Effective Theory for Heavy Quark QCD at Finite Temperature and Density with Stochastic Quantization

Dissertation
zur Erlangung des Doktorgrades
der Naturwissenschaften

vorgelegt beim Fachbereich Physik
der Johann Wolfgang Goethe-Universität
in Frankfurt am Main

von
Mathias Neuman
aus Frankfurt am Main

Frankfurt am Main 2015
D30

vom Fachbereich Physik der

Johann Wolfgang Goethe - Universität als Dissertation angenommen.

Dekan: Prof. Dr. R. Reifarth

Gutachter: Prof. Dr. O. Philipsen
Prof. Dr. D. H. Rischke

Datum der Disputation:

To my Parents

Contents

Contents iii

1 Introduction 1

2 Continuum Quantum Chromodynamics 5
- 2.1 QCD Lagrangian . . . 5
- 2.2 QCD at finite Temperature and Density . . . 7
- 2.3 Symmetries of QCD . . . 9
  - 2.3.1 Center Symmetry . . . 9
  - 2.3.2 Chiral Symmetry . . . 10
  - 2.3.3 Roberge-Weiss Symmetry . . . 11
- 2.4 Asymptotic Freedom . . . 13
- 2.5 QCD Phase Diagram . . . 14
  - 2.5.1 Deconfinement Transition . . . 15
  - 2.5.2 Cold Dense Matter . . . 15

3 QCD on the Lattice 19
- 3.1 Gauge action . . . 20
- 3.2 Fermion action . . . 21
  - 3.2.1 Fermion Doubling . . . 21
  - 3.2.2 Wilson Fermions . . . 22
- 3.3 Numerical Methods . . . 23
  - 3.3.1 Monte-Carlo Method . . . 24
  - 3.3.2 Metropolis Algorithm . . . 25
  - 3.3.3 Stochastic Quantization . . . 26
  - 3.3.4 Data Analysis . . . 27
- 3.4 Finite Density . . . 28
  - 3.4.1 Chemical Potential on the Lattice . . . 28
  - 3.4.2 Sign Problem . . . 29
  - 3.4.3 Silver Blaze . . . 30
- 3.5 Solving the Sign Problem . . . 30
  - 3.5.1 Phase Quenched QCD . . . 31
  - 3.5.2 Reweighting . . . 31
  - 3.5.3 Imaginary Chemical Potential . . . 32
  - 3.5.4 Stochastic Quantization with Complex Action . . . 33

4 An Effective Theory for QCD 35
- 4.1 Effective Action . . . 35

4.2 Strong coupling expansion . . . 36
4.3 Hopping Parameter Expansion . . . 38
4.3.1 Static quark determinant . . . 38
4.3.2 Kinetic Quark Determinant to Leading Order . . . 41
4.3.3 Kinetic Quark Determinant to Next to Leading Order . . . 45
4.4 Gauge Corrections . . . 48
4.4.1 Corrections to Fermion Couplings . . . 48
4.4.2 New Interactions at finite β . . . 51
4.4.3 Fermion Corrections to the Gauge Action . . . 53
4.5 Resummation of the effective action . . . 54
4.6 Multiple Flavors . . . 54
4.7 Cold Dense Limit . . . 55

5 Numerical Results 57
5.1 Integration Measure . . . 58
5.2 Observables . . . 59
5.3 Validity of Stochastic Quantization . . . 59
5.3.1 Comparison between Stochastical Quantization and Monte-Carlo . 60
5.3.2 Criteria for Correctness . . . 60
5.3.3 The logarithm of the static determinant . . . 61
5.4 Numerical Stability . . . 62
5.5 Convergence to full QCD . . . 62
5.5.1 Convergence of the Hopping Expansion . . . 63
5.6 Low Temperature . . . 65
5.6.1 Convergence of the heavy dense limit . . . 65
5.6.2 Setting a scale . . . 65
5.6.3 Continuum extrapolation . . . 67
5.6.4 Liquid-Gas Transition to Nuclear Matter . . . 70
5.7 High Temperature . . . 72
5.7.1 Chiral Condensate . . . 72
5.7.2 Roberge-Weiss Transition . . . 73

6 Analytic Treatment of the Effective Theory 77
6.1 Quarks in the strong coupling limit . . . 77
6.1.1 Static Limit . . . 78
6.1.2 κ^2 corrections . . . 82
6.1.3 κ^4 corrections . . . 85
6.2 Gauge corrections . . . 87
6.3 Analytic Continuum Extrapolation . . . 88
6.4 Resummation of higher order terms . . . 89

7 Conclusions and Outlook 93

A Effective Action to Order κ^4 97

B SU(3) Integration 103

C Transformation of the propagator traces into Polyakov Loops **105**

Bibliography **107**

Deutsche Zusammenfassung

Diese Arbeit beschäftigt sich mit der starken Wechselwirkung, einer der vier heute bekannten fundamentalen Kräften. Als korrekte Theorie zu ihrer Beschreibung gilt heute die Quantumchromodynamik (QCD). Zusammen mit der Theorie der elektroschwachen Wechselwirkung, welche die schwache und elektromagnetische Kraft vereinigt, bildet diese das Standardmodell der Teilchenphysik.

Unser Hauptinteresse gilt der Untersuchung des Phasendiagramms stark wechselwirkender Materie. Für dieses werden gewöhnlich als Parameter die Temperatur T und das chemische Potential μ verwendet. μ ist ein Maß für die Quark-Antiquark Asymmetrie, Regionen mit großen μ sind daher äquivalent zu Regionen hoher Dichte. In dieser Arbeit untersuchen wir zwei Phasenübergänge, den sogenannten *deconfinement* Übergang und den Übergang vom Vakuum zur nuklearen Materie.

Bei hinreichend hohen Temperaturen, wie sie am Large Hadron Collider der Europäische Organisation für Kernforschung oder am Relativistic Heavy Ion Collider des Brookhaven National Laboratory erzeugt werden können, geht das *confinement* verloren und Materie geht in den Zustand des Quark-Gluon-Plasmas über. Die Natur dieses *deconfinement* Übergangs hängt sowohl von den Quarkmassen als auch von μ ab. Bei $\mu = 0$ und physikalischen Quarkmassen handelt es sich um ein *crossover*, also um einen analytischen Übergang.

Von besonderem Interesse für uns, da theoretisch weit weniger gut verstanden, ist die Region tiefer Temperaturen und hoher Dichten. Hier betrachten wir den Übergang vom Vakuum zur Kernmaterie, wie sie im Inneren von Atomkernen oder Neutronensternen vorliegt. Experimente zeigen, dass dieser Übergang bei tiefen Temperaturen erster Ordnung ist und bei $T \approx 20$ MeV in ein *crossover* übergeht.

Der *deconfinement* Übergang findet bei Energien von der Größenordnung der QCD Energieskala, $\Omega \approx 200$ MeV, statt, der Übergang zur Kernmaterie bei $\mathcal{O}(10)$ MeV. Ω ist dabei die Energieskala bei der $\alpha \approx 1$ gilt. Störungstechnische Ansätze, basierend auf Reihenentwicklungen in der Eichkopplung g, sind erst in Bereichen bei Energien viel größer als Ω möglich. Für die Erforschung des QCD Phasendiagramms werden daher nicht-störungstechnische Ansätze benötigt.

In der vorliegenden Arbeit verfolgen wir den 1974 von Wilson eingeführten Ansatz

der Gittereichtheorie. In diesem wird die kontinuierliche Raum-Zeit durch ein Gitter mit endlichem Gitterabstand a ersetzt. Die QCD Wirkung wird dabei in einer passenden Weise diskretisiert, so dass im Grenzfall $a \to 0$, genannt Kontinuumslimes, die ursprüngliche Theorie wiederhergestellt wird. Die so entstehende Theorie wird als Gitter-QCD bezeichnet. Die Diskretisierung gibt den zur Quantisierung der QCD verwendeten Pfadintegralen eine endliche Dimensionalität und erlaubt dadurch deren numerische Lösung. Weiterhin dient die Diskretisierung als Regularisierung, indem Impulse größer als $\frac{\pi}{a}$, abgeschnitten werden.

Die in der Gittereichtheorie vorkommenden Pfadintegrale sind von extrem hoher Dimensionalität, zu ihrer effizienten Lösung kommt daher die sogenannte Monte-Carlo Methode zum Einsatz. In dieser wird das Pfadintegral, welches ein Integral über sämtliche Feldkonfigurationen darstellt, durch eine begrenzte Stichprobe an Konfigurationen approximiert. Die Verteilungsfunktion, nach welcher die Stichproben gewählt werden, wird dabei durch den Boltzmannfaktor, e^{-S} mit Wirkung S, bestimmt. Dieser wird als Wahrscheinlichkeit interpretiert, eine bestimmte Feldkonfiguration vorzufinden, wenn sich das System im Gleichgewicht befindet. Diese als *importance sampling* bekannte Methode gewährleistet eine effiziente Approximierung des Pfadintegrals und ist die Standardmethode zur nicht-perturbativen Lösung der QCD.

Die Gitter-QCD ermöglicht Simulationen bei niedrigen Energien und damit Aussagen über nicht-perturbative Prozesse. Beispiele dafür sind die Berechnung von Hadronmassen, genannt Hadronenspektroskopie, sowie die Untersuchung des *deconfinement* Übergangs. Jedoch führt die Interpretation des Boltzmannfaktors als Wahrscheinlichkeit zu Schwierigkeiten sobald Systeme endlicher Dichte, also Systeme mit endlichem chemischen Potential, betrachten werden. Dies führt notwendigerweise zu einer komplexen Wirkung, wodurch $e^{-S} > 0$ nicht mehr erfüllt ist. Dadurch kann der Boltzmannfaktor nicht mehr als Wahrscheinlichkeit bei der Auswahl der in die Stichprobe einfließenden Feldkonfigurationen dienen, wodurch auf *importance sampling* beruhende Methoden versagen. Dies ist als das Vorzeichenproblem bekannt und hat zur Folge, dass ein Großteil des QCD Phasendiagramms für nichtperturbative Methoden unzugänglich ist.

Zur Bewältigung des Vorzeichenproblems wurden verschiedene Strategien vorgeschlagen. Eine verbreitete Methode ist das so genannte *reweighting*. Bei dieser werden die nicht-positiven Anteile des Boltzmannfaktors in die Observable absorbiert. Diese kann dann mit dem restlichen, strikt positiven Boltzmannfaktor berechnet werden. Die Methode des *reweighting* erlaubt daher, Observablen eines Systems mit Wirkung $S(\mu)$ auf Konfigurationen generiert mit der Wirkung $S(\mu = 0)$ zu berechnen. Brauchbare Ergebnisse werden dabei nur erzielt, wenn die Verteilungen $e^{-S(\mu)}$ und $e^{-S(0)}$ sich nicht signifikant unterscheiden. Dies ist als das *overlap* Problem bekannt. Der statistische Fehler von mit *reweighting* berechneten Werten verschlechtert sich dabei exponentiell

mit $\frac{\mu}{T}$ sowie mit der Größe des Gitters, wodurch die Methode auf kleine Werte von μ/T und kleine Gittervolumina V beschränkt ist.

In dieser Arbeit verfolgen wir einen alternativen Ansatz zur Lösung des Vorzeichenproblems, die stochastischen Quantisierung. Diese wurde 1981 von Parisi und Wu eingeführt und bietet eine alternative, nicht auf Pfadintegralen basierende Methode zur Quantisierung euklidischer Feldtheorien. Die statistische Verteilung der Feldkonfigurationen wird hier als Gleichgewichtsverteilung eines stochastischen Prozesses erzeugt. Dieser Prozess ist durch die Langevin-Gleichung gegeben, einer ursprünglich zur Beschreibung der Brownschen Bewegung aufgestellten stochastischen Differentialgleichung. Die Entwicklung der Freiheitsgrade ϕ strebt dabei zum Minimum der Wirkung, $\frac{\partial\phi}{\partial\theta} = -\frac{\partial S}{\partial\phi}$, und erhält zusätzlich Korrekturen durch einen stochastischen Rauschterm. Diese Entwicklung findet in einer neu eingeführten, fiktiven Zeit θ statt. Ausgehend von einer beliebigen Startkonfiguration ergibt sich dann im Limes $\theta \to \infty$ die gewünschte Gleichgewichtsverteilung.

Da die stochastische Quantisierung nicht auf der Wahrscheinlichkeitsinterpretation des Boltzmannfaktors basiert, funktioniert sie unabhängig davon ob eine komplexe Wirkung vorliegt. Jedoch lässt sich die Äquivalenz zur Pfadintegralmethode nur für reelle Wirkungen beweisen. In der Tat sind Modelle bekannt, bei denen die stochastische Quantisierung bei Existenz einer komplexen Wirkung zu falschen Ergebnissen führt. Wir führen daher auf kleinen Gittern Vergleichssimulationen mit der *reweighting* Methode durch um die Zuverlässigkeit der stochastischen Quantisierung sicherzustellen.

Obwohl die Methode der stochastischen Quantisierung in jüngster Zeit direkt für Gitter-QCD Simulationen verwendet wurde, ist dies extrem rechenintensiv und dadurch auf kleine Gitter beschränkt. Da die Temperatur in Euklidischer Gitter-QCD durch die Ausdehnung in der temporalen Dimension gegeben ist, verhindert die Beschränkung auf kleine Gitter ebenfalls die Untersuchung tiefer Temperaturen. Auch sind in der Gitter-QCD bei hohem chemischen Potential vergleichende, mit *reweighting* durchgeführte Simulationen selbst auf kleinen Gittern unmöglich. Eine unabhängige Überprüfung der Ergebnisse ist dadurch nicht möglich.

Um einen alternativen Zugang zu den Bereichen endlicher Dichte des Phasendiagramms zu ermöglichen leiten wir aus der Gitter-QCD eine effektive Theorie her. Diese soll einerseits einfacher numerisch zu lösen sein, andererseits aber in einem relevanten Parameterbereich zur vollen Theorie konvergieren. Die Herleitung sowie die numerische und analytische Untersuchung dieser Theorie sind das Thema der vorliegenden Arbeit. So sollen Aussagen über bisher unzugängliche Bereiche des Phasendiagramms stark wechselwirkender Materie ermöglicht werden.

Zur Herleitung bedienen wir uns der Störungsrechnung und betrachten zwei Limites. Erstens ist dies der sogenannte *strong coupling* Limes, in welchem die Eichkopplung gegen unendlich geht, $g \to \infty$. In diesem Limes geht die Gittereichkopplung, $\beta \propto \frac{1}{g^2}$,

gegen Null. Es handelt sich hierbei also um den entgegengesetzten Fall des im Kontinuums üblichen Schwachkopplungslimes, welcher zur störungstheoretische Behandlung der QCD bei hohen Temperaturen verwendet wird. Darüber hinaus betrachten wir den Limes unendlich großer Quarkmassen, $m_q \to \infty$, den sogenannte *static quark* Limes. In der von uns verwendeten Wilson Formulierung der Gitterfermionen wird die Quarkmasse durch den Parameter κ bestimmt, der Limes statischer Quarks entspricht$\kappa \to 0$.

Gitter-QCD im *strong coupling static quark* Limes, also mit $\beta = \kappa = 0$, ist exakt lösbar. Ausgehend von diesem Grenzfall berechnen wir Ordnung für Ordnung Korrekturen in β und κ. Diese Entwicklung erlaubt es uns dann, einen Teil der in der Zustandssumme vorkommendenden Integrale explizit auszuführen. Dies ermöglicht es, aus der ursprünglich vierdimensionalen Theorie eine effektive, dreidimensionale Theorie von signifikant reduzierter Komplexität herzuleiten.

Wie bereits erwähnt ist die QCD Kopplung eine Funktion der Energie und damit des Abstands. Deswegen bestimmt in diskreter Raum-Zeit die Gittereichkopplung den Gitterabstand, $a = a(\beta)$. Das Kontinuum wird im Limes $\beta \to \infty$ erreicht. Dies bedeutet, dass der *strong coupling* Limes den Grenzwert maximalen Gitterabstands beschreibt. Sukzessiv eingeführte Korrekturen in β erlauben uns daher die Verwendung feinerer Gitter und dadurch die Annäherung an das Kontinuum. Durch Extrapolation kann dann das Kontinuum, $a = 0$, erreicht werden. Die Korrekturen in κ ermöglicht es uns den Bereich, in dem die effektive Theorie die volle Gitter-QCD abbildet, Schritt für Schritt zu leichteren Quarkmassen auszubauen. Fernziel ist dabei das Erreichen physikalischer Quarkmassen.

Da unsere Theorie lediglich eine Näherung zur vollen Gitter-QCD darstellt, benötigen wir ein Maß für die Größe der Trunkierungseffekte. Wir erlangen dies, indem wir unterschiedliche Trunkierungen in κ und β vornehmen und miteinander vergleichen. Sind die Differenzen zwischen den unterschiedlichen Ordnungen klein kann davon ausgegangen werden, dass Korrekturen höherer Ordnung vernachlässigbar sind und unsere Theorie eine gute Näherung darstellt.

Nachdem wir den Parameterbereich, in dem unsere Theorie eine gute Näherung zur Gitter-QCD darstellt, bestimmt haben, führen wir numerische Untersuchungen durch. Alle Simulationen werden mit einem oder zwei entarteten Quark-Flavors durchgeführt. Dabei betrachten wir die zwei bereits erwähnten Phasenübergänge, den *deconfinement* Übergang zum Quark-Gluonen-Plasma und den Übergang vom Vakuum zur Region endlicher Dichte.

Der *deconfinement* Übergang ist dabei, neben dem bereits angesprochenen Verlusts

des Confinements, durch die spontane Wiederherstellung der chiralen Symmetrie gekennzeichnet. Die von uns verwendeten Wilson Fermionen brechen die chirale Symmetrie explizit. Trotzdem zeigen Gitter-QCD Simulationen mit Wilson Fermionen ein Überbleibsel der Wiederherstellung der chiralen Symmetrie beim erreichen der kritischen Temperatur T_c. Wir untersuchen das chirale Kondensat, den Ordnungsparameter der chiralen Symmetrie, bei verschwindendem chemischen Potential und vergleichen die Ergebnisse mit Gitter-QCD Simulationen.

Der Vergleich mit vollen Gitter-QCD Simulationen ist ebenfalls möglich wenn ein rein imaginäres chemisches Potential, $\mu = i\mu_I$, gewählt wird, da hierbei ebenfalls kein Vorzeichenproblem auftritt. Da die Regionen imaginären und reellen chemischen Potentials analytisch verbunden sind, erlauben solche Simulationen Aussagen über physikalische Parameterbereiche. Das Phasendiagramm im Bereich imaginären chemischen Potentials ist periodisch in μ_I, die einzelnen Sektoren sind durch die so genannten Roberge-Weiss Übergänge getrennt. Diese sind erster Ordnung bei hohen und *crossover* bei tiefen Temperaturen. Die Natur des kritischen Endpunkts ist dabei eine Funktion der Quarkmassen. In Gitter-QCD Simulationen wurden zwei trikritische Punkte gefunden, welche wir versuchen zu replizieren.

Für unsere Untersuchungen im Bereich kalter, dichter Materie stehen keine Gitter-QCD Simulationen zum Vergleich zur Verfügung. Hier betrachten wir, bei Temperaturen zwischen $T = 2.5$ MeV und $T = 20$ MeV, thermodynamischen Größen wie Druck, Teilchen- und Energiendichten. Von besonderem Interesse ist die nukleare Bindungsenergie. Diese ist ein Ergebnis der attraktiven Anziehung zwischen den Quarks, welche zu einer Restwechselwirkung zwischen Nukleonen führt. In der Natur ist diese verantwortlich für die Bildung nuklearer Materie indem sie Protonen und Neutronen bindet.

Durch Simulationen bei verschiedenen Gitterabständen können die Ergebnisse aus dem kalten, dichten Bereich ins Kontinuum extrapoliert werden. Um eine gute Konvergenz zur vollen Gitter-QCD zu gewährleisten, müssen wir uns hierbei auf sehr schwere Quarks, äquivalent zur Verwendung einer Pionmasse von $m_\pi \approx 20$ GeV, beschränken. Ebenso ist die Verwendung feiner Gitter durch die endliche Anzahl an Ordnungen in β beschränkt. Wir verwenden Gitterabstände zwischen $a = 0.11$ fm und $a = 0.08$ fm. Ausgehend von diesen Daten extrapolieren wir dann zum Kontinuum. Mit unseren kontinuumsextrapolierten Ergebnissen können wir demonstrieren, wie beim Verlassen des *static quark* Limes eine endliche Bindungsenergie in der Größenordnung von 10^{-3} Baryonmassen pro Nukleon auftritt.

Ergänzend zu den numerischen Untersuchungen ist es möglich unsere effektive Theorie analytisch zu lösen. Dazu machen wir uns die Existenz kleiner Parameter, nämlich κ und β, zunutze und entwickeln in diesen. Dies erlaubt es uns, die zur Berechnung der Zustandssumme nötigen Integrale explizit zu berechnen. Durch die Kenntnisse der

Zustandssumme können wir analytische Ausdrücke für die verschiedene thermodynamische Größen herzuleiten, welche unsere numerischen Ergebnisse mit hoher Genauigkeit reproduzieren. Weiterhin ermöglicht dies es uns zu zeigen, dass das Nukleon-Nukleon Potential zur führenden Ordnung exponentiell mit der Pionenmasse abfällt, also einem auf Pionenaustausch basierenden Yukawa-Potential entspricht.

Weiterhin eröffnen die analytischen Ausdrücke neue Möglichkeiten der Resummation. Dabei können bestimmte Unterklasse von Diagrammen aufsummiert werden. Dies ermöglicht es den Konvergenzbereich der analytischen Ausdrücke über den Konvergenzbereich der ursprünglichen, effektiven Theorie hinaus zu verbessern. Wir präsentieren Ansätze wie eine solche Resummation in κ durchgeführt werden kann. Zusätzlich zeigen wir, wie β Korrekturen hierzu hinzugefügt werden können. Mithilfe dieses Ansatzes könnte es möglich sein in zukünftigen Arbeiten den Konvergenzbereich der effektiven Theorie in der kalten, dichten Region bis zu physikalischen Quarkmassen auszubauen.

Chapter 1

Introduction

Today, three of the known four fundamental forces are described by the Standard Model, with only gravitation yet to be included. It includes electromagnetism, strong and weak interaction, which are formulated as quantum field theories and can be characterized by their symmetry with respect to certain gauge groups. Electromagnetism and weak interaction are unified in the electroweak force, a gauge theory with symmetry group $SU(2) \times U(1)$ [1].

This thesis is concerned with the theory of strong interaction, called Quantum Chromodynamics (QCD). It is widely believed nowadays to be the correct theory of strong interaction, an overview covering recent high energy experiments testing QCD predictions can be found e.g. in [1]. No mismatch between QCD and experiment has been found so far.

The beginnings of QCD lies in the early 1960s, when Gell-Mann [2] and Ne'eman [3] independently discovered that the large number of newly discovered baryons and mesons, originally thought to be fundamental, could be arranged in patterns formed by different SU(3) representations. The success of this so called Eightfold Way, especially in the prediction of the Ω^-, hinted at a common substructure of the hadrons. After that, the quark model was introduced independently by Gell-Mann [4] and Zweig [5] in 1964, proposing that hadrons are bound states of fundamental particles called quarks. Initially, three different types of quarks, called flavors, where postulated. Those where the up, down and strange quark. The quark model explained the success of the Eightfold Way in terms of the approximately realized flavor symmetries between this three quarks, whose mass difference is small compared to the masses of the hadrons they form. Today six quark flavors are known, whose properties are given in table 1.1. [2] [3]

[1] $U(N)$ denotes the group of unitary $N \times N$ matrices, $SU(N)$ is the respective subgroup that only contains matrices with determinant 1.

[2] Because of confinement, quark masses depend on the subtraction scheme and the energy scale used, see [6].

[3] Throughout this thesis natural units will be used, i.e. $c = \hbar = 1$.

Flavor	up	down	strange	charm	bottom	top
Mass[MeV]	≈ 2.3	≈ 4.8	≈ 95	$\approx 1.3 \cdot 10^3$	$\approx 4.2 \cdot 10^3$	$\approx 160 \cdot 10^3$
Charge[e]	2/3	-1/3	-1/3	2/3	-1/3	2/3

TABLE 1.1: Masses and charges of the six quark flavors.

The quark model made the introduction of a new quantum number, called color, necessary. This became apparent with particles like the Δ^{++}, which consists of three up quarks with parallel spins and vanishing orbital momentum, giving it a symmetric wave function. In order to receive a antisymmetric wave function, as required by the Pauli exclusion principle, Greenberg in 1964 postulated the existence of a new, hidden quantum number [7]. The number of colors, N_c, can be concluded from the ratio of the cross section $e^+e^- \to$ hadrons and $e^+e^- \to \mu^+\mu^-$, which QCD perturbation theory predicts to be proportional to N_c. Experiments show that $N_c = 3$ [8].

While being successful in explaining the known hadron spectrum, needing only a small number of degrees of freedom, the quark model fails to give an explanation to two crucial phenomena. Firstly, no color carrying states or fractional charges could be observed in experiment, instead quarks always form color singlets (color neutral states), built from three (anti-)quarks or a quark-anti-quark pair [4]. This phenomenon is known as color confinement. Secondly, and contrary to the observation of confinement, deep inelastic scattering experiments showed quarks to behave as free particles at high momentum transfer or, equivalently, small distance. This indicates that the strength of the strong interaction, measured as $\alpha_s = \frac{g^2}{4\pi}$, with g being the gauge coupling, decreases at high energies. This phenomenon is known as asymptotic freedom.

The apparent contradiction can be resolved by formulating the strong interaction as a Yang-Mills gauge theory [10], a gauge theory shown to exhibit asymptotic freedom by Gross [11], Wilczek and Politzer [12] and shown to be renormalizable by t'Hooft [13]. The resulting theory of strong interaction is known as QCD.

We will give a short introduction of QCD in its continuum formulation in chapter 2, defining its Lagrangian and demonstrating how the theory can be quantized in an Euclidean spacetime by the use of Feynman path integrals. We will also introduce some important symmetries that will be needed later in the thesis. Furthermore, we discuss the QCD phase diagram, i.e. the phase diagram of strongly interacting matter. Due to the running of the coupling, perturbative approaches, which rely on expansions in the gauge coupling g, are limited to the region of asymptotic high energies and densities. Because of this, a large region of the QCD phase diagram is only accessible to nonperturbative approaches.

One such approach, called lattice QCD (LQCD), is presented in chapter 3. LQCD is the formulation of QCD in a discrete space-time. This is achieved by replacing space-time

[4] States consisting of more than three quarks are hypothesized but are not confirmed yet [9].

by a lattice with lattice spacing a, introducing a shortest distance. This approach gives path integrals a finite dimensionality and allows their evaluation by means of numerical methods. We will introduce, Some of those methods, namely Monte-Carlo and stochastic quantization. The use of Monte-Carlo methods has proven to be highly successful in describing zero density QCD. Examples are the calculation of hadron masses [14] and simulations of the crossover to the quark-gluon plasma [15]. However, they fail when simulating systems with a finite net density of fermions, i.e. systems with a nonvanishing chemical potential μ. We will discuss this issue, known as the sign problem. We will furthermore discuss the different approaches that have been developed in recent years in order to circumvent the sign problem and demonstrate their respective achievements and shortcomings.

The main goal of this thesis is to offer a new possibility for investigating finite density QCD by deriving an effective theory of LQCD. The purpose of such an effective theory is to be less computationally demanding and have a less pronounced sign problem compared to LQCD, while converging to LQCD in a controlled parameter region. We describe the derivation of this effective theory in chapter 4. The theory is derived by an expansion around the limit of infinite quark masses m_q and infinite gauge coupling g and can be systematically improved order by order. We will furthermore demonstrate how the theory simplifies significantly when we consider the limit of cold temperatures and high densities. This parameter region is of particular interest, since it includes the region of nuclear matter and is inaccessible to LQCD simulations.

In chapter 5 we will then show how our theory is solved numerically. We compare different algorithms and present results for two distinct regions of the QCD phase diagram. One is, for reasons just mentioned, the region of low temperature and high density. Here we will present continuum extrapolated results for different thermodynamical quantities and demonstrate the existence of a finite nuclear binding energy. The other region of interest is the region of zero density, since here LQCD results exist for comparison. We will investigate the chiral condensate, which is an approximate order parameter for the chiral symmetry. Furthermore we will repeat LQCD investigations at imaginary chemical potential, where we investigate the nature of the critical Roberge-Weiss endpoint.

The numerical results are complemented with the analytic approach presented in chapter 6. In the cold dense limit this allows us to derive analytic expressions for all thermodynamical observables, accurately reproducing the numerical results from chapter 5. This approach also opens new resummation possibilities, which we will discuss.

Chapter 2

Continuum Quantum Chromodynamics

In this chapter we introduce the theory of Quantum Chromodynamics (QCD) in the continuum, aiming to give a rough overview and highlighting some key features that will be needed in the later parts of the thesis. For a far more detailed overview consult the textbooks [16, 17], on which we partly rely in the following presentation. We start with reviewing the QCD Lagrangian in section 2.1. Section 2.2 is concerned with the quantization of QCD, the transition to Euclidean space-time and the introduction of finite temperature and density. In section 2.3 we present some important symmetries of QCD, while section 2.4 is concerned with the running coupling. Finally, in section 2.3, we discuss the phase diagram of strongly interacting matter.

2.1 QCD Lagrangian

QCD is a Yang-Mills theory, a non-abelian gauge theory with gauge group $SU(N_c = 3)$, coupled to fermion fields in the fundamental representations. The gauge field quanta are called gluons, the quanta of the fermion fields are the quarks. The theory is defined by its Lagrange density, which is constructed by requiring invariance under local $SU(3)$ rotations and renormalizability. The Lagrange density can conveniently be split into a fermionic and a pure Yang-Mills part. The latter part, describing the dynamics of the gluon field in the absence of quarks, being [1]

$$\mathcal{L}_g = -\frac{1}{4} F^a_{\mu\nu}(x) F^{\mu\nu a}(x). \tag{2.1}$$

The field strength tensor $F^a_{\mu\nu}$ depends on the gauge fields A^a_μ,

$$F^a_{\mu\nu} = \partial_\mu A^a_\nu - \partial_\nu A^a_\mu + g f_{abc} A^b_\mu A^c_\nu, \quad [T^a, T^b] = i f_{abc} T^c, \tag{2.2}$$

[1] Throughout this thesis summation over repeated indices is implied.

with Lorenz indices $\mu, \nu = 0, 1, 2, 3$ and adjoint color indices $a, b, c = 1, ..., N_c^2 - 1$. The generators of the $SU(3)$ group are the eight Gell-Mann matrices λ^a, $T^a = \frac{\lambda^a}{2}$, with f_{abc} being the structure constants of $SU(3)$. In analogy to the electromagnetic coupling constant $\alpha_{em} = \frac{e^2}{4\pi}$, depending on the elementary electromagnetic charge e, the strength of the QCD interaction is given as the strong coupling constant $\alpha_s = \frac{g^2}{4\pi}$, depending on the gauge coupling g. The field strength tensor includes terms that are cubic and quartic in the gauge fields, giving rise to gluon self interaction, a consequence of the non abelian nature of QCD. This is in contrast to abelian theories like Quantum Electrodynamics, where gauge fields carry no charge and therefore do not interact with each other. This self interaction gives already the pure gauge part of QCD a highly non trivial dynamics.

The fermionic part of the Lagrange density for N_f quark flavors is

$$\mathcal{L}_F(\psi, \bar{\psi}, A) = \bar{\psi}(i\not{D} - m)\psi. \tag{2.3}$$

The quark field spinors, $\psi = \psi_{i,\alpha,c}$, carry a fundamental color index $c = 1, .., N_c$, a flavor index $i = 1, ..., N_f$ and a Lorentz index $\mu = 0, 1, 2, 3$. The Dirac matrices, acting in flavor space, are defined by their anticommutation relations,

$$\{\gamma^\mu, \gamma^\nu\} = \gamma^\mu\gamma^\nu + \gamma^\nu\gamma^\mu = 2g^{\mu,\nu} \times \mathbb{1}, \tag{2.4}$$

where we have chosen the Minkowski metric $g^{\mu,\nu}$ to have the signature $(+, -, -, -)$. The quark masses enter via the mass matrix, which is diagonal in flavor space, $m = \text{diag}(m_u, m_d, ...)$. The covariant derivative $\not{D} = \gamma^\mu D_\mu$ is formulated in a way that preserves gauge invariance, which is achieved by adding gauge fields,

$$\not{D} = \gamma^\mu(\partial_\mu - igA_\mu), \tag{2.5}$$

with $A_\mu = A_\mu^a T^a$. The resulting Lagrange density, $\mathcal{L} = \mathcal{L}_g + \mathcal{L}_f$, is by construction invariant under $SU(3)$ gauge transformations, $\mathcal{L}[\psi, \bar{\psi}, \mathcal{A}] = \mathcal{L}[\psi', \bar{\psi}', \mathcal{A}']$. Under such a transformation fermion fields transform in the fundamental and gauge fields transform in the adjoint representation,

$$\begin{aligned}
\psi(x) \to \psi'(x) &= U(x)\psi(x), \\
\bar{\psi}(x) \to \bar{\psi}'(x) &= \bar{\psi}(x)U^\dagger(x), \\
A_\mu(x) \to A'_\mu(x) &= U(x)\Big(A_\mu(x) + \frac{i}{g}\partial_\mu\Big)U^\dagger(x),
\end{aligned} \tag{2.6}$$

with $U \in SU(3)$. Indeed this is the most general Lagrange density that is invariant under gauge transformation while still being renormalizable [2]. It encodes all the features of

[2] The addition of an additional, CP symmetry breaking terms is possible, but will not be considered here.

strongly interacting matter, while involving only seven free parameters, namely the six quark masses m_f and the gauge coupling g, which have to be fixed through input from experiment.

2.2 QCD at finite Temperature and Density

The Lagrange density presented in the last section defines QCD on a classical level. In order to quantize the theory we make use of the Feynman Path Integral formalism, which allows us to express the transition amplitude between field configuration as an integral,

$$\langle\phi_1|e^{-i\hat{H}(t_2-t_1)}|\phi_2\rangle \sim \int D[\bar{\psi},\psi,A]\exp\Big(i\int_{t_1}^{t_2}dx_0\int d^3x\mathcal{L}\Big), \tag{2.7}$$

with Hamiltonian $\hat{H}$. The integration measure, $D[\psi,\bar{\psi},A]$, is meant to represent an integral over all possible field configurations with ϕ_1 and ϕ_2 as boundary conditions. This is ill defined in the continuum since we have an infinite number of degrees of freedom, but will become clearer once we switch to a discrete space-time formulation. The quantity in the exponent is called the action, it is given by the space-time integral over the Lagrange density,

$$S = \int d^4x\mathcal{L}. \tag{2.8}$$

The Path Integral formalism expresses the transition amplitudes in terms of ordinary fields instead of operators. Gauge fields are represented in terms of complex numbers, while the fermion fields are represented by anticommuting Grassmann variables,

$$\eta_i\eta_j = -\eta_j\eta_i. \tag{2.9}$$

We will later see how they can be integrated out to make the partition function depend solely on ordinary numbers.

Since the exponent in 2.11 is purely imaginary for a real action, the weight e^{iS} will be complex, with its real part being highly oscillating. For numerical treatment this is not desirable, because the result will strongly depend on cancellations between contributions from different field configurations. It is therefore common to switch from real to imaginary time, using the so called Wick rotation,

$$t \to -i\tau, \quad S \to iS_E, \quad L \to -L_E. \tag{2.10}$$

The imaginary time formalism allows us to make a connection between Euclidean field

theory and statistical equilibrium physics. The central quantity for deriving expectation values for a system in equilibrium is the grand canonical partition function, which describes a system of volume V in thermal and chemical equilibrium with a reservoir of temperature T and chemical potentials μ_i. Each chemical potential is coupled to the respective conserved particle number $N_i = \int d^4x\ \bar{\psi}_i \gamma_0 \psi$,

$$Z[T, \mu, V] = \text{Tr}\ e^{-(\hat{H} - \mu_i \hat{N}_i)/T}. \tag{2.11}$$

The formal similarity between this and eq. 2.7 allows us to express the partition function as a path integral,

$$Z = \int D[\psi, \bar{\psi}, A] \exp(-S_E[\psi, \bar{\psi}, A]). \tag{2.12}$$

Here the path integral now represents an integral over all possible field configurations,

$$\int D[\bar{\psi}, \psi, A] = \int \prod_x d\psi_x d\bar{\psi}_x dA_x. \tag{2.13}$$

The chemical potential can be included into the action as the fourth component of an imaginary vector potential, coupled to the quark fields,

$$S_E = \int_0^{1/T} d\tau \int d^3x\ \bar{\psi}_i (\not{D}_{\mu,E} + m_i + \gamma_4 \mu_i)\psi_i + \frac{1}{4} F^a_{\mu\nu} F^a_{\mu\nu}, \tag{2.14}$$

with

$$\not{D}_{\mu,E} = \gamma_\mu (\partial_\mu + igA_\mu) \tag{2.15}$$

The change to an Euclidean action cures the problem of having an imaginary exponent like in eq. 2.7 as long as S_E is real. We will later see how it reemerges when treating systems that have finite chemical potential, i.e. finite density systems.

The rotated, imaginary time dimension $i\tau$ is now interpreted as a temperature by compactifying it to $[0, 1/T)$. The compactification of the temporal dimension makes the introduction of appropriate boundary condition necessary. We chose periodic boundary conditions for bosons and antiperiodic ones for fermions, reflecting their respective statistical properties:

$$\begin{aligned} A(\vec{x}, 0) &= A(\vec{x}, 1/T), \\ \psi(\vec{x}, 0) &= -\psi(\vec{x}, 1/T). \end{aligned} \tag{2.16}$$

Expectation values can be computed as the average over all field configuration, weighted with the Euclidean action:

$$\langle \mathcal{O} \rangle = \frac{1}{Z} \int \mathcal{D}[\psi, \bar{\psi}, A] \mathcal{O} \exp(-S_E). \tag{2.17}$$

The fact that the weight in the Euclidean path integral suppresses a large fraction of the phase space will later allow for efficient numerical treatments by Monte-Carlo methods. Since we will exclusively use the Euclidean formulation of QCD we will drop the index E for the Euclidean action from now on.

2.3 Symmetries of QCD

The QCD Lagrangian exhibits several local and global symmetries, some of which are spontaneously broken or only approximately realized. Here we will shortly discuss the symmetries that will be of importance for the later parts of this thesis.

2.3.1 Center Symmetry

Pure gauge theory, described by the Lagrangian eq. 2.1, exhibits a symmetry called Center, or $Z_{N_c=3}$, Symmetry. Letting the gauge transformations U in the transformation eq. 2.6 pick up an additional twist z when crossing the temporal boundary,

$$U(\vec{x}, \tau) = zU(\vec{x}, \tau + 1/T), \tag{2.18}$$

leaves the Lagrangian invariant if z is an element of the $SU(3)$ center. The center of the $SU(3)$ group is the subgroup that commutes with all members of the group, $z \in Z_3 = \{1, e^{2/3i\pi}, e^{-2/3i\pi}\}$. The simplest gauge invariant quantity that is affected by this is the so called Polyakov loop,

$$L(\vec{x}) = \mathrm{Tr}\ \mathcal{P} e^{ig \int_0^{1/T} A_4(\vec{x}, \tau)}, \tag{2.19}$$

with time-ordering operator $\mathcal{P}$. Under Z_3 transformation such a Polyakov loop will pick up a factor z, $L \to L^{'} = zL$. If the Z_3 symmetry is realized, i.e. if the action is invariant under such a transformation, the Polyakov loop expectation value will average out over the three possible phases,

$$\langle L \rangle = \frac{1}{3} \langle L + zL + z^2 L \rangle = 0. \tag{2.20}$$

A broken Z_3 symmetry, meaning that one sector is favored, gives L a finite expectation value. L is therefore an order parameter for the Z_3 symmetry. In the gauge sector of QCD center symmetry is realized at low temperatures, while being spontaneously

broken at a critical temperature T_c. This acquires a physical meaning when we use the Polyakov loops to represent a single, static color charge. The expectation value for such a charge is given by

$$\langle L(\vec{x})\rangle = \frac{1}{Z}\int [dU] L(\vec{x}) e^{-S_g} = \frac{Z_L}{Z} = e^{-\Delta F/T}, \tag{2.21}$$

where Z and Z_L denote the partition functions for a system with and without the charge respectively. The ratio of both partition functions vanishes exponentially with the free energy difference between both systems, ΔF. A vanishing Polyakov loop expectation value therefore signals that $\Delta F \to \infty$, meaning it takes an infinite amount of energy to place a single color charge in the system. A finite Polyakov loop expectation value correspondingly signals that such a configuration can be created with a finite amount of energy. The center symmetry is therefore connected to confinement, with the breaking of the symmetry at T_c indicating deconfinement.

Center symmetry gets explicitly broken by the introduction of dynamical quarks, leading to a nonzero, although exponentially suppressed, Polyakov loop at low temperatures. Physically, this is caused by the screening of color charges through pair production, making ΔF finite even in the confined phase. Since the deconfinement transition is a crossover for physical quark masses and zero chemical potential, no real order parameter exists. Nevertheless, the Polyakov loop is used as an indicator for deconfinement.

2.3.2 Chiral Symmetry

In the limit of N_f massless quarks the QCD Lagrangian exhibits the so called chiral symmetry. Decomposing the quark fields into left and right handed spinors,

$$\psi_L = \frac{\mathbb{1} - \gamma_5}{2}\psi, \quad \psi_R = \frac{\mathbb{1} + \gamma_5}{2}\psi, \tag{2.22}$$

the fermion part of the Lagrangian decouples,

$$\mathcal{L} = \bar{\psi}_L \not{D} \psi_L + \bar{\psi}_R \not{D} \psi_R. \tag{2.23}$$

This means that, in absence of the mass matrix in eq. 2.14, the left and right handed components of the quark spinors do not mix. The Lagrangian is then invariant under separate rotations of the spinors in flavor space,

$$\psi_{L/R} \to \psi'_{L/R} = U\psi_{L/R}, \quad U \in U(N_f). \tag{2.24}$$

This symmetry can be decomposed into

$$U(N_f)_L \times U(N_f)_R = SU(N_f)_L \times SU(N_f)_R \times U(1)_V \times U(1)_A. \tag{2.25}$$

The $U(1)_V$ symmetry remains unbroken, its related conserved Noether charge being the baryon number. The axial $U(1)_A$ symmetry, although present on the level of the Lagrangian, gets broken explicitly by quantum corrections due to the presence of instantons [18].

The remaining $SU(N_f)_L \times SU(N_f)_R$ symmetry is called chiral symmetry. If chiral symmetry was realized exactly in nature, the equality between right and left handed components would mean that states of opposite parity, like the N and the N^*, are mass degenerate. This is not realized in nature, where we find the masses to be $m_N = 939.6\text{MeV}$ and $m_{N^*} = 1535\text{MeV}$. As can be seen looking at the masses of the up and down quark in table 1.1, this difference is too big to be explained be the explicit symmetry breaking introduced by finite quark masses. This suggests that the chiral symmetry is broken spontaneously,

$$SU(N_f)_L \times SU(N_f)_R \to SU(N_f)_V. \tag{2.26}$$

The order parameter for the chiral symmetry is the chiral condensate,

$$\langle \bar{\psi}\psi \rangle = \langle \bar{\psi}_L \psi_R + \bar{\psi}_R \psi_L \rangle = -\frac{T}{V}\frac{\partial Z}{\partial m_q}, \tag{2.27}$$

with m_q being the mass of the light quarks. A finite chiral condensate signals the formation of a quark-anti-quark condensate in the vacuum and the breaking of the chiral symmetry. According to the Goldstone theorem, the spontaneous breaking of a continuous symmetry is accompanied by the appearance of massless, scalar bosons, called Goldstone bosons. The Goldstone bosons connected to the breaking of chiral symmetry are the pions. Their small, although nonzero, masses are a result of the explicit chiral symmetry breaking due to the nonzero up and down quark masses. Chiral symmetry gets restored above a critical temperature T_c, called the chiral phase transition [3]. At small values of the chemical potential it coincides with the deconfinement transition. Both transitions are crossover for physical quark masses.

2.3.3 Roberge-Weiss Symmetry

The QCD phase diagram can be extended into the region of imaginary chemical potential, $\mu_i = i\mu$. Here, QCD exhibits a new symmetry that is related to the center symmetry described in section 2.3.1. The center symmetry gets broken explicitly by

[3] Throughout this thesis we use the term "transition" in a loose way, describing any rapid change in thermodynamical observables including crossovers.

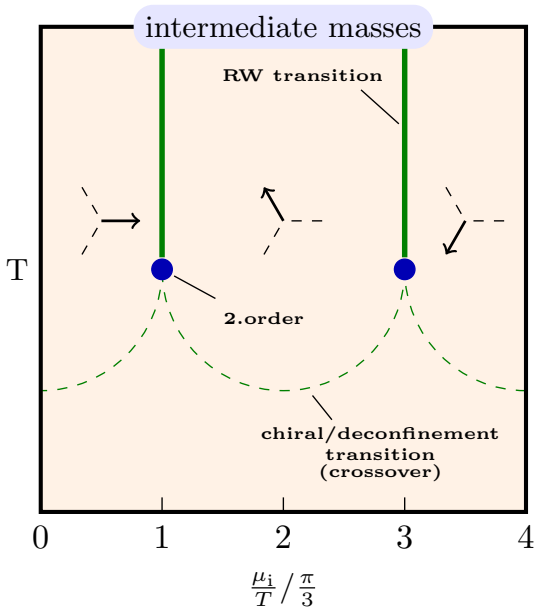

FIGURE 2.1: QCD phase diagram in the region of imaginary chemical potential for different quark masses. The nature of the deconfinement transition indicated by the dashed line depends in the quark mass. Taken from [19]

the introduction of dynamical fermions. However, the effect of a Z_3 transformation on the fermion fields can be absorbed into a shift in the imaginary chemical potential, $\mu_i/T \to \mu_i/T + 2/3n\pi$. This makes the partition function periodic in $\frac{\mu_i}{T}$,

$$Z(\mu_i/T) = Z(\mu_i/T + 2/3\pi n), \quad n \in \mathbb{N}. \tag{2.28}$$

This is called the Roberge-Weiss Symmetry [20]. The resulting phase diagram is shown schematically in fig. 2.1. There are different Z_3 sectors that are separated by Roberge-Weiss transitions at

$$\mu_i/T = 2/3\pi(n + 1/2), \quad n = 0, \pm1, \pm2, ... \tag{2.29}$$

The different sectors can be distinguished by the Polyakov loop phase, $L = |L|e^{i\phi}$, which changes as we move through the Z_3 sectors. The transition between the sectors is of first order at high temperature, ending in an endpoint as temperature is lowered. As can be seen in fig. 2.1 the nature of this endpoint depends on the nature of the dashed lines. The transition order of those depends on the quark masses. For $N_f = 2$ degenerate quarks they are of first order at very high and very low quark masses, meaning that at the endpoints we have coexistence of three phase. At intermediate masses, the dashed lines are crossovers and the Roberge-Weiss transition has a second order endpoint. Therefore two tricritical points exist, separating those two cases [19].

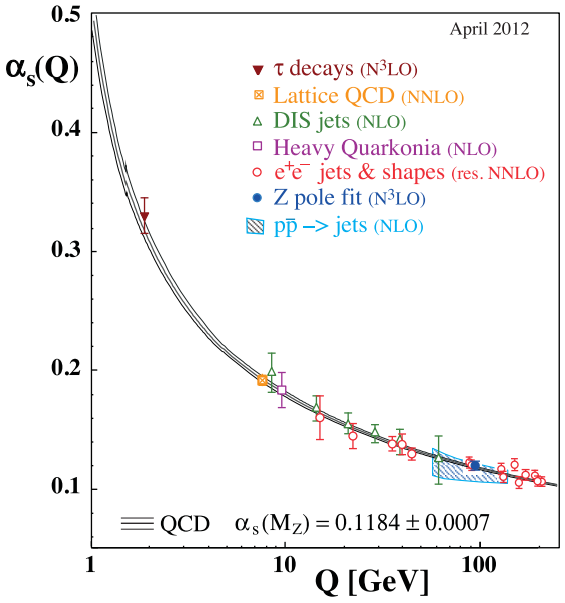

FIGURE 2.2: Strength of the gauge coupling $\alpha_s \sim \frac{1}{\log(Q)}$ as a function of the energy scale Q. At low energies the coupling becomes strong, spoiling perturbative approaches. Taken from [6].

2.4 Asymptotic Freedom

Coupling constants and masses appearing in the action are only bare parameters and get modified when renormalization is employed. In this process the theory is regularized by introducing a ultraviolet cutoff Δ in order to cancel divergences appearing when calculating observables. Coupling constants then get modified, while keeping observables constant. This allows to take the cutoff to infinity. The running of the gauge coupling g with energy scale M is determined by the so called β function,

$$\frac{\partial a_s}{\partial \ln(M)} = \beta(g). \tag{2.30}$$

A negative sign of the β function will therefore mean that the coupling goes to zero at high energies, leading to asymptotic freedom. In QCD the leading order of β, calculated with perturbation theory for N_f massless quarks to one loop order, is [11, 12]

$$\beta = -(\frac{11}{3}N_c - \frac{2}{3}N_f)\frac{g^3}{(4\pi)^2} + \mathcal{O}(g^5). \tag{2.31}$$

β is therefore negative. Solving eq. 2.30 gives

$$\alpha_s(M) = \frac{1}{\frac{1}{12\pi}(11N_c - 2N_f)\ln(\frac{M}{\Delta_{QCD}})}, \tag{2.32}$$

with $\Delta_{QCD} \approx 200$MeV being the QCD energy scale. The dependence on a dimensionless coupling has therefore been replaced with a dimensionful quantity, a process known as

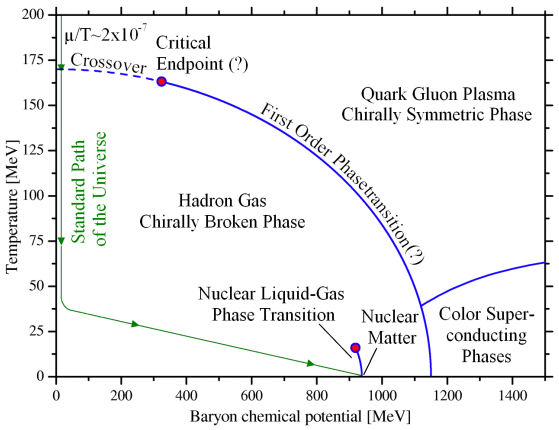

FIGURE 2.3: Sketch of the QCD phase diagram. Of the shown transitions only the deconfinement crossover and the nuclear liquid gas transition are well studied experimentally. Taken from [21].

dimensional transmutation. Fig. 2.2 shows how the prediction of QCD, derived through perturbation theory and using the experimental value of α_s at the energy scale of the Z-Boson mass as an input, compared to different experiments. The fact that the gauge coupling goes to zero logarithmically as $M \to \infty$ allows for perturbative treatment of QCD in the high temperature region where $M >> \Delta_{QCD}$. The running of the coupling is well established experimentally [6] and allows to make theoretical predictions for high energy processes in particle accelerators, serving as the main source for comparisons between theory and experiment. At low energies the coupling grows, making the use of nonperturbative methods necessary.

2.5 QCD Phase Diagram

Our theoretical understanding of the phase diagram of QCD matter is limited, with perturbation theory being only valid at temperatures or values of the chemical potential much larger than Δ_{QCD}, and the breakdown of nonperturbative lattice methods at finite chemical potential [22]. Fig. 2.3 shows one possible phase diagram, including some conjectured phase boundaries together with the path the universe evolved along after the Big Bang. It has to be stressed that of the phase boundaries shown only the crossover to the quark gluon plasma and the liquid gas transition to cold nuclear matter are studied experimentally. Other phases and phase boundary are conjectures based on different theoretical approaches. Many more phases than shown in fig. 2.3 are speculated to exist at large μ. Here we want to discuss the regions of the phase diagram that are relevant for this thesis, namely the high temperature, low density region where deconfinement transition to the quark gluon plasma takes place and the low temperature, high density phase of nuclear matter.

2.5.1 Deconfinement Transition

As we have seen in the last section the gauge coupling will decrease as temperature or density rises. This led to the prediction of a new state of matter at high temperatures, where confinement gets lost and chiral symmetry is restored, the Quark Gluon Plasma (QGP) [23]. The QGP was finally produced in experiment at RHIC [24] and CERN [25].

The transition from the hadronic phase, where quarks are confined to hadronic states, and the quark gluon plasma, where they are free, is not a real phase transition at vanishing chemical potential. It rather is a broad crossover, characterized by rapid changes in pressure and energy density due to the increase in the number of degrees of freedom [26]. The position and width of the transition will therefore depend on the observables used, and no exact critical temperature can be stated. Common choices in lattice calculations are the maximum in the Polyakov loop susceptibility to determine deconfinement and the maximum in the chiral condensate susceptibility to determine the restoration of chiral symmetry. Both methods yield critical temperatures of $T_c \approx 150$ MeV, with transition widths of $\mathcal{O}(10)$ MeV [15, 26]. It is speculated that the crossover turns into a first order transition as chemical potential is raised, but the location of the critical endpoint of this first order transition and even its existence is unclear so far. Lattice Methods for studying the critical endpoint are e.g. Taylor Expansion [27], Monte Carlo with reweighting [28] and simulations at imaginary chemical potential [29]. We will discuss those techniques in chapter 3, when talking about simulations at finite density. Although hints for the existence of a critical endpoint have been found experimentally [30], no conclusive result has been reached so far [31].

2.5.2 Cold Dense Matter

The low temperature, high density region, including nuclear matter, is inaccessible to non-perturbative lattice methods. The reason for this lies in the sign problem, which will be discussed in section 3.1. Studying this region therefore relies mainly on effective models, large N_c expansion and chiral perturbation theory. For a review covering the theoretical and experimental approaches for studying the high density region see e.g. [33].

If we move along the lower axis in fig. 2.3 we are in the zero temperature limit. This is a good approximation to the state we find in atomic nuclei and in compact stars. Such a system will be in its ground state and the baryon density will be zero as long as $\mu_B < \mu_c = m_B - \epsilon$, with m_B being the lightest baryon state and $\mu_B = 3\mu$ the baryon chemical potential. ϵ is the nuclear binding energy, whose magnitude depends on the baryon density, reaching a maximum of $\epsilon_{\text{sat}} \approx 16.3$ MeV per nucleon at a saturation density of $n_{\text{sat}} \approx 0.17$ nucleons per fm^3 [16]. Those values will get modified when

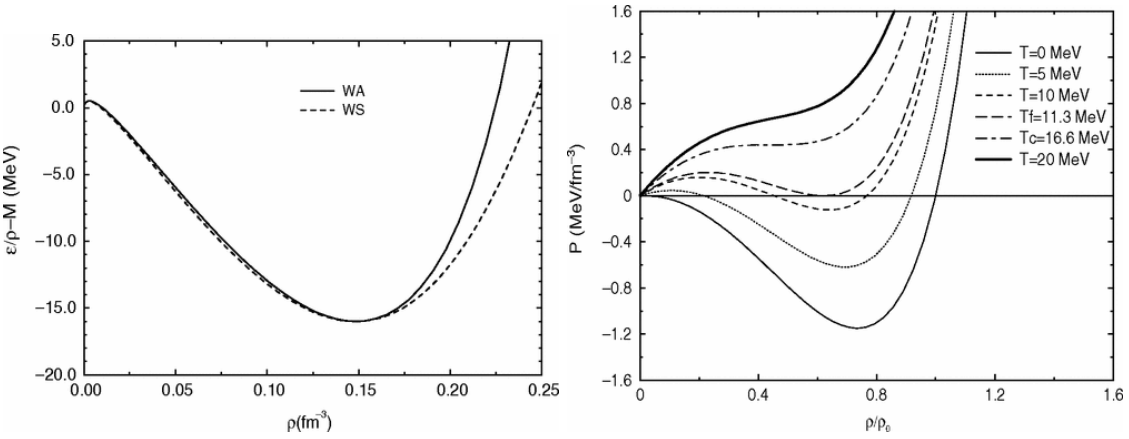

FIGURE 2.4: Left: Binding energy of nuclear matter derived using mean field approximations, plotted against the baryon number density. Right: Pressure for different temperatures plotted against the baryon density, predicting $T_c = 16.6$MeV. Taken from [32].

electromagnetic forces are included. Furthermore, they depend on the composition of the nuclear matter. The left side of fig. 2.4 shows the binding energy, derived from mean field approximations, plotted against the baryon density.

The existence of a finite binding energy means that at intermediate values of the chemical potential a state of uniform density is energetically disfavoured. Instead, we will find a state where matter forms into droplets of nuclear matter with density n_{sat}, surrounded by vacuum. The coexistence of two different phases means that the transition from the vacuum to nuclear matter is of first order. At finite temperature the nuclear matter drops will be surrounded by an evaporated hadron gas. As temperature gets raised this gas will become denser, while the density of the droplets gets lower. Finally, above a critical temperature, both phases will have the same density and the distinction between both phases vanishes. This critical temperature marks the critical endpoint of the first order liquid-gas transition between both phases and is experimentally found to be $T_c \approx 20$ MeV [34]. The left side of fig. 2.4 shows the prediction of T_c from a mean field approximation.

If we stay at low temperatures and go to increasingly higher values of μ, more and more space will become occupied until we eventually end up with a uniform state of nuclear matter. At lower densities physical nuclear matter, i.e. matter also underlying QED interactions, is expected to form various structures called "pasta". Their shape is determined through the competition between repulsive Coulomb interaction and the surface energy [35].

At even higher values of the chemical potential asymptotic freedom is expected to lead to deconfinement and a state of matter called quark matter, but no experiments involving such matter exist. Predictions regarding this phase therefore rely on the use of effective models [36]. Only at asymptotically high densities the Fermi momentum

$k_f \sim \sqrt[3]{n}$ becomes large and rigorous calculations based on perturbation theory becomes possible again. It is predicted that quarks on the Fermi surface will form Cooper Pairs and therefore become superconductive, breaking the local $SU(3)$ color symmetry. Such extreme states of matter are speculated to exists inside of compact stars [37].

Chapter 3

QCD on the Lattice

In this chapter we will introduce lattice QCD (LQCD) and discuss some of its features. We will furthermore discuss how the theory is solved numerically.

LQCD is the formulation of QCD in discrete space-time and constitutes the main tool for nonperturbative investigations of QCD. It was pioneered in 1974 by Wilson, who used it to demonstrate confinement in the limit of infinite gauge coupling [38]. An overview over the development of the field of lattice gauge theory can be found e.g. in [39, 40].

The underlying idea of LQCD is to replace continuous space-time with a hypercubic lattice Λ with lattice spacing a[1], such that $x = (x_1, x_2, x_3, x_4) \in \Lambda$. We call the spatial extent N_σ and the temporal extent N_τ, so that the lattice consists of $N_\sigma^3 N_\tau$ lattice points occupying a volume of $a^4 N_\sigma^3 N_\tau$. Since introducing a shortest distance a is equivalent to a momentum cutoff π/a, this also serves as a regularization. Furthermore, it means that integrals of the type eq. 2.13 will be of finite dimensionality, making them well defined. This will allow the calculation of expectation values by solving eq. 2.17 via numerical integration.

In this chapter we will proceed in the following way: In section 3.1 and 3.2 we discuss how a discretized version S_{latt} of the continuum action can be derived in a way such that $S_{\text{latt}} \to S_{\text{cont}}$ as we take the continuum limit. This limit is defined by taking $a \to 0$, while keeping physical quantities like $\frac{1}{aN_\tau}$, i.e. the temperature, constant. Furthermore, in section 3.3, we will present different methods for numerical evaluation of high dimensional integrals, needed for the effective treatment of LQCD. Finally, in section 3.4, we will discuss the simulation of finite density systems. We will show how chemical potential is introduced on the lattice, demonstrate the notorious problems arising when simulating finite density systems and present common approaches to overcome those difficulties.

In the following outline of the basics of LQCD we mainly follow the textbooks [41–43].

[1] Lattice spacings in temporal and different spatial directions do not necessarily have to be the same, but only isotropic lattices will be used in this thesis.

3.1 Gauge action

We will discuss the discretization of the gauge action first, since it is straightforward compared to the fermionic contribution. When working on a lattice, gauge fields are commonly represented as so called gauge links, which connect neighbouring lattice sites. $U_\mu(x)$ denotes the oriented connection between the sites x and $x + a\hat{\mu}$ and is related to the continuum gauge field via

$$U_\mu(x) = e^{igaA_\mu(x)}, \quad U_\mu(x) \in SU(3). \tag{3.1}$$

The inverse link, going from $x + a\hat{\mu}$ to x, is given by the adjoint matrix $U^\dagger_\mu(x)$. Under a local SU(3) rotation gauge links transform as [2]

$$U_\mu(x) \to W_x U_\mu(x) W^\dagger_{x+\mu} \quad W_x \in SU(3). \tag{3.2}$$

From this it is clear that, in order to construct a gauge invariant quantity, we need an ordered chain of link variables forming a closed loop. The simplest possibility to do so is the so called gauge plaquette, build from four link variables,

$$U_{\mu,\nu}(x) = U_\mu(x) U_\nu(x+\mu) U^\dagger_\mu(x+\nu) U^\dagger_\nu(x). \tag{3.3}$$

One can easily check that Tr $U_{\mu,\nu}(x)$ is invariant under the transformation eq. 3.2. The plaquette is the building block for the most commonly used gauge action, known as the Wilson gauge action. It consists of the sum over all plaquettes on the lattice [38],

$$S_g = \frac{\beta}{N_c} \sum_x \sum_{\mu<\nu} \text{Re Tr}(\mathbb{1} - U_{\mu,\nu}(x)) = \frac{\beta}{2N_c} \sum_P (\text{Tr}U_P + \text{Tr}U_P^\dagger), \quad \beta = \frac{2N_c}{g^2}, \tag{3.4}$$

and is therefore also gauge invariant. The lattice gauge coupling β is inverse to the squared continuum gauge coupling. This is the basis for the so called strong coupling expansion around $\beta = 0$, which will be discussed in chapter 4.2. Expanding eq. 3.1 for small lattice spacings and using the Baker-Campbell-Hausdorff formula, one can check that in the limit of $a \to 0$ we recover the continuum action,

$$S_g = \frac{1}{4} \int_0^{1/T} d\tau \int d^3x \; F^a_{\mu\nu} F^a_{\mu\nu} + \mathcal{O}(a^2). \tag{3.5}$$

Corrections due to finite lattice spacings are of order a^2 and are referred to as lattice artifacts. They determine how fast the lattice action converges to the continuum limit.

[2] When working on the lattice we will in the following usually write $x + \mu$ to denote a translation by one lattice spacing in direction $\hat{\mu}$, i.e. $x + \mu = x + a\hat{\mu}$.

The convergence can be improved by adding appropriate counterterms of order a^2, thus removing the leading lattice artifacts [44].

3.2 Fermion action

Deriving a discrete version of the fermionic action, eq. 2.3, is less obvious than discretizing the gauge action. The reason for this is explained by the No-Go-Theorem proved by Nielsen and Ninomiya [45], which states that it is impossible to formulate a fermion action on a 4 dimensional lattice that is chirally symmetric, local, has the desired number of fermion species and the correct continuum limit. Possible fermion actions differ in which of those desirable attributes they sacrifice.

We will start by demonstrating the appearance of unwanted fermion flavors, the so called doubling problem, in section 3.2.1. In section 3.2.2 we then introduce the Wilson fermions, which we will use in this thesis.

3.2.1 Fermion Doubling

The most straightforward way of discretizing fermions leads to what is called Naive Fermions. These are commonly used to demonstrate the problems arising with the discretization of fermions.

On the lattice fermion fields are represented by spinors located on the lattice sites,

$$\psi_x, \bar{\psi}_x, \quad x \in \Lambda. \tag{3.6}$$

Deriving a form of eq. 2.3 that is suitable for the lattice we first require a discretized field derivative,

$$\partial_\mu \psi_x \to \frac{\psi_{x+\mu} - \psi_{x-\mu}}{2a} + \mathcal{O}(a^2). \tag{3.7}$$

Under a $SU(3)$ transformation the fermion fields transform in the same way as in the continuum,

$$\begin{aligned} \psi_x &\to \psi_x^{'} = W_x \psi_x, \\ \bar{\psi}_x &\to \bar{\psi}_x^{'} = \bar{\psi}_x W_x^\dagger, \; W \in SU(3). \end{aligned} \tag{3.8}$$

Products of fermion fields at different lattice positions are therefore not gauge invariant. However, we can construct gauge invariant terms by connecting the fermion fields by gauge links. Comparing with the transformations eq. 3.2 we see that e.g. $\psi_x U_{\mu,x} \psi_{x+\mu}$ is a gauge invariant quantity. The simplest lattice fermion action is therefore constructed by discretizing the derivative in the continuum action, eq. 2.14, and adding gauge fields

to satisfy gauge invariance [3],

$$\begin{aligned} S_N &= \frac{1}{2a}\sum_{x,\mu}\Big[\bar{\psi}(x)\gamma_\mu U_\mu(x)\psi(x+\mu) - \bar{\psi}(x)\gamma_\mu U_\mu^\dagger(x-\mu)\psi(x-\mu)\Big] \\ &\quad + m\sum_x \bar{\psi}(x)\psi(x) \\ &= \sum_{x,y}\sum_{a,b,\alpha,\beta} \bar{\psi}_{\alpha,a}(x)Q(x|y)_{\alpha,\beta,a,b}\psi_{\beta,b}(y). \end{aligned} \tag{3.9}$$

The Dirac operator $Q(x|y)$ is defined as

$$Q(x|y)_{\alpha,\beta,a,b} = \sum_{\mu=1}^{4}(\gamma_\mu)_{\alpha,\beta}\frac{U_\mu(x)_{ab}\delta_{x+\mu,y} - U_\mu^\dagger(x-\mu)_{ab}\delta_{x-\mu,y}}{2a} + m\delta_{\alpha,\beta}\delta_{ab}\delta_{x,y}. \tag{3.10}$$

It can easily be checked that this action is invariant under the transformations 3.2 and 3.8. Nevertheless, it suffers from a flaw which becomes apparent when studying the limit of free quarks, which correspond to setting $U = \mathbb{1}$ for all gauge links. Setting $m = 0$ the free Dirac operator in momentum space is

$$Q(p) = \frac{i}{a}\sum_{\mu=1}^{4}\gamma_\mu \sin(p_\mu a) \overset{a\to 0}{=} i\sum_{\mu=1}^{4}\gamma_\mu p_\mu. \tag{3.11}$$

The discretized Dirac operator in momentum space is proportional to $\sin(p_\mu a)$. This is in contrast to the continuum version, which is linear in the momentum. The reason for this is that the lattice momentum has to be periodic in the Brillouin zone $(-\frac{\pi}{a}, \frac{\pi}{a}]$. Because of this the lattice propagator, $Q^{-1}(P)$, has 2^4 poles at $p = (0,0,0,0), ...(\pi/a, \pi/a, \pi/a, \pi/a)$, corresponding to 16 fermions. The fact that we ended up with 15 additional fermions, called doublers, when discretizing the fermion action is called the doubling problem.

3.2.2 Wilson Fermions

The fermion action proposed by Wilson sacrifices chiral symmetry in order to get rid of the doublers [46]. The idea is to add an additional term $\bar{\psi}Q_W\psi$ to the action, so that the Dirac operator for free massless fermions becomes

$$Q(p) = \frac{i}{a}\sum_{\mu=1}^{4}\gamma_\mu \sin(p_\mu a) + \mathbb{1}\frac{1}{a}\sum_{\mu=1}^{4}(1-\cos(p_\mu a)). \tag{3.12}$$

At the physical pole, $p_\mu = 0$, the additional term is zero, while for the doublers it acts like an additional mass term, being $\frac{1}{a}$ divergent as the continuum is approached. This causes the doublers to decouple from the theory. The modification is achieved by adding

[3] We will refrain from introducing chemical potential on the lattice until section 3.4.1.

a second order derivative like term to the naive fermion action,

$$S_W = r\bar{\psi}D_W\psi = -\frac{r}{2a}\sum_{n,\mu}\bar{\psi}_n(\psi_{n+\mu} - 2\psi_n + \psi_{n-\mu}). \tag{3.13}$$

This introduces a new parameter r, which we will set to be $r = 1$ as is commonly done. The Wilson action is usually restructured to be proportional to the so called hopping parameter, $\kappa_f = \frac{1}{2}(m_f a + 4)^{-1}$, by rescaling the quark fields as $\psi \to \sqrt{2\kappa_f}\psi$,

$$\begin{aligned} S = S_N + S_W = &\sum_x \bar{\psi}(x)\psi(x) \\ &- \kappa_f \sum_{x,\mu}\Big(\bar{\psi}_x(\mathbb{1} - \gamma_\mu)U_\mu(x)\psi_{x+\mu} + \bar{\psi}(x)(\mathbb{1} + \gamma_\mu)U^\dagger_\mu(x-\mu)\psi_{x-\mu}\Big). \end{aligned} \tag{3.14}$$

The corresponding Dirac operator is

$$\begin{aligned} Q[U] = \mathbb{1} + \kappa_f \sum_{i=1}^{3}\Big[&(\mathbb{1} + \gamma_i)U_i(x)\delta_{y,x+\hat{i}} + (\mathbb{1} - \gamma_i)U_i^\dagger(y)\delta_{y,x-\hat{i}}\Big] \\ -\kappa_f\Big[&e^{\mu}(\mathbb{1} + \gamma_4)U_4(x)\delta_{y,x+\hat{4}} + e^{-\mu}(\mathbb{1} - \gamma_4)U_i^\dagger(y)\delta_{y,x-\hat{4}}\Big]. \end{aligned} \tag{3.15}$$

This formulation is doubler free in the continuum, but even in the limit of massless quarks the Wilson term breaks chiral symmetry explicitly. In the limit $a \to 0$ Wilson fermions converge to the continuum action with $\mathcal{O}(a)$ lattice artifacts.

3.3 Numerical Methods

Now that we derived a suitable discrete version of the gauge and fermion action we want to proceed to derive observables. We do this by using the discretized version of eq. 2.17,

$$\langle\mathcal{O}\rangle = \frac{1}{Z}\int [dU][d\bar{\psi}][d\psi]\mathcal{O}\exp(-S_g[U] - \bar{\psi}Q[U]\psi). \tag{3.16}$$

Since on the lattice we work with a finite number of space-time points, this is a well defined quantity. While the link variables are SU(3) matrices, the fermion fields are formulated in terms of anticommuting numbers, and therefore are problematic to implement in a simulation. Using the Matthews-Salam formula [47, 48],

$$\int d^n\eta d^n\bar{\eta}\exp(\bar{\eta}_i Q_{ij}\eta_j) = \det[Q], \tag{3.17}$$

it is possible to integrate the fermionic fields out analytically. This leaves us with the so called fermion, or quark, determinant,

$$Z = \int [dU] \det Q[U] \exp(-S_g[U]). \tag{3.18}$$

Since the QCD action does not mix the different flavors, this can be done separately for each flavor,

$$\det Q[U] = \prod_{f=1}^{N_f} \det Q_f[U]. \tag{3.19}$$

In the case of N_f degenerate flavors, this reduces to $(\det M[U])^{N_f}$. After the integration the partition function and all observables can be expressed solely in terms of gauge links. The drawback is that the determinant in eq. 3.18 is a highly non-local object. Its computational cost is related to the number of lattice sites being correlated, which grows as quark masses are lowered, making simulations with physical quark masses expensive [49].

Since we are working on a finite lattice, the path integral over all gauge configuration is of finite dimension,

$$\int [dU] = \prod_{x,\mu,a} \int dU_{\mu,a}(x), \tag{3.20}$$

and can in theory be performed using standard numerical integration algorithms. Due to the large number of dimensions though, this is not possible on lattices with realistic sizes. Therefore efficient numerical methods are needed to evaluate the integral. In the next section we will present those that will be employed in this thesis, namely the Monte-Carlo method and the method of stochastic quantization.

3.3.1 Monte-Carlo Method

The most common method for solving high dimensional integrals is the Monte-Carlo Method, pioneered in the late 1940s by Ulam, von Neumann, Fermi and Metropolis [50].

When working with LQCD we are interested in solving integrals of the type [4]

$$\mathcal{O} = \frac{1}{Z} \int [dU] \exp(-S[U]). \tag{3.21}$$

The underlying idea of the Monte-Carlo Method is to sample only a small subset of possible lattice configurations and construct the result out of those samples. The crucial observation is that the integrals we are interested in will be sharply peaked for some regions of the configuration space where the action is minimal, while most configurations

[4] The fermion determinant in 3.18 can be included into the action as $\det Q = \exp(\log \det Q)$.

will have a large action and therefore be suppressed exponentially. This is linked to the observation that a statistical system realizes only a very small subset of all physical possible states, namely those that are close to being minimal in the energy.

Instead of sampling the integral with purely random or equidistantly distributed configurations, we therefore want to sample configurations distributed according to the probability distribution

$$P[U] \propto e^{-S[U]}. \tag{3.22}$$

This method is called importance sampling and ensures that we do not waste computation time generating configurations that have only a negligible contributions to the partition function. The creation of a suitable distribution is done via a Markov chain. Such a chain starts with a arbitrary configuration, from which new configuration are chosen in such a way that the transition probability to go from configuration U to $U^{'}$, expressed as $P(U \to U^{'})$, satisfies

$$\frac{P(U \to U^{'})}{P(U^{'} \to U)} = e^{S[U]-S[U^{'}]}. \tag{3.23}$$

This property is called detailed balance. Additionally one has to ensure that the whole configuration space can be reached, even if this may take an arbitrarily long amount of time. This property is called ergodicity. Those two conditions are sufficient to ensure that the distribution approaches the one in eq. 3.22 in the infinite time limit.

3.3.2 Metropolis Algorithm

There is still a considerable freedom in how detailed balance is achieved, leading to different Monte-Carlo algorithms. A common choice is the Metropolis method [51]. Here, we first generate a new state and calculate its action, $S[U^{'}]$. In order to fulfill detailed balance the state is accepted with the probability

$$P[U \to U^{'}] = e^{S[U]-S[U^{'}]} \tag{3.24}$$

if $S[U^{'}] > S[U]$, while always being accepted otherwise. If the configuration is accepted, it becomes the next element of the Markov chain. Otherwise, the next element will be identical to the previous one. The Metropolis algorithm does not specify how new configurations are generated, so any ergodic method is acceptable. The method of creating new configurations will have to be fine tuned to the model under consideration. A too high acceptance ratio means that successive states are closely correlated. A very low ratio causes the chain to frequently be stuck at a single configuration. Both cases lead to an inefficient sampling of the configuration space. While the optimal acceptance

rate will depend on the model, an accept ratio of $P \approx 0.23$ has been shown to be optimal in the limit of an infinite number of dimensions [52].

3.3.3 Stochastic Quantization

The method of stochastic quantization, or complex Langevin, offers an alternative approach to generate configurations from the desired distribution eq. 3.22. This method was pioneered by Parisi and Wu in 1981 [53]. A comprehensive review of stochastic quantization can be found in [54].

There are two equivalent formulations of stochastic quantization. The first uses the Langevin Equation, originally derived by Langevin for the description of Brownian Motion in 1908 [55], to evolve the systems degrees of freedom in a new, fictitious time θ. After that, observables are obtained as noise averages. In the other one derives expectation values with respect to a probability distribution, which evolves according to the Focker-Planck equation. We will concentrate on the first approach, since it is the approach commonly used for numerical treatment [56–61].

In the Langevin approach the desired distribution, eq. 3.22, is seen as the equilibrium distribution of a stochastic process, evolving in θ. In the limit $\theta \to \infty$ stochastic averages are then supposed to agree with vacuum expectation values. The stochastic process evolves according to the Langevin equation,

$$\frac{\partial \phi(x,\theta)}{\partial \theta} = -\frac{\partial S}{\partial \phi(x,\theta)} + \eta(x,\theta). \tag{3.25}$$

Here the scalar field ϕ represents a single degree of freedom, but generalizing this to multiple degrees of freedom per site or gauge links is straightforward [59]. $\eta(x,\theta)$ is a gaussian white noise term with the moments

$$\begin{aligned} \langle \eta(x,\theta) \rangle_\eta &= 0, \\ \langle \eta(x_1,\theta_1)\eta(x_2,\theta_2) \rangle_\eta &= 2\delta_{x_1,x_2}\delta_{\theta_1,\theta_2}. \end{aligned} \tag{3.26}$$

$\langle\rangle_\eta$ denotes noise averages. They are calculated as

$$\langle \phi(x_1,\theta_1),...,\phi(x_n,\theta_n) \rangle_\eta = \frac{\int D\eta \ \phi(x_1,\theta_1),...,\phi(x_n,\theta_n) \exp(-\frac{1}{4}\int d^n x \ d\tau \eta^2)}{\int D\eta \exp(-\frac{1}{4}\int d^n x \ d\tau \eta^2)}. \tag{3.27}$$

The two point correlator, eq. 3.26, shows that the noise is uncorrelated in time, reflecting the Markov property of the stochastic process. Note that, for $\eta = 0$, we recover the classical field equation,

$$\frac{\partial S}{\partial \phi(x,t)} = 0. \tag{3.28}$$

The assertion of the Complex Langevin method is that correlation functions become equal to the corresponding quantum Greens functions as $\theta \to \infty$,

$$\lim_{\theta\to\infty} \langle (x_1)...\phi(x_n)\rangle_\eta = \langle \phi(x_1)...\phi(x_n)\rangle. \tag{3.29}$$

This equivalence can be shown to be true in the case of real actions [62, 63]. Nevertheless, the possibility to apply stochastic quantization to problems involving complex actions is its most attractive feature. This also makes it possible to apply it to quantize systems in Minkowskian space-time [64]. Often problems due to numerical instabilities arise, those can be solved by applying an adaptive stepsize when discretizing eq. 3.25 [65].

We will apply stochastic quantization to systems with finite fermion densities, where complex actions appear. The problems of finite density systems and the application of stochastic quantization to such systems are discussed in section 3.4.

3.3.4 Data Analysis

After we generated an ensemble of configurations, following any of the aforementioned methods, we can estimate observables by averaging over their values on said configurations,

$$\mathcal{O} = \frac{1}{N}\sum_{i}^{N} \mathcal{O}[U^{(i)}]. \tag{3.30}$$

This gives an estimate of eq. 3.16 respectively eq. 3.27. We can estimate the error of $\mathcal{O}$ by resampling. This means we randomly choose N configurations of our original sample, allowing for multiple draws of the same configuration, to create a new ensemble. Calculating the observable on each configuration we get a set of K estimates $\mathcal{O}^k$, which we then can use to estimate the standard deviation of $\mathcal{O}$,

$$\sigma^2_{\mathcal{O}} = \frac{1}{K}\sum_{k=1}^{K} \left(\mathcal{O}^k - \mathcal{O}\right)^2. \tag{3.31}$$

This method is known as bootstrapping. It assumes that the data is uncorrelated, i.e. that for observables calculated on successive configurations we have

$$C_{\mathcal{O}}(t) = \langle \mathcal{O}_i \mathcal{O}_{i+t}\rangle - \langle \mathcal{O}_i\rangle\langle \mathcal{O}_{i+t}\rangle = 0. \tag{3.32}$$

This will not be the case in most simulations, where configurations are usually generated by making small changes to the previous element in the Markov chain. We therefore will have to deal with autocorrelation between successive configurations. The autocorrelation

strength is estimated by looking at the function

$$\Gamma_{\mathcal{O}} = \frac{C_{\mathcal{O}}(t)}{C_{\mathcal{O}}(0)} \propto \exp(-\frac{t}{\tau_{\mathcal{O}}}). \tag{3.33}$$

The value $\tau_{\mathcal{O}}$ is called autocorrelation time. In order to avoid underestimating statistical errors only configurations separated by $\mathcal{O}(\tau_{\mathcal{O}})$ should be used for the evaluation of observables.

3.4 Finite Density

In this section we will consider systems with a finite fermion density. We discuss the introduction of chemical potential on the lattice and the so called sign problem. This problem, arising from the fact that the action describing a finite density system is necessarily complex, makes finite density simulations extremely challenging. We will discuss different approaches that were developed to avoid this problem.

3.4.1 Chemical Potential on the Lattice

In the continuum finite density was introduced by coupling the chemical potentials μ_i to the respective quark numbers $N_i = \int d^4x \ \bar{\psi}_i \gamma_4 \psi_i$, cf. eq. 2.14. The naive introduction of a term $\mu_i \gamma_4$ into the Dirac operator eq. 3.14 leads to a divergent energy density [41]. Chemical potential on the lattice is therefore introduced by multiplying the temporal gauge links in the Dirac operator by a suitable function $f(a\mu)$. The function is chosen in a way such that $f(0) = 1$ reproduces the zero density theory and $f(a\mu) = 1/f(-a\mu)$ ensures time reflection invariance. Furthermore we want to have $f(a\mu) = 1 + a\mu + \mathcal{O}(a\mu)^2$ to recover the coupling of the chemical potential to the density term, $\mu\bar{\psi}\gamma_4\psi$, in continuum limit. This leaves $f(a\mu) = \exp(a\mu)$ as the obvious choice. We therefore multiply gauge links going forward in time with a factor $\exp(a\mu)$ while multiplying links going backwards in time with $\exp(-a\mu)$,

$$\begin{aligned} U_\nu &\to e^{\delta_{\nu,4} a\mu} U_\nu, \\ U_\nu^\dagger &\to e^{-\delta_{\nu,4} a\mu} U_\nu^\dagger. \end{aligned} \tag{3.34}$$

This introduces a quark-anti-quark asymmetry, thus favouring the existence of quarks over antiquarks if $\mu > 0$. While the introduction of chemical potential on the lattice is straightforward, its presence leads to the infamous sign problem that we will discuss next.

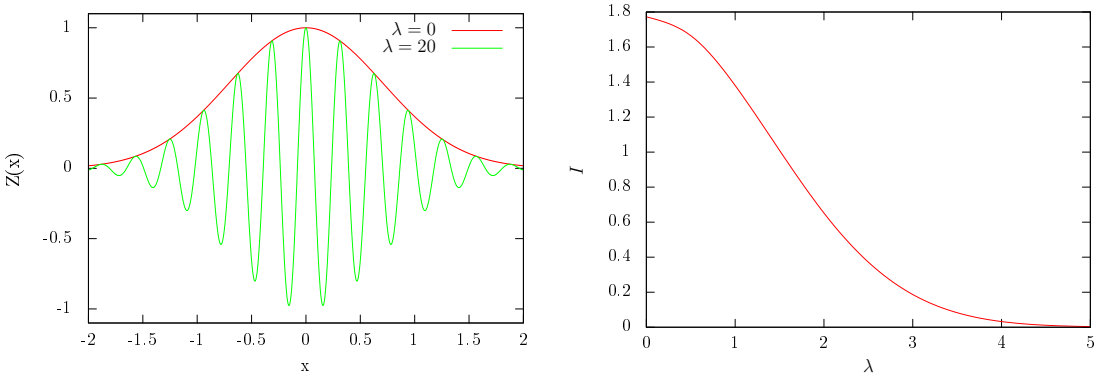

FIGURE 3.1: Left: Real part of the Boltzmann factor in eq. 3.39 for $\lambda = 0$ (no sign problem) and $\lambda = 20$ (strong sign problem). Right: Value of the integral eq. 3.39 vs. λ.

3.4.2 Sign Problem

Monte-Carlo techniques relying on importance sampling are the method of choice in solving high dimensional integrals, but the interpretation of the Boltzmann weight as a probability fails when we introduce a finite chemical potential [66]. The reason for this lies in the fermionic determinant. We start with the observation that the Dirac operator, $\not{D}$, is γ_5 hermitian, i.e.

$$\gamma_5 \not{D} \gamma_5 = \not{D}^\dagger. \tag{3.35}$$

If we neglect chemical potential, we therefore can write

$$\det[\gamma_5(\not{D} + m)\gamma_5] = \det[(\not{D} + m)] = \det[(\not{D} + m)^\dagger] = \det[(\not{D} + m)]^*, \tag{3.36}$$

which shows that the determinant has to be real. However, including μ we have

$$\gamma_5(\not{D} + m + \mu\gamma_4)\gamma_5 = (\not{D} + m - \mu\gamma_4) = (\not{D} + m - \mu^*\gamma_4)^\dagger. \tag{3.37}$$

After taking the determinant this gives

$$\det[(\not{D} + m + \mu\gamma_4)] = \det[(\not{D} + m - \mu^*\gamma_4)]^* \tag{3.38}$$

demonstrating that the determinant does not has to be real for $\mu \neq 0$. Indeed it can be shown that it has to be complex in order to produce the expected features of finite density physics [66].

The problem of having a complex determinant can easily be demonstrated using a toy model. Consider the partition function

$$Z = \int dx\ e^{-x^2+i\lambda x}. \tag{3.39}$$

Since thermodynamical quantities are real, we know that the partition function has to be real too. Therefore, we can assume that the imaginary contributions cancel out and concentrate on the real part of the integrand. The left side of fig. 3.1 shows that the real part of the integrand in eq. 3.39 has negative contributions for sufficiently large values of λ. This spoils the interpretation of the Boltzmann factor as a probability, like we did in eq. 3.22, making the use of importance sampling impossible.

The left side of fig. 3.39 shows that in our toy model the value of Z goes to zero for large λ. This is an effect of the cancellations between positive and negative contributions. It is therefore necessary to sample the whole x range in order to give a reliable estimation of Z. This is not feasible when evaluating partition functions one encounters in LQCD.

3.4.3 Silver Blaze

A phenomenon that is closely related to the sign problem is the Silver Blaze property [67, 68]. This denotes the fact that at $T = 0$ the QCD partition function, and therefore all thermodynamical observables, are independent of μ as long as $\mu_B < \mu_c = m_B - \epsilon$, with ϵ being the nuclear binding energy. μ_c is the energy required to produce a baryon at rest, therefore there is not enough energy available to create baryons below this threshhold and the system remains in its vacuum state. This is despite the fact that μ_B explicitly enters the fermion determinant and changes the eigenvalues of the Dirac operator. Below μ_c cancellations have to take place that cause the partition function to be independent of μ.

3.5 Solving the Sign Problem

In the last section we showed how the introduction of a finite chemical potential leads to a complex fermion determinant. Since this makes the use of standard Monte-Carlo Methods impossible, most of the QCD phase diagram is inaccessible to such methods.

Different approaches have been developed in recent years in order to circumvent this problems, for an overview see e.g. [66]. Some of them, like reweighting [69], Taylor expansion [70] and analytic continuation from imaginary chemical potential [29], work only in the region where μ/T is small. Others, like quenched or phase quenched QCD [71], avoid the sign problem completely but inherently differ from full LQCD. An especially promising approach is the use of stochastic quantization, which has recently been applied to full LQCD at large chemical potentials [61]. However, there are known cases

where stochastic quantization produces wrong results [72–75]. No method that both works for all values of the chemical potential and is guaranteed to give correct results is known.

3.5.1 Phase Quenched QCD

Early LQCD simulations employed the so called quenched approximation, which consists of approximating the fermion determinant with a gauge field independent constant [76]. A more elaborated approximation is phase quenched LQCD [77]. In this approximation the phase of the quark determinant, $\det(Q) = e^{i\phi}|\det(Q)|$ is neglected and simulations are performed with the absolute value of the determinant. If we take $N_f = 2$ degenerate quarks, up and down, we can use eq. 3.38 to write the partition function in the phase quenched approximation as

$$Z = \int [dU] \; |\det Q|^2 e^{-S_g} = \int [dU] \det Q(\mu) \det Q(-\mu) e^{-S_g}. \tag{3.40}$$

This is equivalent to simulating with finite isospin chemical potential, $\mu_{\rm iso} = \mu_u = -\mu_d$. In contrast to quark or baryon chemical potential, introducing a asymmetry between particles and antiparticles, $\mu_{\rm iso}$ introduces an asymmetry between up and down quarks.

At a value of $\mu_{\rm iso} = \frac{m_\pi}{2}$ a transition to a finite density region due to the formation of a pion condensate takes place. This is in contrast to the case of baryon chemical potential, where the transition to finite density does not happen until $\mu_B = \frac{m_B}{3}$ [67]. This gap demonstrates that the phase quenched approximation leads to a significantly different phase diagram compared to QCD with baryon chemical potential.

3.5.2 Reweighting

Reweighting is a technique that can be used to circumvent the problem arising from negative weights in the partition function by reformulating the partition function [28, 78]. Writing the quark determinant as

$$\det(Q) = |\det Q| e^{i\theta} \tag{3.41}$$

and introducing a positive function $f[U]$ into the partition function, we can write

$$\begin{aligned} \langle \mathcal{O} \rangle_{\det(Q)} &= \frac{1}{Z_{\det(Q)}} \int [dU] \mathcal{O} \; \det(Q) \; e^{-S} \\ &= \frac{\int [dU] \mathcal{O} \; e^{-S} \; \frac{e^{i\theta}}{f} f}{\int [dU] e^{-S} e^{i\theta} \; \frac{f}{f}} = \frac{\langle \mathcal{O} \; \frac{e^{i\phi}}{f} \rangle_f}{\langle \frac{e^{i\phi}}{f} \rangle_f}. \end{aligned} \tag{3.42}$$

In the second step the absolute value of the determinant was included into the action, $S = S_g - \log(|\det(Q)|)$. $\langle ... \rangle_f$ denotes expectation values derived with the (positive)

weight $e^{-S+\log(f)}$, while $\langle ... \rangle_{\det(Q)}$ is the expectation value obtained with the full action, $S = S_g - \log(\det(Q))$.

After this reformulation we can express an expectation value at $\mu \neq 0$ in terms of expectation values obtained from a integral over a strictly positive weight. This is possible because we absorbed the fluctuating parts of the determinant into the observables. This method of reweighting is not restricted to chemical potential, originally it was used for calculating expectation values over a range of the lattice coupling β from a single simulation, a technique known as Ferrenberg-Swendsen Reweighting [79].

Reweighting works well as long as the distribution we are interested in is not too different from the one we are sampling. The overlap between the two distributions is determined by the choice of f. The optimal choice, in the sense that it minimizes the statistical error of the denominator in eq. 3.42, is $f = |\cos(\theta)|$ [80]. This results in $\langle \frac{e^{i\phi}}{f} \rangle$ becoming the average sign of $\cos(\theta)$.

The severity of the problem of sampling a distribution that is significantly different from the desired distribution becomes clear when we rewrite the denominator as a ratio between the partition function with weight $\det(M)$ and weight f,

$$\langle \frac{e^{i\phi}}{f} \rangle_f \overset{V \to \infty}{=} e^{-\frac{V}{T}\Delta f} \tag{3.43}$$

with Δf being the free energy density difference between both ensembles. This means the denominator will exponentially approach zero as the volume or the free energy density difference, which is a function of $\frac{\mu}{T}$, increases, causing the statistical error to grow exponentially. The cause for this is the small overlap between the desired and the sampled function and is therefore called the overlap problem. This restricts the technique of reweighting to small volumes and small values of $\frac{\mu}{T}$.

3.5.3 Imaginary Chemical Potential

Another method to explore the phase diagram at finite density is the use of simulations at imaginary chemical potential [19, 29, 82, 83]. As can be seen in eq. 3.38 the determinant will be real if we chose a purely imaginary chemical potential $\mu_i = i\mu$. In this case we have $\mu_i^* = -\mu_i$ and the determinant will be real again, allowing for the use of standard Monte-Carlo methods. The fact that the region of real and imaginary chemical potential are connected analytically then allows the results to be extrapolated by means of an analytic continuation.

To demonstrate this we look at the left hand side of fig. 3.2, showing the so called Columbia plot. It shows the order of the deconfinement/chiral transition depending on the masses of the three lightest quarks. On the right side the same plot is extended to account for chemical potential at real and imaginary values. Because of the symmetry

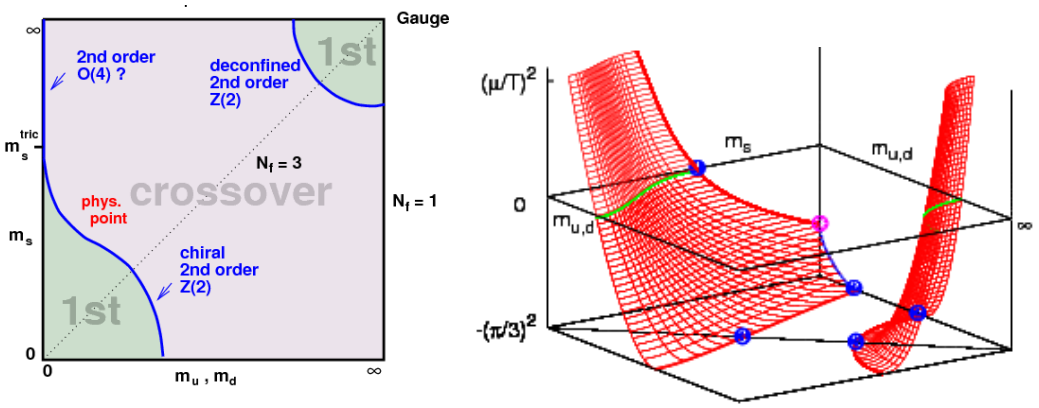

FIGURE 3.2: Left side: Columbia plot, showing order of the deconfinement/chiral transition for different values of the quark masses [81]. Right side: Same plot, but extended in the third dimension to account for real and imaginary chemical potential [81].

discussed in section 2.3.3 the phase diagram repeats itself if one goes beyond $\frac{\mu_i}{T} = \frac{\pi}{3}$, so fig. 3.2 shows the complete phase diagram for imaginary chemical potential.

An example for the use of analytic continuation is the question regarding the order of the transition for $N_f = 2$ chiral quarks at $\mu = 0$ [83]. Determining the critical points for different values of μ_I allowed to determine that, for coarse lattices, the $N_f = 2$ chiral limit lies inside the first order region. Another example is the search for the QCD critical endpoint at finite chemical potential. Investigating the location and curvatures of the chiral critical surface at finite μ_I can be used to extrapolate how the surface will continue at real μ [84]. Nevertheless, this method can only make statements on critical surfaces that extend into the region of imaginary chemical potential, and naturally becomes less reliable the further we extrapolate into the region of real chemical potential.

3.5.4 Stochastic Quantization with Complex Action

While $\mu \neq 0$ makes the use of standard importance sampling impossible, it is straightforward to apply eq. 3.25 to a complex action. Since this means that derivatives of the action with respect to the degrees of freedom, the so called drift terms, are complex all degrees of freedom will become complex too. In the case of LQCD the degrees of freedom are the gauge links. The presence of a complex action means that they are no longer restricted to the $SU(3)$ group but belong to the larger $SL(3,\mathbb{C})$ group[5]. In the case of physical observables those imaginary contributions will average out after taking the noise average, see eq. 3.27.

While being successful in solving different models with complex action [56, 58, 59], stochastic quantization has been shown to fail in other cases when the systems become unbounded in the complex plane [72–75]. Efforts have been made in recent years to

[5] $SL(N,\mathbb{C})$ denotes the group of N × N matrices with complex entries and determinant 1. It contains $SU(N)$ as a subgroup

formulate a criterion to decide whether the Complex Langevin process converges to the correct distribution [85, 86], but the reasons causing stochastic quantization to fail are not yet fully understood.

Stochastic quantization can also be applied to full LQCD. This gets complicated by the fact that, under the evolution eq. 3.25, the system will spend most of the time exploring the complex plane, slowing the simulation down. Recently this problem has been overcome by introducing the so called gauge cooling, designed to keep the gauge links as close as possible to the $SU(3)$ group [61, 87].

Chapter 4

An Effective Theory for QCD

In this chapter we will derive an effective theory for lattice QCD (LQCD) with heavy quarks, expanding on the work done in [88–90]. Parts of the results presented here have already been published in [91, 92].

The purpose of the effective theory is to reproduce LQCD in a relevant parameter region. The theory we are about to derive can be improved systematically and is easier to solve numerically than LQCD. Of special interest is the cold and dense region, which is inaccessible for LQCD due to the sign problem, see section 3.4.2. The resulting theory still suffers from the sign problem, but can be solved using either the method of stochastic quantization, see section 3.3.3, or Monte-Carlo with reweighting, see section 3.5.2. The numerical results can be found in chapter 5. Furthermore, as will be demonstrated in chapter 6, the theory can also be treated analytically.
The derivation of the effective theory will be organized as follows: In section 4.1 we outline our general strategy. In section 4.2 we show how the pure gauge part is expanded in a strong coupling expansion. Section 4.3 is concerned with the expansion of the fermion determinant by means of a hopping parameter expansion. Gauge corrections that come from mixing between both expansions are introduced in section 4.4. Finally, we discuss how to resum the effective action in section 4.5, the introduction of multiple flavors in section 4.6 and how the theory simplifies when go into the cold dense limit in section 4.7.

4.1 Effective Action

Starting point for the derivation is LQCD in (3+1) dimensions with the Wilson gauge and the Wilson fermion action, see eq. 3.4 and eq. 3.14 respectively. With N_f flavors we have

$$Z = \int [dU_\mu] \prod_{f=1}^{N_f} \det Q_f e^{-S_g}, \qquad S_g = \frac{\beta}{2N_c} \sum_P (\mathrm{Tr} U_P + \mathrm{Tr} U_P^\dagger). \tag{4.1}$$

We derive the effective theory in two steps. First, we perform a series expansion of both the fermion determinant and the gauge action. In the case of the gauge action this happens via a strong coupling expansion around the limit $\beta \to 0$. The determinant is expanded in a hopping parameter expansion around the static quark limit, $\kappa = 1/(2am_q + 8) \to 0$.

The expansion allows us, as a second step, to perform the gauge integration over the spatial gauge links analytically, leaving us with an action that solely depends on temporal link variables. We call this the effective action S_{eff},

$$Z_{\text{eff}} = \int [dU_4] e^{-S_{\text{eff}}}, \quad S_{\text{eff}} = \ln \int [dU_i] \prod_{f=1}^{N_f} \det Q^f e^{-S_g}. \tag{4.2}$$

This will allow us to change the integration measure to an integral over Polyakov Loops,

$$\int [dU_4] \to \int [dL], \quad L(\vec{x}) = \text{Tr } W(\vec{x}) = \text{Tr} \prod_{\tau=0}^{N_\tau - 1} U_4(\vec{x}, \tau). \tag{4.3}$$

The resulting theory is three dimensional and has a significantly reduced number of degrees of freedom compared to the original theory. Nevertheless, the reliance on expansions means that our theory approximates LQCD only in a finite parameter region in β and κ.

4.2 Strong coupling expansion

The expansion of the pure gauge action was already done in [89]. Since in this thesis we do not expand on these results we will only briefly review them. New results regarding gauge corrections coming from mixing terms between hopping and strong coupling expansion will be shown in section 4.4.

The natural limit to consider on the lattice is the opposite of the weak coupling expansion in the continuum, i.e. that of vanishing lattice coupling $\beta = \frac{2N_c}{g^2} \to 0$. Since β determines the lattice spacing, we will discuss this in section 5.6.2, this is also the limit of large lattice spacings. By making use of the character expansion [42, 93] we can write the effective action as

$$-S_{\text{eff}} = \ln \int [dU_i] \prod_p [1 + \sum_{r \neq 0} d_r a_r(\beta) \chi_r(U_p)]. \tag{4.4}$$

The sum extends over all irreducible representations r. Each representation has a dimension d_r, a character χ_r and an expansion parameter $a_r(\beta)$. While it is possible to have non-vanishing terms that do not wind through the temporal boundary of the lattice, i.e. by constructing a cube out of six gauge plaquettes, those terms will become

independent of the link variables after performing the spatial link integration. Since constant contributions to the partition function cancel out when calculating expectation values, we can neglect those graphs.

The leading contribution is obtained by neglecting spatial plaquettes, i.e. plaquettes that contain no temporal links. This limit leaves only chains of plaquettes looping through the temporal boundary as a possible contribution. The spatial link integration can then be performed with the group integral

$$\int dU \chi_r(XU)\chi_s(U^{-1}Y) = \frac{\delta_{rs}}{d_r}\chi_r(XY), \tag{4.5}$$

which enforces all plaquettes of a graph to belong to the same representation. Since, when considering a chain of plaquettes, we have one spatial link integral per plaquette the factor d_r cancels, and we are left with

$$-S_{\text{eff}} = \ln \prod_{<ij>} [1 + \sum_{r\neq 0} [a_r(\beta)]^{N_\tau} \chi_r(W_i)\chi_r(W_j)]. \tag{4.6}$$

This describes a nearest neighbour interaction between Polyakov loops in all representations. The leading order contribution comes from the fundamental representation, where $a_f = u = \frac{\beta}{18} + \mathcal{O}(\beta^2)$ [1],

$$-S_{\text{eff}} = \sum_{<i,j>} \ln[1 + \lambda_1(L_i^* L_j + L_i L_j^*)], \quad \lambda_1 = u^{N_\tau} + O(u^{N_\tau+4}). \tag{4.7}$$

The corrections to λ_1 come from additionally including spatial plaquettes and are known up to order $u^{N_\tau+10}$ [89].

Interactions between Polyakov loops in higher representations start at higher order in u. The next contribution comes from the interaction between loops in the adjoint representation,

$$-S_{\text{eff}} = \sum_{<ij>} \log(1 + \lambda_a(\chi(W_i)\chi(W_j))), \quad \lambda_a = \frac{9}{8}u^{2N_\tau} + \mathcal{O}(u^{2N_\tau+1}) \tag{4.8}$$

with $\chi_a(W_i) = |L|^2 - 1$ [94]. Corrections to the coupling λ_a, again originating from the introduction of spatial plaquettes, are known up to order $u^{2N_\tau+6}$ [89]. Contributions from higher representations have also been investigated in [95].

Interaction over larger distances, i.e. next to nearest neighbours, begin at distance $\sqrt{2}a$ and with order $u^{2N_\tau+2}$,

$$-S_{\text{eff}} = \sum_{<k,l>} \log(1 + \lambda_2(L_k L_l^* + L_k^* L_l)), \quad \lambda_2 = u^{2N_\tau+2} + \mathcal{O}(u^{2N_\tau+4}). \tag{4.9}$$

[1] Higher orders of a_f up to $\mathcal{O}(\beta^{14})$ can be found in [42]

The effects of long range interaction in the effective theory was investigated in [96]. In [90] it was shown that already the one coupling model, which only includes λ_1, is sufficient to determine the continuum pure gauge deconfinement temperature as $T_c = 250(14)$MeV. Since the pure gauge deconfinement transition is of first order, perturbation theory will break down in the deconfined phase. This sets the limit for the temperature range that can be described by the effective theory. All thermodynamical quantities inside of this range are described well, while correlation functions suffer from neglecting larger distance interaction terms [96].

4.3 Hopping Parameter Expansion

We will now proceed to perform the expansion of the quark determinant around the limit of static quarks, i.e. $\kappa = 0$ [42]. We will first perform the expansion in the strong coupling limit, i.e. $\beta = 0$. The pure gauge contribution shown in the last section can be included independently from the results shown here. Mixing terms, coming from graphs that receive contributions from both the strong coupling and the hopping parameter expansion, will be discussed in section 4.4.

We begin the hopping parameter expansion with the Wilson Dirac operator, eq. 3.15, which we rewrite as

$$Q_f[U] = \mathbb{1} - \kappa_f M[U], \tag{4.10}$$

with the hopping matrix $M[U]$. The quark determinant is then expanded as

$$\det[\mathbb{1} - \kappa_f M] = \exp(\mathrm{Tr}\log[\mathbb{1} - \kappa_f M]) = \exp\Big(\sum_{l=1}^{\infty} \frac{\kappa_f}{l} \mathrm{Tr} M^l\Big) \tag{4.11}$$

Due to the Kronecker deltas in eq. 3.15 only closed loops, build out of consecutive links, will give a non-vanishing contribution. The hopping expansion therefore is an expansion in terms of closed quark lines of length l.

4.3.1 Static quark determinant

The first step in our derivation is the calculation of the static quark determinant. This is the part of the determinant that describes static, i.e. infinitely heavy, quarks. All corrections to this limit are contained in the remainder part, which we call kinetic determinant. As we will see the static part of the determinant can be calculated exactly. The kinetic part will later be derived order by order in $\kappa \propto \frac{1}{m_q}$.

We begin by splitting up $M[U]$ into temporal and static hoppings [2]. For the sake of simplicity we will first treat the $N_f = 1$ case and drop the flavor index. The introduction of multiple flavors will be postponed to section 4.6. We split up the hopping matrix to rewrite the determinant as

$$\det_{c,s,x} Q_{x,y} = \det[\mathbb{1} - T^+_{x,y} - T^-_{x,y} - \sum_{i=1}^{3} S^+_{x,y,i} - \sum_{i=1}^{3} S^-_{x,y,i}]. \tag{4.12}$$

Here we also introduced the indices c,s and x to show the determinant to be in color, spin and coordinate space. The respective hopping terms are

$$\begin{aligned} S^+_{x,y,i} &= \kappa(\mathbb{1} - \gamma_i)U_i(x)\delta_{y,x+i}, \\ S^-_{x,y,i} &= \kappa(\mathbb{1} + \gamma_i)U_i^\dagger(y)\delta_{y,x-i}, \\ T^+_{x,y} &= \kappa e^{a\mu}(\mathbb{1} + \gamma_4)U_4(x)\delta_{y,x+\hat{4}}, \\ T^-_{x,y} &= \kappa e^{-a\mu}(\mathbb{1} - \gamma_4)U_4^\dagger(y)\delta_{y,x-\hat{4}}. \end{aligned} \tag{4.13}$$

These matrices only have non-vanishing entries for positions x and y that are nearest neighbours. We will therefore in the following use the notation $S_{x,y,i} = S_{x,x+i}$ in order to reduce the number of indices. Rewriting the hopping matrix like in eq. 4.12 allows us to split up the fermion determinant into a static and a kinetic part,

$$\det_{c,s,x} Q = \det Q_{\text{stat}} \det Q_{\text{kin}}, \quad \det Q_{\text{stat}} = \det[\mathbb{1} - T^+_{xy} - T^-_{xy}]. \tag{4.14}$$

For now, we are only interested in the static determinant, therefore we will postpone all considerations regarding the kinetic part to section 4.3.2.

The delta functions in eq. 4.13 mean that we will only have non-vanishing contributions for closed quarks lines. As long as we are in the static limit, where we neglect spatial hops, the only possibility to form a closed quark line is by looping around the lattice through the temporal boundary. Such a loop is equivalent to a temporal Wilson line, i.e. an untraced Polyakov loop, cf. eq. 4.3. Using this we can, after inserting the definition for the temporal hoppings and using the fact that $(\mathbb{1} + \gamma_4)^2 = 2(\mathbb{1} + \gamma_4)$, calculate the coordinate space determinant and get

$$\det_{c,s,x} Q_{\text{stat}} = \prod_{\vec{x}} \det_{c,s}[\mathbb{1} + \frac{1}{2}(2\kappa)^{N_\tau} e^{N_\tau a\mu}(\mathbb{1} + \gamma_4)W_x] \det_{c,s}[\mathbb{1} + \frac{1}{2}(2\kappa)^{N_\tau} e^{-N_\tau a\mu}(\mathbb{1} - \gamma_4)W_x^\dagger]. \tag{4.15}$$

The additional minus sign compared to eq. 4.14 is caused by the antiperiodic temporal boundary conditions. In order to evaluate the spin determinant we use fact that $\det_s[\mathbb{1} +$

[2] We will in the following use the expression "hopping" to refer to the terms given in eq. 4.13, i.e. a quark line connecting neighbouring lattice sites.

$\alpha(1 \pm \gamma_\mu)] = [\mathbb{1} + 2\alpha]^2$. We get

$$\det_{c,s,x} Q_{\text{stat}} = \prod_{\vec{x}} \det_c [\mathbb{1} + h_1(\mu, N_\tau) W_x]^2 \det_c [\mathbb{1} + h_1(\mu, N_\tau) W_x^\dagger]^2. \tag{4.16}$$

Here we have introduced the effective couplings for static quarks and anti-quarks,

$$\begin{aligned} h_1 &= (2\kappa)^{N_\tau} e^{N_\tau a\mu} = e^{N_\tau(a\mu + \ln(2\kappa))} \\ \bar{h}_1 &= (2\kappa)^{N_\tau} e^{-N_\tau a\mu} = e^{N_\tau(-a\mu + \ln(2\kappa))}. \end{aligned} \tag{4.17}$$

Both couplings will receive gauge corrections once we leave the strong coupling limit, see section 4.4. The color determinant can be computed from the fact that for a SU(3) matrix U we can write [97]

$$\det_c [\mathbb{1} + \alpha U] = 1 + \alpha \text{Tr} U + \alpha^2 \text{Tr} U^\dagger + \alpha^3. \tag{4.18}$$

Using this relation we get the final expression for the static quark determinant,

$$\det_{c,s,x} Q_{\text{stat}} = \prod_{\vec{x}} (1 + h_1 L_{\vec{x}} + h_1^2 L_{\vec{x}}^\dagger + h_1^3)^2 (1 + \bar{h}_1 L_{\vec{x}}^\dagger + \bar{h}_1^2 L_{\vec{x}} + \bar{h}_1^3)^2. \tag{4.19}$$

The new degrees of freedom are now traces over temporal Wilson lines, i.e. Polyakov loops, $L = \text{Tr } W$.

As the final step we now have to perform the integration over spatial links, but since we neglected those in order to obtain the static limit this does not change the result. The partition function for a system of static quarks in the strong coupling limit is therefore

$$\begin{aligned} Z &= \int [dU_4] e^{-\int [dU_i]\ S_{\text{stat}}} \\ &= \int [dU_4] \prod_{\vec{x}} (1 + h_1 L_{\vec{x}} + h_1^2 L_{\vec{x}}^\dagger + h_1^3)^2 (1 + \bar{h}_1 L_{\vec{x}}^\dagger + \bar{h}_1^2 L_{\vec{x}} + \bar{h}_1^3)^2 \end{aligned} \tag{4.20}$$

This partition function describes a system of static quarks and converges to full LQCD only in the limit of $\kappa \to 0$, i.e. the infinite quark mass limit. To populate the lattice with (anti)-quarks we have to take the limit $a\mu \to \infty(-\infty)$, while keeping the coupling constant $h_1(\bar{h}_1)$ fixed. Note that in this limit it is only possible to have either quarks or anti-quarks on the lattice, because at least one of the coupling constants is always zero. As will be discussed in section 5.1, the Polyakov loops L can be parameterised in terms of two angles, so eq. 4.20 describes a three dimensional spin model. This action, including leading orders of the pure gauge contributions discussed in section 4.2, has been studied as an effective theory for heavy quark QCD at finite chemical potential before, using Complex Langevin dynamics to avoid the sign problem [56, 57, 59, 60]. It is also possible to recast it into a flux representation that is sign problem free [90, 98].

As we will discuss in chapter 6 we can also compute this partition function analytically.

4.3.2 Kinetic Quark Determinant to Leading Order

We are now ready to expand the kinetic part of the determinant, which we split off in eq. 4.14. The determinant, after factoring out the static part, becomes

$$\begin{aligned}\det Q &= \det Q_{\text{stat}} \det Q_{\text{kin}} \\ &= \det[\mathbb{1} - T_{x,y}] \det[\mathbb{1} - \frac{S^+_{x,x+i} + S^-_{x,x+i}}{\mathbb{1} - T}] \\ &= \det[\mathbb{1} - T_{x,y}] \det[\mathbb{1} - P - M], \end{aligned} \tag{4.21}$$

with the abbreviation $T_{x,y} = T^+_{x,y} + T^-_{x,y}$. We introduced two new quantities, $P = P_{x,i}$ and $M = M_{x,i}$. They contain the static quark propagator, $(\mathbb{1} - T_{x,y})^{-1}$, followed by a spatial hopping to a neighbouring lattice site. Our first step is therefore to calculate the static propagator, after that we will be able to expand the kinetic quark determinant as

$$\det[\mathbb{1} - P - M] = \exp(\text{Tr} \sum_{n=1}^{\infty} [-\frac{1}{n}(P + M)^n]). \tag{4.22}$$

The leading order in the expansion of the kinetic determinant consists of truncating the sum in eq. 4.22 at $n = 2$. Since an equal number of P and M is required in order to form a closed loop [3] the $n = 1$ term as well as the $n = 2$ contributions proportional to PP and MM vanish. Each spatial hopping comes with a factor of κ, we therefore find the leading contribution to be of order $\mathcal{O}(\kappa^2)$ [4]. We get

$$\det Q_{\text{kin}} = \exp\Big(- \sum_{ij} \text{Tr} P_i M_j + \mathcal{O}(\kappa^4)\Big). \tag{4.23}$$

The requirement of closed loops means that we can set $i = j$, i.e. forward and backward hoppings happen in the same spatial direction. To find the expressions for P and M we need to calculate the static quark propagator $Q^{-1}_{\text{stat}} = (\mathbb{1} - T^{-1}_{x,y})$. This is simplified by the observation that graphs involving backtracking, i.e. 180° turns, give no contribution since $(\mathbb{1} + \gamma_\mu)(\mathbb{1} - \gamma_\mu) = 0$. We can therefore split the static propagator into forward

[3] This is not true when we consider finite lattices with periodic boundary conditions, but since we are interested in the thermodynamical limit we will neglect finite size corrections.

[4] This convention of course neglects the fact that h_1 and $\bar{h}_1$ are already of order κ^{N_τ}, but since we have $h_1 = \mathcal{O}(1)$ in finite density systems those can not serve as expansion parameters. It therefore makes sense to order the expansion in terms of spatial hoppings.

and backward, i.e. quark and anti-quark, propagation,

$$\begin{aligned}(Q_{\text{stat}})^{-1}_{x,y} &= (\mathbb{1} - T^{+}_{x,y} - T^{-}_{x,y})^{-1} \\ &= (\mathbb{1} - T^{+}_{x,y})^{-1} + (1 - T^{-}_{x,y})^{-1} - \mathbb{1} \\ &= (Q^{+}_{\text{stat}})^{-1} + (Q^{-}_{\text{stat}})^{-1} - \mathbb{1}. \end{aligned} \tag{4.24}$$

We will start with calculating the static quark propagator $(Q^{+}_{\text{stat}})^{-1}$. Since no spatial propagation is involved, we can fix $\vec{x} = \vec{y}$, so propagation will be from time τ_x to τ_y. In the case that $\tau_x = \tau_y$ we get

$$(Q^{+}_{\text{stat}})^{-1}_{\tau_x,\tau_x} = \mathbb{1} - h_1 \frac{\frac{1}{2}(\mathbb{1} + \gamma_4)W}{\mathbb{1} + h_1 W}. \tag{4.25}$$

The leading one comes from the possibility to move from τ_x to τ_x by making no movement at all. Alternatively, the quark can travel an arbitrary number of times around the temporal extent of the lattice, i.e. have infinitely many windings. These can be summed up as a geometric sum resulting in the second term.

Considering next the case that $\tau_x \neq \tau_y$ we have two separate contributions, coming from $\tau_x > \tau_y$ and $\tau_x < \tau_y$,

$$(Q^{+}_{\text{stat}})^{-1}_{\tau_x \neq \tau_y} = h_1^{\frac{\tau_y - \tau_x}{N_\tau}} \frac{\frac{1}{2}(\mathbb{1} + \gamma_4)W(\tau_x, \tau_y)}{\mathbb{1} + h_1 W}[\theta(\tau_y - \tau_x) - h_1 \theta(\tau_x - \tau_y)]. \tag{4.26}$$

We write $W(\tau_x, \tau_y)$ to denote a temporal Wilson line going from τ_x to τ_y in the positive time direction. Such a partial winding is proportional to the fractional static quark coupling constant $h_1^{\frac{\tau_y - \tau_x}{N_\tau}}$. Note how we can reach an earlier timeslice by crossing the antiperiodic boundaries, adding an additional minus sign. We get the complete positive propagator by combining the cases $\tau_x = \tau_y$ and $\tau_x \neq \tau_y$ [5],

$$\begin{aligned}(Q^{+}_{\text{stat}})^{-1}_{xy} &= \delta_{\tau_x,\tau_y}(\mathbb{1} - q\ h_1 W) + q\ h_1^{\frac{\tau_y - \tau_x}{N_\tau}} W(\tau_x, \tau_y)[\theta(\tau_y - \tau_x) - h_1 \theta(\tau_x - \tau_y)], \\ q &= \frac{\frac{1}{2}(\mathbb{1} + \gamma_4)}{\mathbb{1} + h_1 W}. \end{aligned} \tag{4.27}$$

The static anti-quark propagator is derived equivalently by making the replacements

$$\tau_x \leftrightarrow \tau_y, \quad W(\tau_x, \tau_y) \leftrightarrow W(\tau_x, \tau_y)^\dagger \quad \mu \leftrightarrow -\mu. \tag{4.28}$$

[5] We use the convention $\theta(0) = 0$.

Doing so we get

$$(Q^{-}_{\mathrm{stat}})^{-1}_{xy} = \delta_{\tau_x,\tau_y}(\mathbb{1} - \bar{q}\bar{h}_1 W^\dagger) + \bar{q}\bar{h}_1^{\frac{\tau_x-\tau_y}{N_\tau}} W^\dagger(\tau_x,\tau_y)[\theta(\tau_x-\tau_y) - \bar{h}_1\theta(\tau_y-\tau_x)],$$
$$\bar{q} = \frac{\frac{1}{2}(\mathbb{1}-\gamma_4)}{\mathbb{1}+\bar{h}_1 W^\dagger}. \tag{4.29}$$

$W^\dagger(\tau_x,\tau_y)$ now denotes a string of temporal links connecting the timeslices τ_x and τ_y in the negative time direction.

For the following calculations it will prove convenient to furthermore split up the static propagator according to

$$(Q_{\mathrm{stat}})^{-1}_{xy} = A^+_{xy} + \gamma_4 B^+_{xy} + A^-_{xy} - \gamma_4 B^-_{xy}. \tag{4.30}$$

The respective terms then read

$$\begin{aligned}
A^+_{xy} &= \frac{1}{2}\Big[\mathbb{1} - \frac{h_1 W}{\mathbb{1}+h_1 W}\Big]\delta_{xy} + \frac{1}{2}h^{\frac{\tau_y-\tau_x}{N_\tau}}\frac{W(\tau_x,\tau_y)}{\mathbb{1}+h_1 W}\Big[\theta(\tau_y-\tau_x) - h_1\theta(\tau_x-\tau_y)\Big]\delta_{\vec{x},\vec{y}},\\
B^+_{xy} &= -\frac{1}{2}\frac{h_1 W}{\mathbb{1}+h_1 W}\delta_{xy} + \frac{1}{2}h^{\frac{\tau_y-\tau_x}{N_\tau}}\frac{W(\tau_x,\tau_y)}{\mathbb{1}+h_1 W}\Big[\theta(\tau_y-\tau_x) - h_1\theta(\tau_x-\tau_y)\Big]\delta_{\vec{x},\vec{y}},\\
A^-_{xy} &= \frac{1}{2}\Big[\mathbb{1} - \frac{\bar{h}_1 W^\dagger}{\mathbb{1}+\bar{h}_1 W^\dagger}\Big]\delta_{xy} + \frac{1}{2}\bar{h}^{\frac{\tau_y-\tau_x}{N_\tau}}\frac{W^\dagger(\tau_x,\tau_y)}{\mathbb{1}+\bar{h}_1 W^\dagger}\Big[\theta(\tau_x-\tau_y) - \bar{h}_1\theta(\tau_y-\tau_x)\Big]\delta_{\vec{x},\vec{y}},\\
B^-_{xy} &= -\frac{1}{2}\frac{\bar{h}_1 W^\dagger}{\mathbb{1}+\bar{h}_1 W^\dagger}\delta_{xy} + \frac{1}{2}\bar{h}^{\frac{\tau_y-\tau_x}{N_\tau}}\frac{W^\dagger(\tau_x,\tau_y)}{\mathbb{1}+\bar{h}_1 W^\dagger}\Big[\theta(\tau_x-\tau_y) - \bar{h}_1\theta(\tau_y-\tau_x)\Big]\delta_{\vec{x},\vec{y}}.
\end{aligned} \tag{4.31}$$

This completes our derivation of the static quark propagator. We can proceed to calculate the leading order of the kinetic determinant. Inserting the definitions of P and M the leading order, eq. 4.23, reads

$$\begin{aligned}
\det Q_{\mathrm{kin}} &= \exp(\mathrm{Tr}PM + \mathcal{O}(\kappa^4))\\
&= \exp(\sum_{x,y,i}\mathrm{Tr}[(Q_{\mathrm{s}})^{-1}_{x,y}S^+_{y,y+i}(Q_{\mathrm{s}})^{-1}_{y+i,x+i}S^-_{x+i,x}] + \mathcal{O}(\kappa^4)).
\end{aligned} \tag{4.32}$$

This corresponds to propagation in the temporal direction, followed by a spatial hop to a neighbouring lattice site, then temporal propagation and finally a spatial hop back to the original site. Inserting the definition of the static quark propagator and the spatial hoppings, while using the abbreviation $A_{x,y} = A^+_{x,y} + A^-_{x,y}$ and $B_{x,y} = B^+_{x,y} - B^-_{x,y}$, we can write this as

$$\begin{aligned}
\det Q_{\mathrm{kin}} = \exp\Big(&-\kappa^2\sum_{x,y,i}\mathrm{Tr}[(A_{x,y}+\gamma_4 B_{x,y})(\mathbb{1}+\gamma_i)U_i(y)\\
&\times(A_{y+i,x+i}+\gamma_4 B_{y+i,x+i})(\mathbb{1}-\gamma_i)U_i^\dagger(x)] + \mathcal{O}(\kappa^4)\Big)
\end{aligned} \tag{4.33}$$

We now see the benefit of splitting up the static quark propagator as we did in eq. 4.30,

since after we evaluate the Dirac matrices the terms proportional to $A_{x,y}$ drop out. The kinetic quark determinant is then equal to

$$\exp\Big(- 8\kappa^2 \sum_{x,y,i} \mathrm{Tr}[(B^+_{x,y} - B^-_{x,y})U_i(y)(B^+_{y,x} - B^-_{y,x})U_i^\dagger(x+i)] + \mathcal{O}(\kappa^4)\Big). \tag{4.34}$$

Now we have to perform the integration over spatial links. Since this can not be done for links in the exponential we have to expand,

$$\int [dU_i] \exp(\mathrm{Tr} \sum_{x,y,i} P_{x,i} M_{y,i}) = 1 + \int [dU_i] \mathrm{Tr} \sum_{x,y,i} P_{x,i} M_{y,i} + \mathcal{O}(\kappa^4). \tag{4.35}$$

Furthermore, we need the following group integrals [99]

$$\begin{aligned} \int dU U_{ij} &= 0 \\ \int dU U^\dagger_{ij} &= 0 \\ \int dU U_{ij} U^\dagger_{kl} &= \frac{1}{N_c} \delta_{il} \delta_{jk} \end{aligned} \tag{4.36}$$

This means graphs involving single occupied spatial links vanish, implying that we have to set $x_4 = y_4$. Since $A_{x,y}$ and $B_{x,y}$ describe purely temporal propagation we already know that $\vec{x} = \vec{y}$, so we can set $x = y$. Performing the integration this leads to

$$\begin{aligned} &- \int [dU_i] \sum_{x,i} \mathrm{Tr}[(Q_\mathrm{s})^{-1}_{x,x} S^+_{x,x+i} (Q_\mathrm{s})^{-1}_{x+i,x+i} S^-_{x+i,x} (Q_\mathrm{s})^{-1}_{x,x}] = \\ &\quad -8 \frac{\kappa^2}{N_c} \sum_{x,i} \mathrm{Tr}[B^+_{x,x} + B^-_{x,x}] \mathrm{Tr}[B^+_{x+i,x+i} + B^-_{x+i,x+i}]. \end{aligned} \tag{4.37}$$

Now that the action does no longer depend on spatial links we can perform the sum over all temporal positions. This changes the sum to a sum over spatial positions, making the action three dimensional. $B_{x,x}$ does not depend on x_4, so we only have to introduce an additional factor of N_τ. Inserting the definition for $B_{x,x}$ we get the final expression for the kinetic determinant to leading order,

$$\begin{aligned} \int [dU_i] \det Q_\mathrm{kin} = 1 - 2 \frac{\kappa^2 N_\tau}{N_c} \sum_{\vec{x},i} &\Big(\mathrm{Tr} \frac{h_1 W_{\vec{x}}}{\mathbb{1} + h_1 W_{\vec{x}}} - \mathrm{Tr} \frac{\bar{h}_1 W^\dagger_{\vec{x}}}{\mathbb{1} + \bar{h}_1 W^\dagger_{\vec{x}}} \Big) \\ &\times \Big(\mathrm{Tr} \frac{h_1 W_{\vec{x}+i}}{\mathbb{1} + h_1 W_{\vec{x}+i}} - \mathrm{Tr} \frac{\bar{h}_1 W^\dagger_{\vec{x}+i}}{\mathbb{1} + \bar{h}_1 W^\dagger_{\vec{x}+i}} \Big) + \mathcal{O}(\kappa^4). \end{aligned} \tag{4.38}$$

The leading correction to the static quark limit is therefore a nearest neighbour interaction. This can take place between two quarks, two anti-quarks or between a quark and an anti-quark. Like in the static case there is no more dependence on temporal

coordinates. To characterize the nearest neighbour interaction strength we introduce the coupling

$$h_2(\kappa, N_\tau) = \frac{\kappa^2 N_\tau}{N_c}. \tag{4.39}$$

Like the static quark couplings this will receive gauge corrections once we introduce a finite β. Those corrections will be discussed in section 4.4.

Note that our degrees of freedom changed from Polyakov loops, as in the static case, to $\mathrm{Tr}\frac{h_1 W}{1+h_1 W}$, i.e. traces over all powers of temporal Wilson lines. This happened due to the resummation over all possible winding numbers. In appendix C we show that it is always possible to exactly rewrite the action in terms of Polyakov loops.

The action involving the sum over all winding numbers is far superior to the unresummed version which was given in [90]. The reason for that is that at the onset to the region of finite baryon density h_1 will be large. High winding numbers will therefore give a significant contribution. In the limit of high chemical potential μ we have $h_1 \to \infty$. The unresummed action, which is proportional to $h_1 \mathrm{Tr}\, W$, will therefore diverge. The resummed action in contrast becomes constant, leading to the expected behaviour of lattice saturation once the lattice is filled with quarks. The resummed version therefore gives the correct behaviour for all values of μ, while the truncated version is limited to small values of μ.

4.3.3 Kinetic Quark Determinant to Next to Leading Order

We will now proceed to calculate the fermion determinant to next to leading order, i.e. to order $\mathcal{O}(\kappa^4)$. For this we have to include the $n = 4$ case in eq. 4.22. An additional contribution arises from the expansion of the exponential in eq. 4.35.

Including $n = 4$ in eq. 4.22 results in

$$\exp(\mathrm{Tr}\sum_{n=1}^{\infty}[-\frac{1}{n}(P+M)^n]) = \\ \exp(-\sum_i \mathrm{Tr}P_iM_i - \sum_{ijkl}\mathrm{Tr}P_iP_jM_kM_l - \frac{1}{2}\sum_{ijkl}\mathrm{Tr}P_iM_jP_kM_l) + \mathcal{O}(\kappa^6). \tag{4.40}$$

As previously, only closed quark lines give a contributions, so we dropped terms that contain an unequal number of Ps and Ms. Furthermore we have to enforce restrictions on the spatial directions by introducing the delta functions $\delta_{i+j-k-l}$ for the $PPMM$ and $\delta_{i-j+k-l}$ for the $PMPM$ term. Evaluating those we get multiple distinct contributions

from both terms,

$$\begin{aligned}\sum_{ijkl} \mathrm{Tr} P_i P_j M_k M_l \ \delta_{i+j-k-l} &= \sum_{i\neq j} \mathrm{Tr} P_i P_j M_j M_i + \sum_{i,j} \mathrm{Tr} P_i P_j M_i M_j \\ \sum_{ijkl} \mathrm{Tr} P_i M_j P_k M_l \ \delta_{i-j+k-l} &= \sum_{i} \mathrm{Tr} P_i M_i P_i M_i + \sum_{i\neq j} \mathrm{Tr} P_i M_i M_j M_j \\ &\quad + \sum_{i\neq j} \mathrm{Tr} P_i M_j P_j M_i. \end{aligned} \tag{4.41}$$

As can be seen those terms describe lines and wedges of length $2a$. An exception is the term $P_i P_j M_i M_j$, that forms a square if $i \neq j$. The restrictions in the sums have to be introduced in order to avoid overcounting. The last $\mathcal{O}(\kappa^4)$ contributions comes from the expansion of eq. 4.35,

$$\begin{aligned}\exp(-\sum_{\vec{x},i} \mathrm{Tr} P_{x,i} M_{x,i}) &= 1 - \sum_{\vec{x},i} \mathrm{Tr} P_{x,i} M_{x,i} \\ &\quad + \sum_{x,i} \sum_{y,j} \mathrm{Tr} P_{x,i} M_{x,i} \mathrm{Tr} P_{y,j} M_{y,j} + O(\kappa^6). \end{aligned} \tag{4.42}$$

Since here we have two independent sums and two traces this term describes mostly disconnected diagrams and is quadratic in the lattice volume. In section 4.5 we will demonstrate how terms like this can be resummed.

We start with the first term in eq. 4.41. Inserting again the definitions for the hopping terms and remembering that spatial hops have to take place at the same timeslices we get

$$\begin{aligned}\sum_{i,j} \mathrm{Tr} P_i P_j M_j M_i &= \sum_{x,y,i,j} \mathrm{Tr}[(Q_s^{-1})_{xx} S^+_{x,x+i} (Q_s^{-1})_{x+i,y+i} S^+_{y+i,y+i+j} \\ &\quad (Q_s^{-1})_{y+i+j,y+i+j} S^-_{y+i+j,y+i} (Q_s^{-1})_{y+i,x+i} S^-_{x+i,x}] \\ &= \kappa^4 \sum_{i,j} \mathrm{Tr}[(A-\gamma_4 B)(\mathbb{1}+\gamma_i) U_i(x) (A+\gamma_4 B)(\mathbb{1}+\gamma_j) U_j(y+i) \\ &\quad (A+\gamma_4 B)(\mathbb{1}-\gamma_j) U_j^\dagger(y+i) (A+\gamma_4 B)(\mathbb{1}-\gamma_i) U_i^\dagger(x)] \end{aligned} \tag{4.43}$$

As in the previous section several terms drop out when we evaluate the Dirac matrices,

$$\begin{aligned}&\sum_{i,j} \mathrm{Tr} P_i P_j M_j M_i = \\ &32\kappa^4 \sum_{x,y,i,j} B_{x,x} U_i(x) A_{x+i,y+i} U_j(y+i) B_{y+i+j,y+i+j} U_j^\dagger(y+i) A_{y+i,x+i} U_i^\dagger(x). \end{aligned} \tag{4.44}$$

We are again only dealing with doubly occupied spatial links. We therefore use eq. 4.36 to perform the integration,

$$\int [dU_i] \sum_{i,j} \mathrm{Tr} P_i P_j M_j M_i = 32 \frac{\kappa^4}{N_c^2} \sum_{x,y,i,j} \mathrm{Tr} B_{x,x} \mathrm{Tr} A_{x+i,y+i} A_{y+i,x+i} \mathrm{Tr} B_{y+i+j,y+i+j}. \tag{4.45}$$

Since $A_{x,y}$ describes temporal propagation we can set $\vec{x} = \vec{y}$. After that we perform the sums over temporal positions and insert the definitions for A and B,

$$\begin{aligned}
-\int [dU_i] \sum_{i,j} \mathrm{Tr} P_i P_j M_j M_i = 2 \frac{\kappa^4 N_\tau (N_\tau - 1)}{N_c^2} \sum_{\vec{x},i,j} \mathrm{Tr}\Big(\frac{h_1 W_{\vec{x}}}{\mathbb{1} + h_1 W_{\vec{x}}} - \frac{\bar{h}_1 W^\dagger_{\vec{x}}}{\mathbb{1} + \bar{h}_1 W^\dagger_{\vec{x}}} \Big) \\
\mathrm{Tr}\Big(\frac{h_1 W_{\vec{x}+i}}{(\mathbb{1} + h_1 W_{\vec{x}+i})^2} - \frac{\bar{h}_1 W^\dagger_{\vec{x}+i}}{(\mathbb{1} + \bar{h}_1 W^\dagger_{\vec{x}+i})^2} - 2 \frac{\frac{\mathbb{1}}{N_\tau - 1} \sum_{t=1}^{N_\tau - 1} (2\kappa)^{2t}}{(\mathbb{1} + h_1 W_{\vec{x}+i})(\mathbb{1} + \bar{h}_1 W^\dagger_{\vec{x}+i})} \Big) \\
\mathrm{Tr}\Big(\frac{h_1 W_{\vec{x}+i+j}}{\mathbb{1} + h_1 W_{\vec{x}+i+j}} - \frac{\bar{h}_1 W^\dagger_{\vec{x}+i+j}}{\mathbb{1} + \bar{h}_1 W^\dagger_{\vec{x}+i+j}} \Big) \\
-2 \frac{\kappa^4 N_\tau}{N_c^2} \sum_{\vec{x},i,j} \mathrm{Tr}\Big(\frac{h_1 W_{\vec{x}}}{\mathbb{1} + h_1 W_{\vec{x}}} - \frac{\bar{h}_1 W^\dagger_{\vec{x}}}{\mathbb{1} + \bar{h}_1 W^\dagger_{\vec{x}}} \Big) \mathrm{Tr}\Big(\mathbb{1} - \frac{h_1 W_{\vec{x}+i}}{(\mathbb{1} + h_1 W_{\vec{x}+i})} + \mathbb{1} - \frac{\bar{h}_1 W^\dagger_{\vec{x}+i}}{\mathbb{1} + \bar{h}_1 W^\dagger_{\vec{x}+i}} \Big)^2 \\
\mathrm{Tr}\Big(\frac{h_1 W_{\vec{x}+i+j}}{\mathbb{1} + h_1 W_{\vec{x}+i+j}} - \frac{\bar{h}_1 W^\dagger_{\vec{x}+i+j}}{\mathbb{1} + \bar{h}_1 W^\dagger_{\vec{x}+i+j}} \Big).
\end{aligned} \tag{4.46}$$

There are two distinct contributions. The first one is proportional to $N_\tau(N_\tau - 1)$. It stems from the sum over the terms where $x_4 \neq y_4$. The second one is proportional to N_τ, accounting for the case where $x_4 = y_4$. They differ in the value of $\mathrm{Tr} A_{x+i,y+i} A_{y+i,x+i}$. In the case of $x_4 \neq y_4$ the two propagators, $A_{x+i,y+i}$ and $A_{y+i,x+i}$, are both fractional Wilson lines, but together they form one closed loop around the lattice. Both partial propagations can be followed by an arbitrary number of complete loops, accounting for the square in the denominator. The term containing the sum over 2κ describes the case where forward and backward propagation mixes [6]. The case where $x_4 = y_4$ is somewhat simpler. Both propagators describe full windings around the temporal dimension.

Due to the length of the expressions, the remainder of the κ^4 action is shown in appendix A. This completes our discussion of the derivation of the hopping parameter expansion in the strong coupling limit. We will now proceed with the derivation of gauge corrections.

[6] Since this is intermitted by spatial hoppings, which can not be seen any more since they have been integrated out, this does not violate the restriction concerning backtracking.

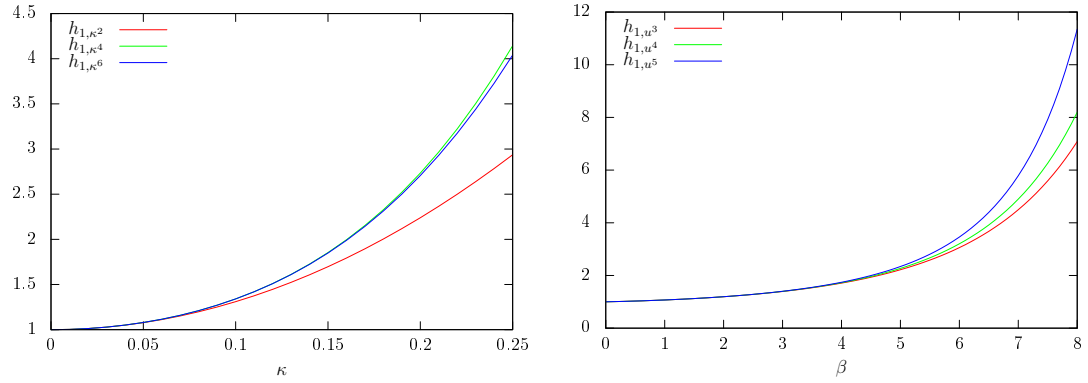

FIGURE 4.1: Left: Static quark coupling h_1 truncated at orders κ^2, κ^4 and κ^6 at $\beta = 6, N_\tau = 10$. Right: h_1 truncated at order u^3, u^4 and u^5 at $\kappa = 0.25, N_\tau = 10$.

4.4 Gauge Corrections

The pure gauge contribution was already discussed in section 4.2, but moving away from the strong coupling limit also introduces mixing terms. We use this term to describe diagrams that contain graphs coming from the strong coupling as well as graphs coming from the hopping parameter expansion. Such diagrams contain gauge plaquettes as well as quark lines. Many of those new contributions reduce to graphs already present in the strong coupling limit after the spatial link integration has been performed. We can therefore absorb them into the respective coupling constants, so we will get $h_1(\kappa) = h_1(\beta, \kappa)$, $h_2(\kappa) = h_2(\beta, \kappa)$, and so on. These contributions are presented in section 4.4.1, while the new interactions are shown in section 4.4.2. Since there is an infinite number of possible gauge corrections to all of our couplings we additionally have to check their convergence by comparing different truncations in $u(\beta)$. Finally, there are fermionic corrections that get absorbed into the gauge couplings, $\lambda_1(\beta) = \lambda_1(\beta, \kappa)$. We will discuss those in 4.4.3.

4.4.1 Corrections to Fermion Couplings

The gauge corrections for h_1 are [90, 100] [7]

$$h_1(u, \kappa, N_\tau \geq 3) = \exp\Big[N_\tau(\mu + \ln(2\kappa))\Big] \exp\Big[6N_\tau\kappa^2 u\Big(\frac{1-u^{N_\tau-1}}{1-u} + 4u^4 - 12\kappa^2 + 9k^2u + 4\kappa^2u^2 - 4\kappa^4\Big)\Big] \quad (4.47)$$

The anti-quark coupling $\bar{h}_1$ receives the same corrections. In fig. 4.1 we compare different truncations of h_1 to test the convergence of the expansion in κ and $u(\beta)$. As can be seen, h_1 (and therefore $\bar{h}_1$) is convergent up to large values of κ and values of $\beta \approx 6$.

[7] Two prefactors given in [90] are wrong, we therefore replace them with the correct one from [100].

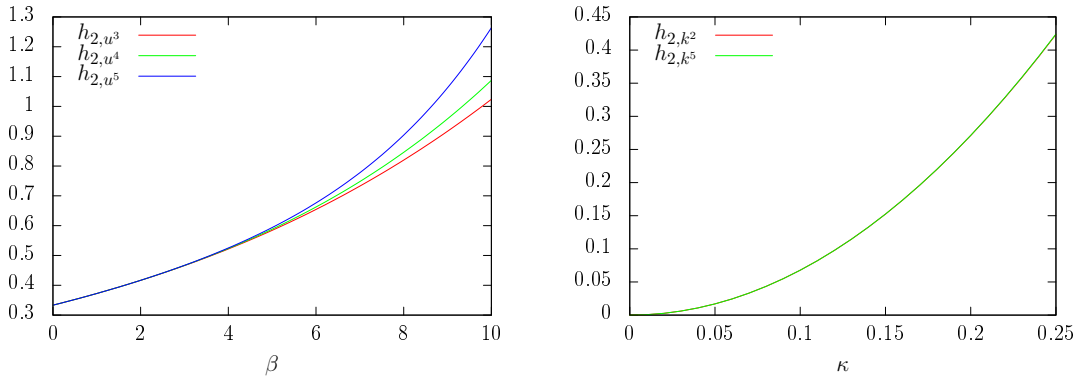

FIGURE 4.2: Left: Convergence of the nearest neighbour coupling h_2, truncated at order u^4 and u^5 and plotted vs. β with $N_\tau = 10, \kappa = 0.1$. Right: h_2 truncated at order κ^2 and κ^5, plotted vs κ with $N_\tau = 10$ and $\beta = 6$. Both lines lie on top of each other.

We already gave the leading gauge corrections for the nearest neighbour coupling h_2 in [91], the next corrections are

$$h_2(\kappa, N_\tau, u) = \frac{\kappa^2 N_\tau}{N_c}\Big(1 + 2\frac{u - u^{N_\tau}}{1-u} + 8u^5 + 16\kappa^3 u^4\Big). \tag{4.48}$$

The leading correction comes from graphs where the two spatial quark hoppings happen at separate locations. Since the integration rule eq. 4.36 enforces links to be at least doubly occupied we have to fill the area between them with gauge plaquettes. This can be done with up to $N_\tau - 1$ plaquettes and is summed up. The factor of two accounts for the possible orientations the plaquettes can take. The next correction that is not already included in this sum is of order u^5 and comes from attaching a cube out of five plaquettes onto quark hoppings separated by distance a. This can be done in four different spatial directions and in two different orientations. The final contribution comes from graphs where one of the plaquettes in the cube is replaced by three additional quark hoppings.

Fig. 4.2 shows the value of h_2 truncated to different orders in u and plotted against β. As can be seen including the corrections up to order u^5 should be sufficient to have good convergence up to values of $\beta \approx 6$. The leading κ correction is negligible up to high values of κ.

We now proceed to consider the couplings for the κ^4 graphs. We start with the two point interactions, eq. A.2 and eq. A.3. We begin with the terms that only contain double occupied spatial links, i.e. the parts of eq. A.2 and eq. A.3 that are proportional to $N_\tau(N_\tau - 1)$. We are going to call the coupling constant for those terms h_{3_1}. Calculating corrections up to $\mathcal{O}(u^5)$ and $\mathcal{O}(\kappa^3 u^4)$ we get

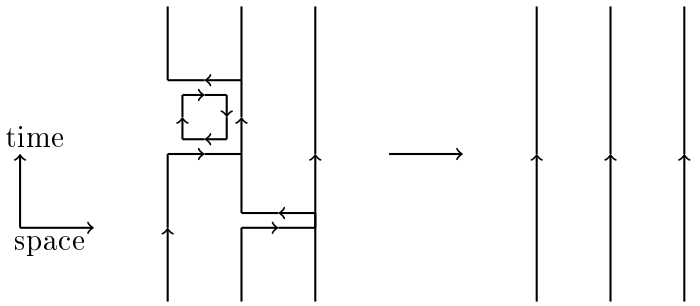

FIGURE 4.3: The leading gauge correction to h_{3_3}, created by inserting a single gauge plaquette, before and after the spatial link integration. To the next order one can attach another plaquette to the first one, or start inserting plaquettes to the other spatial quark links.

$$
\begin{aligned}
h_{3_1}(N_\tau = 2) &= \frac{N_\tau(N_\tau-1)\kappa^4}{N_c^2}, \\
h_{3_1}(N_\tau = 4) &= \frac{N_\tau(N_\tau-1)\kappa^4}{N_c^2}\Big[1+\frac{8}{3}\Big(u+u^2+4u^5+8\kappa^3u^4\Big)\Big], \\
h_{3_1}(N_\tau = 6) &= \frac{N_\tau(N_\tau-1)\kappa^4}{N_c^2}\Big[1+\frac{2}{5}\Big(8u+12u^2+12u^3+8u^4+32u^5+64\kappa^3u^4\Big)\Big], \\
h_{3_1}(N_\tau = 8) &= \frac{N_\tau(N_\tau-1)\kappa^4}{N_c^2}\Big[1+\frac{8}{7}\Big(3u+5u^2+6u^3+6u^4+17u^5+24\kappa^3u^4\Big)\Big], \\
h_{3_1}(N_\tau > 8) &= \frac{N_\tau(N_\tau-1)\kappa^4}{N_c^2}\Big[1+\frac{4u(2-N_\tau+N_\tau u)}{(N_\tau-1)(u-1)^3}+\frac{20(N_\tau-6)}{N_\tau-1}u^5 \\
&\qquad + \frac{40(N_\tau-6)}{N_\tau-1}\kappa^3u^4\Big].
\end{aligned} \tag{4.49}
$$

As in the case of the h_2 corrections the leading orders come from adding plaquettes to the area enclosed by the two Polyakov loops. The $\mathcal{O}(u^5)$ correction again contains contributions from adding a cube of plaquettes, and the κ dependent correction from replacing two plaquettes of the cube with quark hoppings.

In the case of two point interactions with all four spatial links sharing one position, i.e. the contributions proportional to $\kappa^4 N_\tau$ in eq. A.2 and eq. A.3, the gauge corrected coupling constant is

$$
h_{3_2}(N_\tau \geq 2) = \frac{\kappa^4 N_\tau}{N_c^2}\Big[1+4\frac{u-u^{N_\tau}}{1-u}+16u^5+32\kappa^3u^4\Big]. \tag{4.50}
$$

These corrections are derived analogously to the h_2 case, but with an additional factor of two due to the possibility to swap spatial quark lines.

The remaining terms, eq. A.4 , eq. A.5 and A.6 are three point interactions. Their coupling constant is

$$
h_{3_3}(N_\tau \geq 2) = \frac{\kappa^4 N_\tau^2}{N_c^2}\Big[1+4\frac{(1-u^{N_\tau})(u-u^{N_\tau})}{(1-u)^2}+16u^5+32\kappa^3u^4\Big]. \tag{4.51}
$$

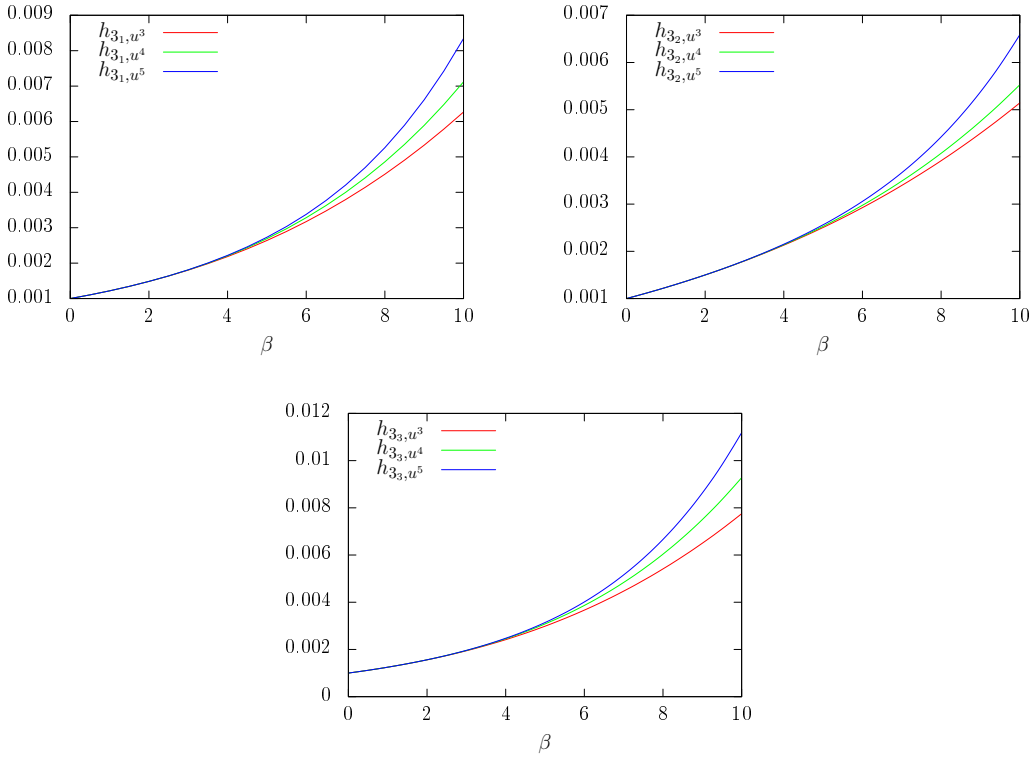

FIGURE 4.4: Coupling constants h_{3_1}, h_{3_2} and h_{3_3} truncated at order u^3, u^4 and u^5, plotted vs. β with $N_\tau = 10, \kappa = 0.1$.

Again we can sum up contributions coming from inserting plaquettes between the Polyakov loops, but since we now have three loops we have a double sum. The other corrections are derived as in the previous cases.

In fig. 4.4 we show the coupling constant h_{3_1}, h_{3_2} and h_{3_3} truncated at different orders in $u(\beta)$. As can be seen the gauge corrections converge well up to values of $\beta \approx 6$. Since the κ dependent corrections are similarly small as for the h_2 coupling we do not show the respective plots.

4.4.2 New Interactions at finite β

An entirely new contributions comes from the term $\mathrm{Tr} P_i P_j M_i M_j$ in eq. 4.41, which we neglected because its contributions vanishes for $\beta = 0$. This is because it forms a square and therefore has only singly occupied spatial links. But considering finite values of β, it becomes non-vanishing when we insert a gauge plaquette inside of the square. This requires all spatial hoppings to happen in the same timeslice, the contribution is

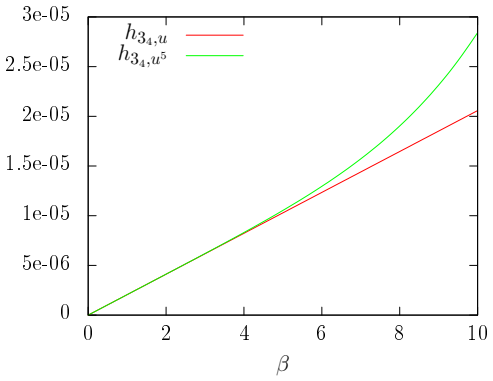

FIGURE 4.5: Coupling constant h_{3_4} truncated to order u and u^5, $\kappa = 0.1, N_\tau = 10$.

therefore proportional to $\kappa^4 u N_\tau$. Inserting the definitions for P and M we get

$$
\begin{aligned}
-\int [dU_k] \sum_{i\neq j} \mathrm{Tr} P_i P_j M_i M_j = N_c \kappa^4 u \sum_{x,i\neq j} \mathrm{Tr}\Big[& U_j^\dagger(x+i) U_i^\dagger(x) U_j(x) U_i(x+j)\Big] \\
\mathrm{Tr}\Big[& (A_{x,x} + \gamma_4 B_{x,x}) U_i(x) (\mathbb{1} + \gamma_i)(A_{x+i,x+i} + \gamma_4 B_{x+i,x+i}) U_j(x+i)(\mathbb{1}+\gamma_j) \\
& (A_{x+i+j,x+i+j} + \gamma_4 B_{x+i+j,x+i+j}) U_i^\dagger(x+j)(\mathbb{1}-\gamma_i)(A_{x+j,x+j} + \gamma_4 B_{x+j,x+j}) U_j^\dagger(x)(\mathbb{1}-\gamma_j)\Big].
\end{aligned}
\tag{4.52}
$$

After evaluating the gamma matrices and performing the spatial link integration this gives

$$
\begin{aligned}
-\int [dU_k] \sum_{i\neq j} \mathrm{Tr} P_i P_j M_i M_j = & \\
8\frac{\kappa^4 u}{N_c^3} \sum_{x,i\neq j} \Big[& \mathrm{Tr}A_{x,x}\mathrm{Tr}A_{x+i,x+i}\mathrm{Tr}A_{x+i+j,x+i+j}\mathrm{Tr}A_{x+j,x+j} \\
& -\mathrm{Tr}B_{x,x}\mathrm{Tr}B_{x+i,x+i}\mathrm{Tr}A_{x+i+j,x+i+j}\mathrm{Tr}A_{x+j,x+j} \\
& -\mathrm{Tr}B_{x,x}\mathrm{Tr}A_{x+i,x+i}\mathrm{Tr}B_{x+i+j,x+i+j}\mathrm{Tr}A_{x+j,x+j} \\
& -\mathrm{Tr}A_{x,x}\mathrm{Tr}B_{x+i,x+i}\mathrm{Tr}B_{x+i+j,x+i+j}\mathrm{Tr}A_{x+j,x+j} \\
& -\mathrm{Tr}B_{x,x}\mathrm{Tr}A_{x+i,x+i}\mathrm{Tr}A_{x+i+j,x+i+j}\mathrm{Tr}B_{x+j,x+j} \\
& -\mathrm{Tr}A_{x,x}\mathrm{Tr}B_{x+i,x+i}\mathrm{Tr}A_{x+i+j,x+i+j}\mathrm{Tr}B_{x+j,x+j} \\
& -\mathrm{Tr}A_{x,x}\mathrm{Tr}A_{x+i,x+i}\mathrm{Tr}B_{x+i+j,x+i+j}\mathrm{Tr}B_{x+j,x+j} \\
& +\mathrm{Tr}B_{x,x}\mathrm{Tr}B_{x+i,x+i}\mathrm{Tr}B_{x+i+j,x+i+j}\mathrm{Tr}B_{x+j,x+j}\Big].
\end{aligned}
\tag{4.53}
$$

Like in the case of the other $\mathcal{O}(\kappa^4)$ contributions the final result after performing the temporal sum has been moved to appendix A. The coupling constant for this term,

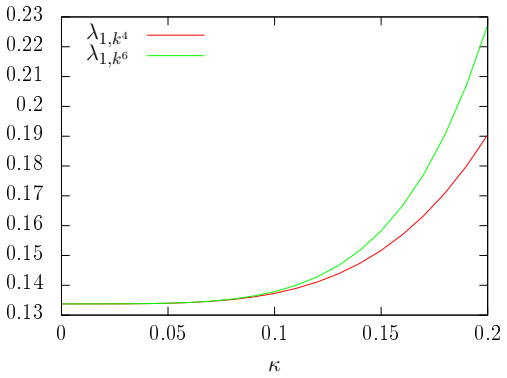

FIGURE 4.6: Gauge constant λ_1 truncated to orders κ^4 and κ^6. Parameters are $\beta = 6, N_\tau = 4, N_f = 3$.

including leading gauge corrections, is

$$h_{3_4}(N_\tau \geq 2) = \frac{1}{2}\frac{\kappa^4 u N_\tau}{N_c^3}\Big[1 + 4u^4 + 16u^3\kappa^3\Big]. \tag{4.54}$$

The convergence of the gauge corrections for h_{3_4} are shown in fig. 4.5. Like for the other coupling constants, κ dependent corrections seem to be negligible, while the convergence in β is good up to $\beta \approx 6$.

4.4.3 Fermion Corrections to the Gauge Action

We now want to discuss fermionic contributions to λ, i.e. $\lambda(\beta, N_\tau) = \lambda(\beta, N_\tau, \kappa)$. The leading order correction was already given in [90]. It comes from the possibility to replace any gauge plaquette by four quark hoppings. Since this can be done for every plaquette we can absorb this contribution into an overall shift in β, by making the correction

$$\beta \to \beta + 48 N_f \kappa^4. \tag{4.55}$$

The next contribution comes from replacing two adjacent plaquettes in the graphs leading to the leading interaction 4.7 with six quark hoppings, giving [8]

$$\lambda(\beta, \kappa) = u^{N_\tau} + \frac{16 N_f N_\tau \kappa^6}{9u^2}. \tag{4.56}$$

Since this only applies to adjacent plaquettes this contribution can not be absorbed into an overall shift in β.

In fig. 4.6 we again check the convergence of λ_1 by truncating it at different orders in κ. Fermionic corrections to λ_1 seem to become sizable at $\kappa > 0.1$.

[8] For higher corrections of λ_1 in u and the respective truncation error see [89].

4.5 Resummation of the effective action

The 4 dimensional action we started with was written in the exponential. We had to expand it in order to perform the spatial link integrals. Neglecting anti-quark contributions for brevity the κ^2 theory we derived so far reads

$$Z = \int [dU_4]\ \mathrm{Q}_{\mathrm{stat}} \Big(1 - h_2 \sum_{\vec{x},i} \mathrm{Tr} \frac{h_1 W_{\vec{x}}}{\mathbb{1} + h_1 W_{\vec{x}}} \mathrm{Tr} \frac{h_1 W_{\vec{x}+i}}{\mathbb{1} + h_1 W_{\vec{x}+i}} \Big). \tag{4.57}$$

The κ^2 truncation will only be a good approximation if the $\mathcal{O}(\kappa^2)$ contributions are small, i.e. if the sum in eq. 4.57 times h_2 is much smaller than one. Since the sum goes over all spatial positions convergence depends on the lattice size, meaning that the thermodynamical limit only exists in the limit of $\kappa \to 0$.

To get a finite result for $\kappa \neq 0$ we need to resum the effective action, bringing it back into an exponentiated form. Taking the leading $\mathcal{O}(\kappa^2)$ term and searching for suitable κ^4 terms we see that this is indeed possible. The $\mathcal{O}(\kappa^4)$ contribution from eq. 4.42 can be used as the next order in the resummation. Taking both contributions we can write

$$\begin{aligned} & 1 - 2\frac{\kappa^2 N_\tau}{N_c} \sum_{\vec{x},i} \mathrm{Tr} \frac{h_1 W_{\vec{x}}}{\mathbb{1} + h_1 W_{\vec{x}}} \mathrm{Tr} \frac{h_1 W_{\vec{x}+i}}{\mathbb{1} + h_1 W_{\vec{x}+i}} \\ & + 2\frac{\kappa^4 N_\tau (N_\tau - 1)}{N_c^2} \sum_{\vec{x},\vec{y},i,j} \mathrm{Tr} \frac{h_1 W_{\vec{x}}}{\mathbb{1} + h_1 W_{\vec{x}}} \mathrm{Tr} \frac{h_1 W_{\vec{x}+i}}{\mathbb{1} + h_1 W_{\vec{x}+i}} \mathrm{Tr} \frac{h_1 W_{\vec{y}}}{\mathbb{1} + h_1 W_{\vec{y}}} \mathrm{Tr} \frac{h_1 W_{\vec{y}+j}}{\mathbb{1} + h_1 W_{\vec{y}+j}} + O(\kappa^6) \\ & = \exp\Big[-2\frac{\kappa^2 N_\tau}{N_c} \sum_{\vec{x},i} \mathrm{Tr} \frac{h_1 W_{\vec{x}}}{\mathbb{1} + h_1 W_{\vec{x}}} \mathrm{Tr} \frac{h_1 W_{\vec{x}+i}}{\mathbb{1} + h_1 W_{\vec{x}+i}} \Big] + \mathcal{O}\Big(\frac{\kappa^4 N_\tau}{N_c^2} \Big). \end{aligned} \tag{4.58}$$

This resummation improves the convergence by including an infinite number of graphs. Inspection of higher order terms indicates that this should be valid to all orders. Since the term we found was of order $N_\tau(N_\tau - 1)$ instead of order N_τ^2, the resummation requires the introduction of counterterms that are of subleading order in N_τ in order to avoid overcounting.

This completes our derivation of the effective theory. We will end the chapter by demonstrating how to introduce multiple flavors in section 4.6, and discussing the limit of low temperatures and high chemical potential in section 4.7.

4.6 Multiple Flavors

So far we only considered the $N_f = 1$ case. Introducing another flavor means adding a second quark determinant, cf. eq. 3.19, so for $N_f = 2$ we have

$$Z = \int [dU_4] \det Q_u \det Q_d\ e^{-S_g}. \tag{4.59}$$

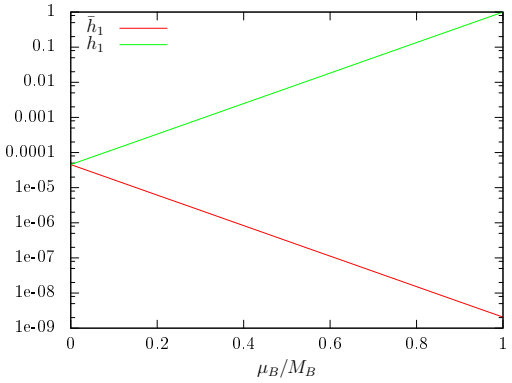

FIGURE 4.7: Comparison of the quark and anti-quark couplings h_1 and $\bar{h}_1$ plotted against the baryon chemical potential normalized with the baryon mass. At high chemical potential the anti-quark couplings is suppressed exponentially.

Each new flavor also introduces a new hopping parameters, so we now have κ_u and κ_d. The static strong coupling approximation for two flavors is therefore

$$Z = \int [dU_4] \prod_{\vec{x}} (1 + h_{1,u} L_{\vec{x}} + h_{1,u}^2 L_{\vec{x}}^* + h_{1,u}^3)^2 (1 + h_{1,d} L_{\vec{x}} + h_{1,d}^2 L_{\vec{x}}^* + h_{1,d}^3)^2, \tag{4.60}$$

with $h_{1,u}$ and $h_{1,d}$ being the static coupling constants for the respective quark flavors. The kinetic quark determinant, eq. 4.22, becomes

$$\begin{aligned} &\det[1 - P_u - M_u] \det[1 - P_d - M_d] = \\ &\exp\Big(\mathrm{Tr} \sum_{n=1}^{\infty} [-\frac{1}{n}(P_u + M_u)^n]) + \mathrm{Tr} \sum_{n=1}^{\infty} [-\frac{1}{n}(P_d + M_d)^n]\Big). \end{aligned} \tag{4.61}$$

A great simplification arises when we consider degenerate quarks, $\kappa_u = \kappa_d$. In the case of N_f degenerate quarks the expansion of the kinetic quark determinant simplifies to

$$Q_{\mathrm{kin}}^{N_f} = \exp(N_f \mathrm{Tr} \sum_{n=1}^{\infty} [-\frac{1}{n}(P + M)^n]). \tag{4.62}$$

In this case all expressions we derived so far stay the same, only the appropriate factors of N_f have to be introduced. We will use the approximation of multiple degenerate flavors in the chapters 5 and 6 to investigate QCD with $N_f = 2, 3$ heavy quarks.

4.7 Cold Dense Limit

The action derived so far can be simplified enormously when going to the cold dense limit. The limit of low temperatures $T = \frac{1}{aN_\tau}$ is reached by taking $N_\tau \to \infty$. In this limit only terms that are of leading order in N_τ will be relevant. This means that terms

in appendix A that are proportional to $\kappa^4 N_\tau$ are of subleading order compared to terms proportional to $\kappa^4 N_\tau^2$ and therefore can be neglected.

The dense limit is reached when the chemical potential μ_B becomes comparable to the baryon mass m_B, so that $h_1 = \mathcal{O}(1)$. Fig. 4.7 shows that in this limit the anti-quark coupling $\bar{h}_1$ goes to zero exponentially. This means that when investigating systems with large density, contributions proportional to $\bar{h}_1$ can be safely neglected. Terms containing both quark and anti-quark propagators, i.e. mesonic terms, are not exponentially suppressed in this limit. But since $h_1 \bar{h}_1 = (2\kappa)^{N_\tau}$, those become suppressed in the limit of large N_τ.

An additional simplification arises since the pure gauge couplings λ_1, λ_2 and λ_a go to zero in the limit $N_\tau \to \infty$. This can be seen from the fact that the lowest order contribution of all gauge coupling is at least $\mathcal{O}(u^{N_\tau})$. Since we have $u < 1$ for all β this will vanish if we take $N_\tau \to \infty$ while keeping β fixed. Gauge corrections in the low temperature limit can therefore be completely absorbed into the fermionic coupling constants.

We therefore can approximate the complete $\mathcal{O}(\kappa^4)$ action, including gauge contributions, as

$$
\begin{aligned}
S_{\text{eff}} = &- \sum_{\vec{x}} \ln[1 + h_1 \mathrm{Tr} W_{\vec{x}} + h_1^2 \mathrm{Tr} W_{\vec{x}}^\dagger + h_1^3] \\
&+ 2h_2 \sum_{\vec{x},i} \mathrm{Tr} \frac{h_1 W_{\vec{x}}}{\mathbb{1} + h_1 W_{\vec{x}}} \mathrm{Tr} \frac{h_1 W_{\vec{x}+i}}{\mathbb{1} + h_1 W_{\vec{x}+i}} \\
&- 2h_2^2 \sum_{\vec{x},i} \Big(\mathrm{Tr} \frac{h_1 W_{\vec{x}}}{\mathbb{1} + h_1 W_{\vec{x}}} \Big)^2 \Big(\mathrm{Tr} \frac{h_1 W_{\vec{x}+i}}{\mathbb{1} + h_1 W_{\vec{x}+i}} \Big)^2 \\
&- 2h_2^2 \sum_{\vec{x},i} \mathrm{Tr} \frac{h_1 W_{\vec{x}}}{(\mathbb{1} + h_1 W_{\vec{x}})^2} \mathrm{Tr} \frac{h_1 W_{\vec{x}+i}}{(\mathbb{1} + h_1 W_{\vec{x}+i})^2} \\
&- h_{3,3} \sum_{\vec{x},i,j} \mathrm{Tr} \frac{h_1 W_{\vec{x}}}{\mathbb{1} + h_1 W_{\vec{x}}} \mathrm{Tr} \frac{h_1 W_{\vec{x}+i}}{(\mathbb{1} + h_1 W_{\vec{x}+i})^2} \mathrm{Tr} \frac{h_1 W_{\vec{x}+i+j}}{\mathbb{1} + h_1 W_{\vec{x}+i+j}} \\
&- 2h_{3,3} \sum_{\vec{x},i,j} \mathrm{Tr} \frac{h_1 W_{\vec{x}}}{\mathbb{1} + h_1 W_{\vec{x}}} \mathrm{Tr} \frac{h_1 W_{\vec{x}+i}}{(\mathbb{1} + h_1 W_{\vec{x}+i})^2} \mathrm{Tr} \frac{h_1 W_{\vec{x}+i-j}}{\mathbb{1} + h_1 W_{\vec{x}+i-j}} \\
&- h_{3,3} \sum_{\vec{x},i,j} \mathrm{Tr} \frac{h_1 W_{\vec{x}}}{\mathbb{1} + h_1 W_{\vec{x}}} \mathrm{Tr} \frac{h_1 W_{\vec{x}-i}}{(\mathbb{1} + h_1 W_{\vec{x}-i})^2} \mathrm{Tr} \frac{h_1 W_{\vec{x}+i+j}}{\mathbb{1} + h_1 W_{\vec{x}+i+j}}.
\end{aligned}
\tag{4.63}
$$

This action is significantly simplified compared to the full expression, it is therefore preferable to use it wherever possible. We will investigate in the next chapter how fast this approximation converges to the complete $\mathcal{O}(\kappa^4)$ action.

Chapter 5

Numerical Results

In this chapter we will present the numerical results obtained from the effective theory which we derived in chapter 4. Like full lattice QCD (LQCD) our theory still suffers from the sign problem, described in section 3.4.2, when we use it to simulate finite density systems. We will therefore have to rely on the methods of Monte-Carlo with reweighting and stochastic quantization, which we outlined in section 3.5.2 and 3.5.4 respectively.

We begin in section 5.1 with demonstrating how the integration measure of the partition function can be changed from temporal gauge links to Polyakov loops. This leads to a reduced number of degrees of freedom and therefore to a further reduction of numerical costs. In section 5.2 we then discuss the observables we are interested in and how they are calculated. In Section 5.3.1 we compare data from Monte-Carlo and stochastic quantization simulations, in order to confirm the validity of the latter. Section 5.5 is concerned with the size of the truncation effects in κ. Those determine how far we can raise κ, i.e. lower the quark mass, until the neglect of higher orders is no longer a valid approximation. Together with the truncating effects on the coupling constants, discussed in section 4.4, this determines the parameter region where our theory converges to full LQCD. After those considerations we present our main results for two different regions of the QCD phase diagram:

Section 5.6 presents the results for the region of low temperatures and high density, which we discussed in section 2.5.2, including continuum extrapolated data for various thermodynamical observables. Furthermore, indications for a first order liquid-gas transition to cold nuclear matter are shown.

Section 5.7 is concerned with the high temperature phase, which we discussed in section 2.5. This region extents up to the deconfinement transition, where the effective theory breaks down. Here we show results for the chiral condensate and the nature of the Roberge-Weiss transition, see section 2.3.3, and compare our results to recent LQCD results [19].

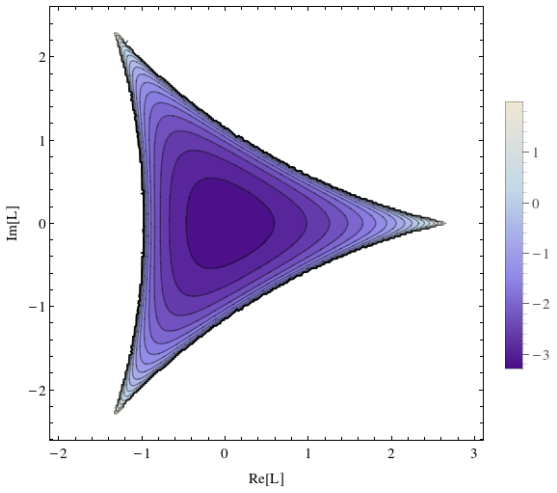

FIGURE 5.1: The Polyakov Loop potential eq. 5.2, induced by the change of the integration measure.

5.1 Integration Measure

When solving our theory in a simulation we have to chose an appropriate integration measure. The effective action we derived in chapter 4 depends on traces over fractions containing temporal Wilson lines. As described in appendix C we can always reformulate this in terms of Polyakov loops. This is true for all higher orders as well. It is therefore preferable to change the integration measure from temporal links to Polyakov loops [60, 89]. This introduces a Jacobian that takes the form of an effective potential,

$$Z = \int [dU_4] e^{-S_{\text{eff}}} = \int [dL] e^{-S_{\text{eff}}} e^{V}. \tag{5.1}$$

For $SU(3)$ this potential is

$$V = \sum_{\vec{x}} V_{\vec{x}} = \frac{1}{2} \sum_{\vec{x}} \ln(27 - 18|L_{\vec{x}}|^2 + 8\text{Re}L_{\vec{x}}^3 - |L_{\vec{x}}|^4). \tag{5.2}$$

The potential restricts the Polyakov loops to the region shown in fig 5.1. Following [101] we rotate the temporal gauge links to their diagonal form and write the Polyakov loops as

$$L_{\vec{x}}(\theta, \phi) = e^{i\theta} + e^{i\phi} + e^{-i(\theta+\phi)}, \quad \theta, \phi \in [-\pi, \pi). \tag{5.3}$$

Changing the integration variables to θ and ϕ introduces another Jacobian identical to the one in eq. 5.1,

$$\int [dU_4] = \int [dL] e^{V} = \int [d\theta][d\phi] e^{2V}. \tag{5.4}$$

We can therefore formulate our theory using only two complex degrees of freedom per spatial lattice site, as compared to $27N_\tau$ in the original theory.

5.2 Observables

The simplest observable in our effective theory is the Polyakov loop expectation value $\langle L \rangle$. Its physical relevance is twofold: As explained in section 2.3.1 we can use the Polyakov loop as an approximate order parameter for deconfinement, with $\langle L \rangle \approx 0$ in the confined and $\langle L \rangle \neq 0$ in the deconfined phase. Secondly, as shown in section 2.3.3, its phase distinguishes the different Z_3 sectors at imaginary chemical potential. We will use $\langle L \rangle$ for both those purposes in section 5.7.2.

Since the calculation of correlation functions suffers from the neglect of long range interactions [96], we are primarily interested in bulk thermodynamic quantities. We therefore will investigate baryon number density, pressure, energy density and nuclear binding energy. The first three, being thermodynamical quantities, can be directly derived from the partition function,

$$\begin{aligned} a^3 n_B &= \frac{1}{N_\tau N_\sigma^3} \frac{\partial}{\partial a \mu_B} \ln Z, \\ a^4 p &= \frac{1}{N_\tau N_\sigma^3} \ln Z, \\ a^4 e &= -\frac{a}{N_\tau N_\sigma^3} \frac{\partial}{\partial a} \ln Z \Big|_z, \end{aligned} \tag{5.5}$$

where the the derivatives in the last line are to be taken at constant fugacity $z = e^{\mu/T}$.

Besides those quantities we are interested in the nuclear binding energy ϵ. This is the binding energy between the nucleons, created by the residual attractive baryon-baryon potential. To calculate this quantity we first calculate the energy density using eq. 5.5. From this we subtract the rest mass contained in the system, $n_B m_B$ and normalize with respect to the baryon mass and the baryon number density in order to get a dimensionless quantity,

$$\epsilon \equiv \frac{e - n_B m_B}{n_B m_B}. \tag{5.6}$$

In the limit of low temperatures, where thermal excitations can be neglected, ϵ is then equal to the nuclear binding energy.

5.3 Validity of Stochastic Quantization

In this section we want to check the validity of the method of stochastic quantization for our model. This is necessary, because there are known case where stochastic quantization

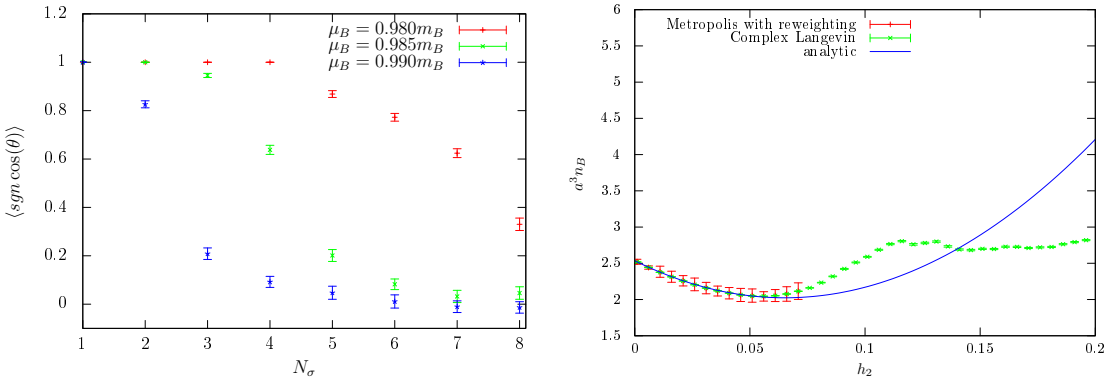

FIGURE 5.2: Left: Average sign of the phase of the determinant, $\cos(\theta)$, plotted against the spatial lattice extent N_σ, Parameters are $\kappa = 0.01$, $N_f = 3$ and $\beta = 0$. Right: Numerical instabilities at large values of h_2 lead to failure of Monte-Carlo and Complex Langevin algorithm.

leads to wrong results when it is applied to systems with a complex action [72–75]. We therefore compare results obtained from simulations with Monte-Carlo using reweighting in the phase of the determinant, see section 3.5.2, and stochastic quantization, see section 3.3.3. We furthermore perform two tests that have been proposed in order to check the reliability of Stochastic Quantization when simulating a given model.

5.3.1 Comparison between Stochastical Quantization and Monte-Carlo

As can be seen in fig. 5.2 the sign problem of our effective theory is mild enough to pose no problem for the use of reweighting, as long as we use small spatial lattice sizes. We therefore perform the comparison on small lattices with a volume of only $V = 4^3$. Since at $\kappa = 0.01$ the Compton wavelength of a pion is far smaller than one lattice spacing, this is still a valid approximation. In fig. 5.3 we show the expectation values of the quark number density and the Polyakov loop plotted against the chemical potential.

It has to be emphasized that in this case $\langle L\rangle \neq 0$ does not signal a deconfinement transition, since the argument made in section 2.3.1 does not hold for large densities. In dense systems color charges are screened by the medium, leading to $\langle L\rangle \neq 0$. At higher chemical potential lattice saturation sets in, and we again have $\langle L\rangle \approx 0$, since that lattice is now filled with color neutral states.

As fig. 5.3 shows, Stochastic Quantization and Monte-Carlo agree well.

5.3.2 Criteria for Correctness

Previous failures of the Stochastic Quantization method have been linked to an broad distribution of the degrees of freedom in the complex plane. A criteria has been proposed to check whether the distribution is localized enough to produced correct results [85]. This is done by applying the Langevin operator $\hat{L}$ to every observable. The criteria is

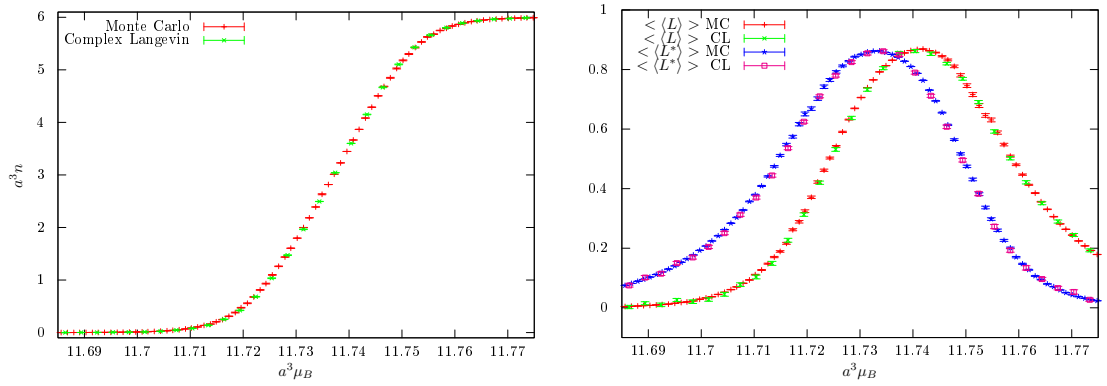

FIGURE 5.3: Comparison between stochastic quantization and Monte-Carlo with reweighting for different values of μ_B. Shown are the quark number density (left) and the Polyakov loops and its adjoint (right). Parameters are $N_\tau = 100, \beta = 0$ (left) and $\beta = 5.7, \kappa = 0.01$ and $N_\tau = 200$ (right), both with $N_f = 1$ and $V = 4^3$.

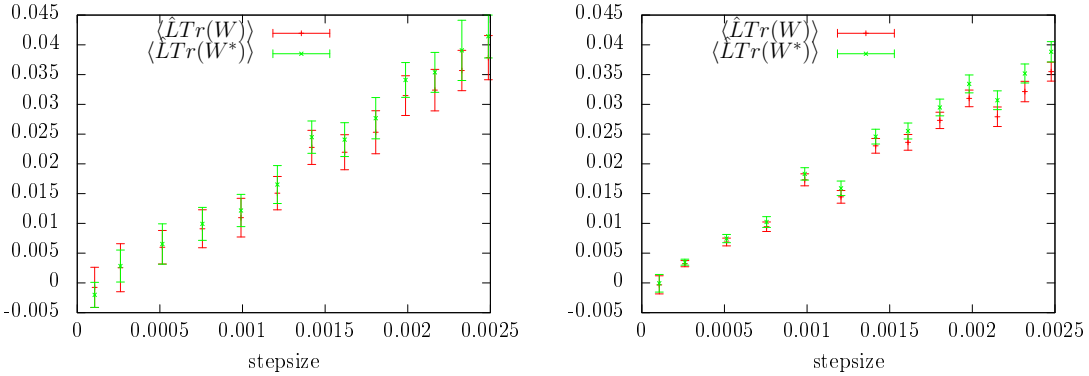

FIGURE 5.4: Applying the criteria in eq. 5.7 to $L = \mathrm{Tr}W$ and $L^* = \mathrm{Tr}W^\dagger$, using our effective theory to order κ^2 (left) and κ^4 (right). Parameters are $V = 10$, $\kappa = 0.0245$, $N_\tau = 50$, $a\mu_B = 9.7$ and $\beta = 6$.

fulfilled if for every observable we have

$$\langle \hat{L}O \rangle = 0, \quad \hat{L} = \sum x, a \Big(\frac{\partial}{\partial \phi_a(x)} - \frac{\partial S}{\partial \phi_a(x)} \Big) \frac{\partial}{\partial \phi_a(x)}. \tag{5.7}$$

Since in our model all observables can be expressed as functions of L and L^*, it is sufficient to check those. As can be seen in fig. 5.4 the criteria are fulfilled in the limit of vanishing stepsize.

5.3.3 The logarithm of the static determinant

Another possible source for wrong results produced by Stochastic Quantization was given in [102]. Fermionic systems have an effective action proportional to $\log(\det Q)$. For complex arguments the logarithm develops a cut along the negative real axis and is therefore multivalued. In [102] it was discovered that, for the random matrix model, wrong results were produced when derivatives frequently have to be taken across this

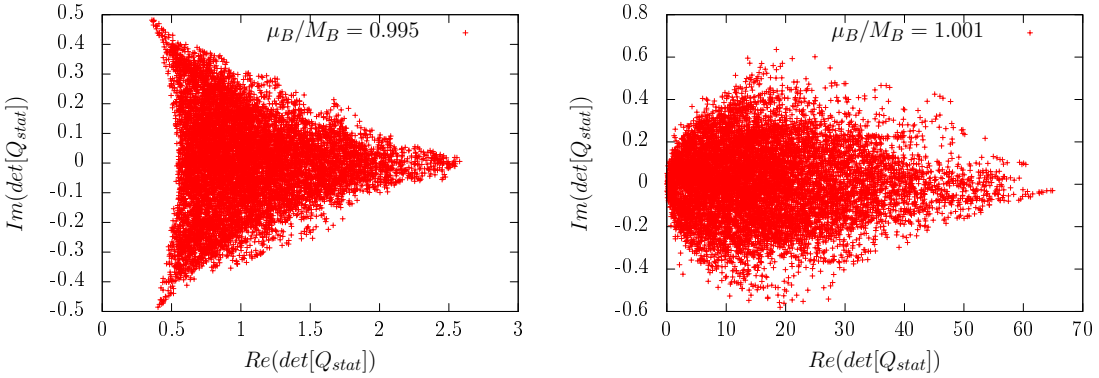

FIGURE 5.5: Distribution of the static determinant, eq. 4.20, in the complex plane for low and high chemical potential with $\kappa = 0.0173, N_\tau = 100$ and $\beta = 0$. No crossings of the negative real axis occur.

cut.

Since in our model all higher orders are being exponentiated, see section 4.5, no logarithm appears for those contributions. This only happens for the leading order, i.e. the static determinant, see eq. 4.20. In fig. 5.5 we observed the logarithm of the static determinant at low and high chemical potential. As can be clearly seen the real part of the determinant is always positive, therefore no crossings of the branch cut occur.

Together with the comparison with analytic results, which we will present in chapter 6, the three tests shown here make us confident that Stochastic Quantization works well in the convergence region of our effective theory.

5.4 Numerical Stability

While the effective theory is always numerically stable in the static limit, at higher orders one can get instabilities due to truncation effects. To demonstrate this, we compare numerical results from simulations using Monte-Carlo and Stochastic Quantization with analytic results (see chapter 6 for details regarding the analytic results). As can be seen on the right side of fig. 5.2, the Monte-Carlo algorithm breaks down at $h_2 \approx 0.07$. Stochastical Quantization seems to keep working, but qualitatively differs from the analytic result. Since this happens in a parameter region where the hopping expansion is no longer convergent, this has no consequences for our investigations. Both algorithms as well as the analytic results agree in the parameter region we will be working in.

5.5 Convergence to full QCD

The most important property of our effective theory to consider is the size of the parameter region where it is a good approximation to full LQCD. The parameter region is

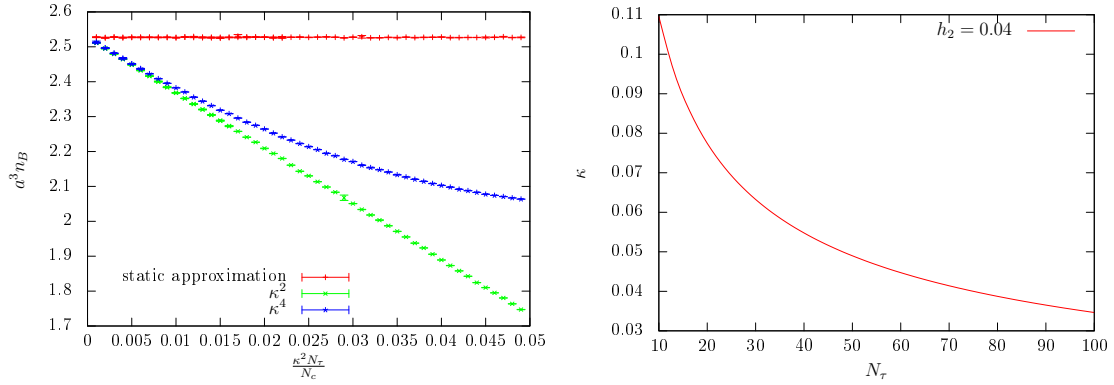

FIGURE 5.6: Left: Baryon density for $N_f = 3$ calculated with action truncated at different orders in the hopping expansion, $V = 6^3, \beta = 0$. Baryon chemical potential was tuned to fix $h_1 = 0.8$, making the contribution from the static determinant constant.
Right: Maximal value of κ that is still in the convergence region, $h_2 <= 0.04$

defined by the input parameters of the original theory, i.e. β, κ and N_τ. We distinguish three different sources of truncation effects that we can test independently:

- The first source of truncation errors come from gauge corrections to the fermionic coupling constants, $h_1(\kappa, N_\tau, \beta), h_2(\kappa, N_\tau, \beta)$ and so on. The truncation effects for those contributions were already discussed in section 4.4. There we concluded that higher corrections should be small up to $\beta \approx 6$.

- The second contribution comes from the pure gauge action and can be further divided into two different sources of truncation effects. Firstly there are truncation effects in the coupling constants, $\lambda_1(\beta, N_\tau)$, $\lambda_2(\beta, N_\tau)$ and so on, which are only known to a certain order in β. Secondly there is an error due to neglecting higher order interactions, i.e. coupling constants for interactions over larger distances and between Polyakov loops in higher representations are set to zero. Both of those errors were already discussed in [89]. There it was concluded that, for small N_τ, convergence is good up to the deconfinement transition. This does not hold for the region of large N_τ we want to consider in order to investigate low temperature QCD. However, because of the considerations in section 4.4, we will not go beyond $\beta \approx 6$, and, as discussed in section 4.7, all pure gauge couplings go to zero for large values of N_τ and fixed β.

- The remaining uncertainty concerns the truncation of the expansion in eq. 4.11. In the following we will investigate how fast this error grows as we leave the limit of infinite quark mass.

5.5.1 Convergence of the Hopping Expansion

Since we integrated out the temporal dimension, the effective expansion parameter of our theory is $h_2 = \frac{\kappa^2 N_\tau}{N_c}$ rather than just κ. Strictly speaking this is only true in the cold and dense limit, since in the full effective theory additional contributions that are of subleading order in N_τ appear. We will nevertheless use it as an approximation since

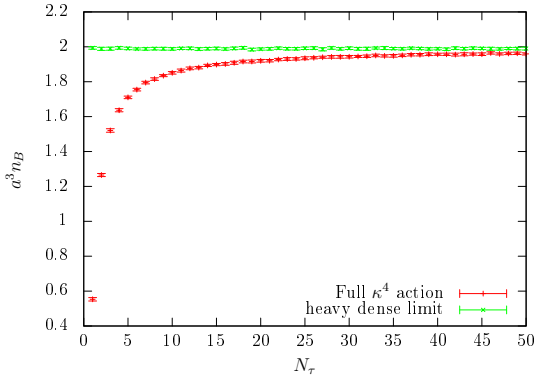

FIGURE 5.7: Comparison between the full κ^4 theory and the heavy dense limit shown in eq. 4.63 for $\beta = 0, V = 4^3, N_f = 1$. Chemical potential and κ were fixed such that $h_1 = 0.8$ and $h_2 = 0.05$, meaning that the action in eq. 4.63 will be constant.

it greatly simplifies the problem while still giving a good estimate, especially if N_τ is large. We will see in section 5.6.1 how large N_τ has to be in order to justify such approximations.

In order to check the convergence properties of the hopping expansion we go to the strong coupling limit, $\beta = 0$, and perform simulations at different values of h_2. In order to judge convergence we calculate the baryon number density using the effective action truncated at $O(\kappa^0)$, $O(\kappa^2)$ and $O(\kappa^4)$. The behaviour of the respective expectation values $\langle a^3 n_B \rangle_{k^0}$, $\langle a^3 n_B \rangle_{\kappa^2}$ and $\langle a^3 n_B \rangle_{\kappa^4}$ is then compared at different values of h_2. The region of convergence for an order κ^a is then determined by setting a desired accuracy α and searching for the point where $\langle a^3 n_B \rangle_{\kappa^{a+2}}$ diverges by more than this threshhold. We therefore define our criteria for convergence as

$$\left| \frac{\langle a^3 n_B \rangle_{\kappa^{a+2}}}{\langle a^3 n_B \rangle_{\kappa^a}} - 1 \right| < \alpha. \tag{5.8}$$

We decide to set our desired accuracy to 10%, i.e. $\alpha = 0.1$. The results are shown in fig. 5.6. We scaled $a\mu_B$ in such a way that h_1, and therefore $\langle a^3 n_B \rangle_{\kappa^0}$, is constant. As we can see the static κ^0 approximation is valid up to $h_2 \approx 0.015$, while the κ^2 approximation converges up to $h_2 \approx 0.04$. The convergence radius of the κ^4 approximation can not be determined without the κ^6 action. The left side of fig. 5.6 shows the values of κ for different N_τ if we fix $h_2 = 0.04$. At lower values of N_τ, i.e. higher temperatures, larger κ and therefore lighter quarks can be achieved. Probing low temperatures therefore restrict us to the use of heavy quarks, while at larger temperatures the simulation of lighter quarks is possible.

5.6 Low Temperature

In this section we will investigate the cold dense limit. This is equivalent to the region of the QCD phase diagram described in section 2.5.2. As discussed in section 2.2, temperature in an Euclidean field theory is equivalent to the inverse extent of the temporal dimension, so on the lattice we have the temperature $T = \frac{1}{aN_\tau}$. We therefore can reach low temperatures by increasing the number of timeslices N_τ or the lattice spacing a. Since we will want to extrapolate to the continuum by taking $a \to 0$ we will fix the temperature by varying N_τ.

This suggest the use of the limit discussed in section 4.7, so we will begin with testing the validity of this approximation in section 5.6.1. After that we perform continuum extrapolations of various observables in the sections 5.6.2 and 5.6.3. Section 5.6.4 finally discusses the existence of a first order liquid-gas transition to cold nuclear matter.

Most of the results presented in this section have already been published [91, 92].

5.6.1 Convergence of the heavy dense limit

As a first step we want to investigate the validity region of the heavy dense limit approximation. We do this by comparing the action given in eq. 4.63 to the full κ^4 action as shown in appendix A. In the approximation subleading orders in N_τ, pure gauge and anti-quark contribution are neglected. Fig. 5.7 shows the comparison between both actions plotted against the number of timeslices. We scale the parameters in such a way that observables calculated with the approximated action are constant. The approximated action shows the expected $\frac{1}{N_\tau}$ convergence to the full result, giving a result better than 10% at $N_\tau = 10$, better than 5% for $N_\tau = 20$ and better than 2% for $N_\tau = 50$. An error of 2% can be considered to be small compared to the error of up to 10% due to the truncation of the hopping expansion in section 5.5. We will therefore use the approximated action whenever we work with $N_\tau \geq 50$ and keep this additional error in mind. We will return to the use of the full action when working at high temperatures in section 5.7. Together with the estimate given in sections 4.4 and 5.5 this concludes our discussion of the convergence properties of our effective theory.

5.6.2 Setting a scale

As discussed in chapter 2 we need to take the limit of vanishing lattice spacing, $a \to 0$, in order to recover continuum QCD from LQCD. Therefore simulations at different values of a with a subsequent extrapolation have to be performed. Because of the running coupling, see section 2.2, quark masses and gauge coupling depend on the energy scale or, equivalently, on the distance, i.e. the lattice spacing. We can therefore determine the lattice spacing as a function $a = a(\beta, \kappa)$. Since the gauge coupling g goes to zero for close range the limit $a \to 0$ corresponds to $\beta = \frac{2N_c}{g^2} \to \infty$.

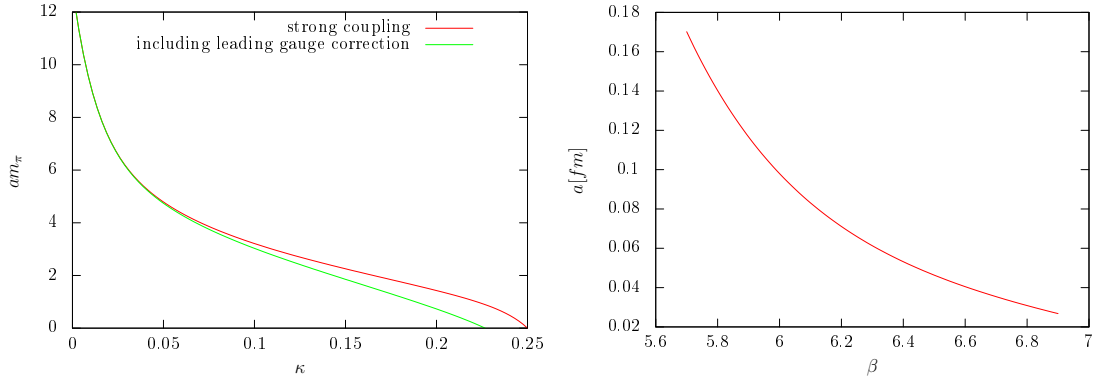

FIGURE 5.8: Left: Strong coupling pion mass with and without leading gauge corrections, eq. 5.11. For heavy quarks pion masses are reasonably well approximated by their strong coupling value. Right: Running of the lattice spacing with respect to β, eq. 5.9

In order to determine $a(\beta, \kappa)$ we use the fact that heavy quarks have only a small influence on the running of the coupling, i.e. for small κ we can approximate $a(\beta, \kappa) = a(\beta)$. We then use the non-perturbative beta function of the pure gauge theory to fix the lattice spacing. For this we use the interpolation function [103]

$$\begin{aligned} a(\beta) = r_0 \exp[&- 1.6804 - 1.7331(\beta - 6) \\ &+ 0.7849(\beta - 6)^2 - 0.4428(\beta - 6)^3], \quad 5.7 < \beta < 6.92, \end{aligned} \tag{5.9}$$

with the Sommer parameter $r_0 = 0.5$ fm.

Furthermore, the continuum extrapolation has to be performed along lines of constant physics. We will do this by computing the baryon mass in lattice units, $am_B(\beta, \kappa)$, and use this to tune $a(\beta)$ while keeping the ratio $\frac{m_\pi}{T}$ constant as we approach the continuum. In order to compute the baryon mass we use the fact that hadron masses can be calculated exactly in the strong coupling limit [104]. For $\beta = 0$ the masses of pions and nucleons built from $N_f = 2$ degenerate quarks are

$$\begin{aligned} \cosh m_{\pi,\beta=0} &= 1 + \frac{(M^2-4)(M^2-1)}{2M^2-3}, \\ \exp m_{B,\beta=0} &= \frac{M^3(M^3-2)}{M^3-5/4}, \end{aligned} \tag{5.10}$$

with $M = \frac{1}{2\kappa}$. Leading gauge corrections to all orders in κ are also known [105], starting with

$$\begin{aligned} am_\pi &= m_{\pi,\beta=0} - 24\kappa^2 \frac{u}{1-u}, \\ am_B &= m_{B,\beta=0} - 18\kappa^2 \frac{u}{1-u}, \quad u = \frac{\beta}{18} + \mathcal{O}(\beta^2) \end{aligned} \tag{5.11}$$

β	a[fm]	N_τ	κ
5.70	0.170	116	0.000089
5.75	0.152	130	0.000224
5.80	0.136	144	0.000491
5.85	0.123	160	0.000964
5.90	0.112	176	0.001724
5.95	0.102	194	0.002851
6.00	0.093	211	0.004419
6.05	0.086	230	0.006487
6.10	0.079	250	0.009098

TABLE 5.1: Parameters for continuum extrapolation with $T = 10$MeV and $\frac{m_\pi}{T} = 2000$.

As can be seen on the left plot of fig. 5.8 the leading gauge corrections vanish in the limit of heavy quarks. As we will restrict ourselves to heavy quarks, cf. table 5.1, we can use eq. 5.11 as an approximation for the hadron masses.

5.6.3 Continuum extrapolation

We are now ready to perform continuum extrapolations along lines of constant physics. We begin our calculation with setting the desired temperature T. Knowing that 1 fm = 197 MeV we can then use this value to determine N_τ as a function of the lattice spacing,

$$N_\tau(T, \beta) = 197 \, \frac{\text{MeV}}{T} \frac{\text{fm}}{a(\beta)}. \tag{5.12}$$

Having chosen a temperature we can therefore tune $a(\beta)$ by using eq. 5.9 and determine the respective $N_\tau(\beta)$ that keeps T constant by using eq. 5.12.

Next we have to set a pion mass. We do that by fixing the ratio $\frac{m_\pi}{T} = c$, which then gives

$$am_\pi(\kappa, \beta) = \frac{c}{N_\tau(\beta)}. \tag{5.13}$$

By solving eq. 5.11 for κ we can use this to determine $\kappa(\beta)$. We see that, after fixing T and c as input parameters, all other parameters are functions of β. This allows us to perform simulations at different values of the lattice spacing $a(\beta)$ and extrapolate $a \to 0, \ \beta \to \infty$.

Next we have to decide what values to choose for T and c. Since we have to rely on eq. 5.9 to determine $a(\beta)$, our range of accessible lattice spacings is limited. Furthermore our effective theory converges to full QCD only in a limited parameter region, see section 5.5, so we have to restrict our choice of $\frac{m_\pi}{T}$ to the region where $\frac{\kappa^2 N_\tau}{N_c} < 0.04$. With this in mind we choose a temperature of $T = 10$ MeV and $c = 2000$, which corresponds to a pion mass of $m_\pi = 20$ GeV. Varying β between 5.7 and 6.1 gives us the input parameters shown in table 5.1.

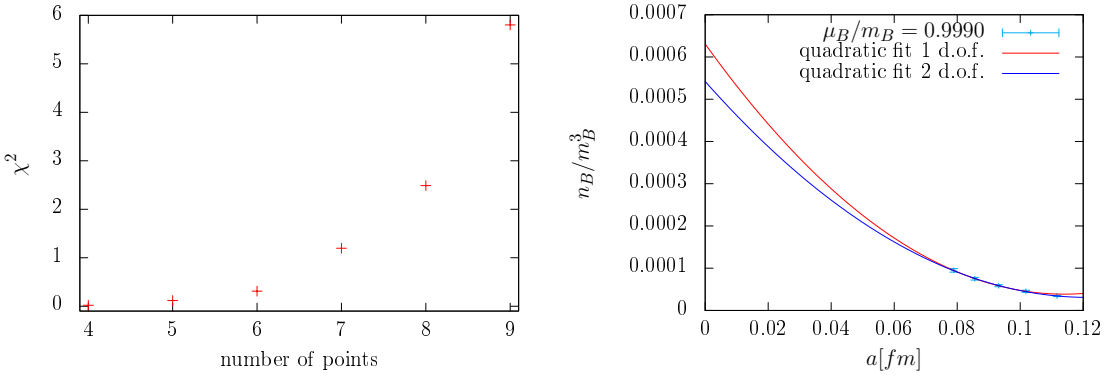

FIGURE 5.9: Left: Reduced χ^2 for quadratic fitting including different numbers of lattice spacings. Right: Density vs. lattice spacing, fitted quadratically including 4 and 5 lattice spacings.

After performing simulations at various values of β, we have to extrapolate. Since our theory is based on unimproved Wilson fermions, see section 3.2.2, corrections due to finite lattice spacing are expected to start at $\mathcal{O}(a)$,

$$\frac{n_{B,\text{latt.}}}{m_B^3} = \frac{n_{B,\text{cont.}}}{m_B^3} + A(\mu)a + B(\mu)a^2 + O(a^3). \tag{5.14}$$

The normalization with respect to the baryon mass is necessary in order to get a dimensionless quantity. Note that only the constant term has a physical meaning. It is therefore preferable to fit the data with a polynomial of low order. While our lattice spacings seem much too coarse to permit a linear fit, a quadratic fit is possible. The left plot of fig. 5.9 shows the reduced χ^2 for different quadratic fits. We varied the number of data points included into the fit by excluding some of the coarsest lattices. As can be seen, the inclusion of too coarse lattices introduces higher order corrections and makes the quadratic fit worse. We therefore choose to use fits involving only our four and five finest lattices, leaving one and two degrees of freedom for the quadratic fit. We then use the difference between those fits as a measure for the uncertainty of the continuum result. On the right side of fig. 5.9 we show how this method yields a continuum value of $\frac{n_{B,\text{cont.}}}{m_b^3} = 0.00054 \pm 0.00009$ for $\frac{\mu_B}{m_B} = 0.999$. This process is repeated for a range of different values of μ_B.

As a next step the extrapolation $V \to \infty$ has to be performed in order to reach the thermodynamical limit. However, the finite size scaling effects are much smaller than statistical and fitting error. The reason for this is that heavy baryons have very short Compton wavelengths, $\lambda = 1/m_B \approx 0.01$fm. This makes the use of small lattices, in our case with a spatial extents of $aN_s = 0.5 - 0.7$fm, sufficient to suppress all finite size effects. On the other hand this means that our lattice is much too coarse to resolve any inner structures of the baryons.

In fig. 5.10, 5.11 and 5.12 we show the results for the continuum extrapolation of

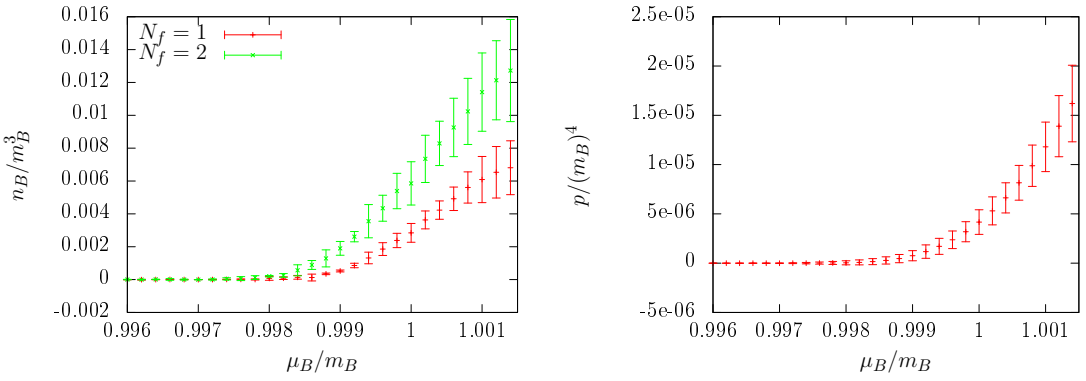

FIGURE 5.10: Continuum extrapolated results for baryon density (left) and pressure (right) with respect to chemical potential. Density is shown for $N_f = 1, 2$ degenerate flavors, pressure for $N_f = 2$ degenerate flavors. In both cases we have $V = 6^3$ and $m_\pi = 20$ GeV

baryon number density, pressure, energy density and binding energy. For baryon number density we show both the $N_f = 1, 2$ case for comparison. As can be seen going from one to two degenerate flavors adds roughly a factor of two to the density. The same is true for the other quantities for which we only show the $N_f = 2$ case. Continuum extrapolation becomes less reliable when one goes beyond $\frac{\mu_B}{m_B} = 1$. The reason for this is the unphysical lattice saturation once the lattice starts to fill up with quarks. Due to the Fermi principle each lattice site can only be filled with up to $2N_cN_f$ quarks. Approaching this limit requires the use of increasingly finer lattices to resolve physical effects. Because of this we cut the data at $\frac{\mu_B}{m_B} = 1.0012$. In fig. 5.12 we additionally show the baryon number density for different temperatures. Note that the error grows as the temperature is lowered. This signals the breakdown of our effective theory as N_τ is raised.

Several interesting observation can be made from our results. The onset to the region of finite density happens at $\mu_B < m_B$. This is consistent with the existence of a finite binding energy. Since our quarks are very heavy, the difference is small. This is confirmed by the results shown in fig. 5.11, which indicate a binding energy of approximately 0.1 % of the baryon mass at the onset, compared to approximately 1.7 % as assumed for nuclear matter with physical quark masses [16]. While our results do show the existence of a finite binding energy, they do not show a minimum like in fig. 2.4. We believe that the reason for this is the influence of saturation effects that set on as we approach $\mu_B = m_B$.

Furthermore, the data in fig. 5.12 demonstrates what is known as the Silver Blaze property [67]. The density is independent of μ_B as long as we are in the region where $\mu_B < \mu_c = m_B - \epsilon m_B$, despite the fact that the chemical potential explicitly enters the partition function.

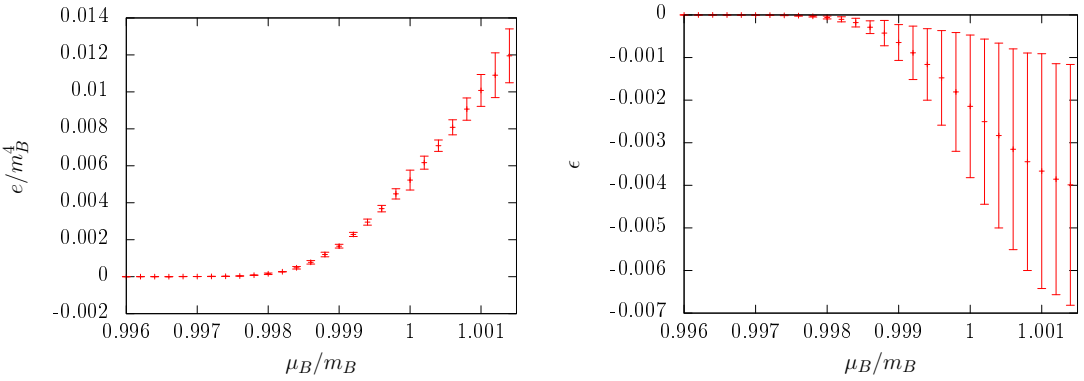

FIGURE 5.11: Continuum extrapolated results for energy density (left) and binding energy (right) for two degenerate flavors, $V = 6^3$ and $m_\pi = 20$ GeV

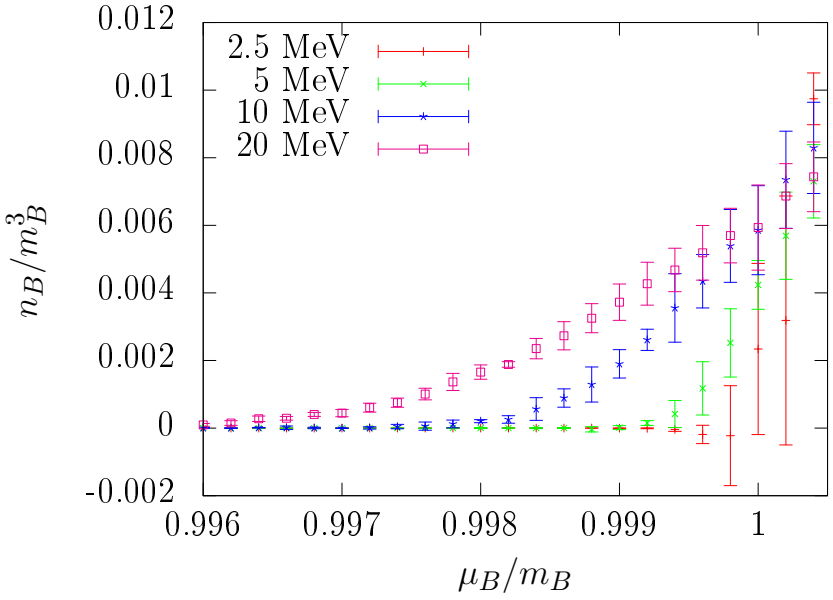

FIGURE 5.12: Continuum extrapolated results for the baryon density with $N_f = 2$,$V = 6^3$ and $m_\pi = 20$ GeV for different Temperatures.

5.6.4 Liquid-Gas Transition to Nuclear Matter

In section 2.5.2 we discussed the fact that the transition to nuclear matter should be of first order at low temperatures, turning into a crossover as temperature is raised. Scaling analysis of the transition shown in fig. 5.12 shows it to be a smooth crossover for quark masses and temperatures reachable in our effective theory. Since $T = 2.5$MeV lies below the critical temperature suggested by experiment [34], this is likely to be caused by the unphysical quark masses.

Nevertheless we want to test whether the change to a first order transition can be described at least qualitatively in our effective theory if we lower the quark masses sufficiently. For this we raise the hopping parameter to $\kappa = 0.12$ and probe low temperatures by going to temporal lattice extents up to $N_\tau = 1000$. Since this means $\frac{\kappa^2 N_\tau}{N_c} > 1$ we

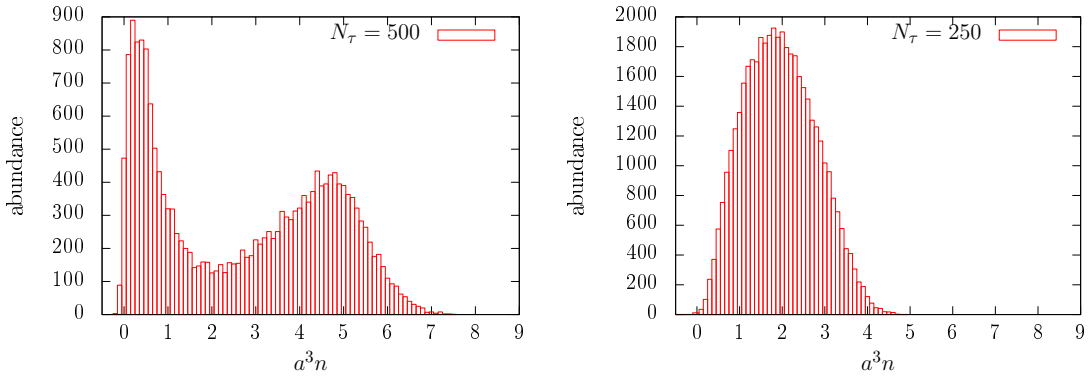

FIGURE 5.13: Distributions of the quark density for two different temperatures. At low temperatures (left) the distributions shows the coexistence of two phases, signaling a first order transition. As the temperature is raised (right) the transition turns into a crossover. Both plots made with $\kappa = 0.12, N_f = 1, \beta = 5.7$.

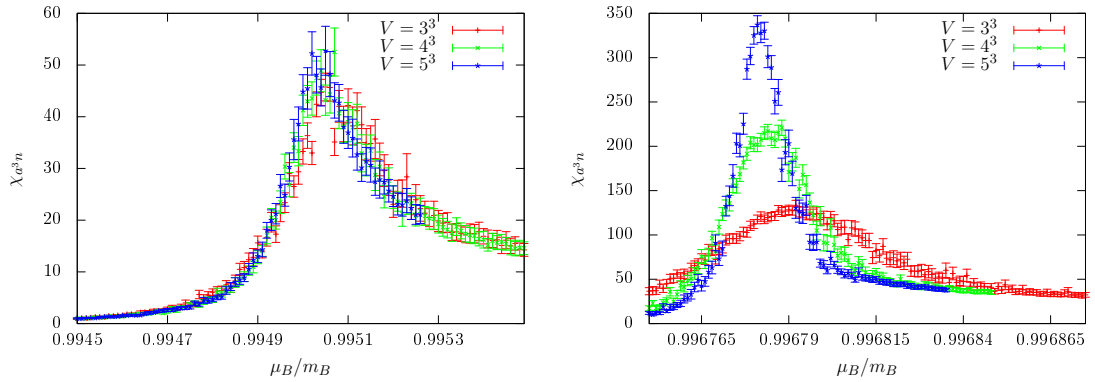

FIGURE 5.14: Quark number susceptibility for the transition to nuclear matter. At low temperatures (left) volume scaling indicates are phase transition, while at higher temperatures (right) scaling indicates a crossover. Same parameters as in fig. 5.13

are far outside the region of convergence we determined in section 5.5. It can therefore not be expected that our results represent QCD quantitatively. It is nevertheless encouraging to see that our model indeed predicts a change from a crossover to a first order transition as temperature is lowered. Fig. 5.13 shows the distribution of the quark number density at temperatures above and below the critical endpoint. At low enough temperatures there is a coexistence between the vacuum and a finite density phase, signaling a first order transition. This is confirmed by the finite size scaling of the quark number susceptibility shown in fig. 5.14. At higher temperature this changes into a crossover, where no region with coexisting phases is present and the quark number susceptibility does not scale with the volume. Since we are outside of the region of convergence and therefore can not make any quantitative statements we do not attempt to locate the exact location of the critical endpoint or extract critical exponents.

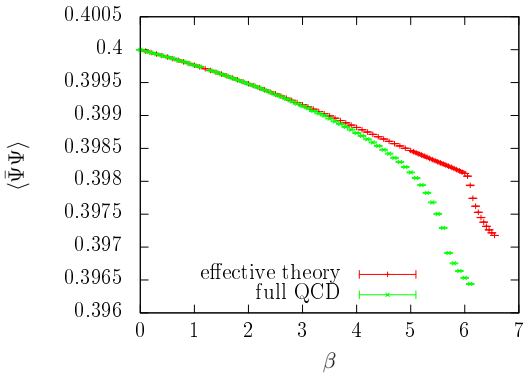

FIGURE 5.15: Chiral Condensate for two flavour heavy Wilson quarks from full QCD and effective theory, $\kappa = 0.4, N_\tau = 4, V = 4$.

5.7 High Temperature

In this section we use our theory to investigate QCD at high temperatures. This corresponds to the use of small N_τ, thus, in contrast to the previous section, we now have a significant contribution from the pure gauge action due to λ_1 being large. Furthermore, this means that we can access much lighter quarks while still staying in the convergence region of the strong coupling and hopping expansion, cf. fig. 5.6. In this section we will investigate two topics. Both concern either zero or imaginary chemical potential, therefore we can compare our results with full LQCD simulations since there is no sign problem.

In section 5.7.1 we will use our effective theory to calculate the chiral condensate as a function of temperature. Using Wilson quarks, chiral symmetry is always broken explicitly, see section 3.2.2. Nevertheless, small effects due to the restoration of spontaneous symmetry breaking are visible in LQCD simulations [19]. We will try to reproduce those results.

Furthermore we are interested in the nature of the Roberge-Weiss critical endpoints at imaginary chemical potential, see section 2.3.3. This topic was already investigated using the effective theory presented in this thesis, but including only the static quark determinant [89, 90]. Despite the neglect of higher order corrections this was sufficient to locate the first Roberge-Weiss tricritical point in accordance with [19]. In section 5.7.2 we will try to expand on these results using our improved $\mathcal{O}(\kappa^4)$ action.

5.7.1 Chiral Condensate

In order to test whether our heavy quark effective theory maintains the feature of partial chiral symmetry restoration we calculate the chiral condensate and compare it with full LQCD with Wilson quarks, simulated with the software presented in [106] [1]. This is

[1] Many thanks to Georg Bergner for providing the LQCD data.

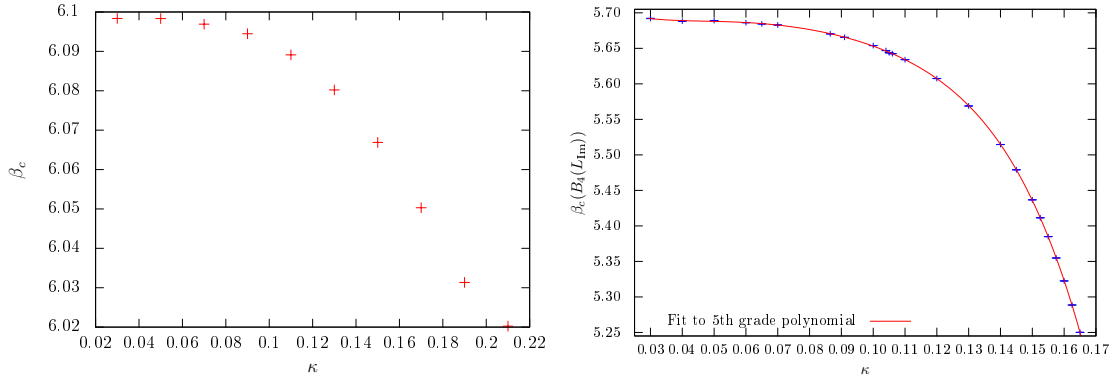

FIGURE 5.16: Comparison of β_c for effective theory (left) and full QCD (right) for $N_\tau = 4$ and $N_f = 2$. Full QCD results taken from [19].

done at vanishing chemical potential. The chiral condensate is given by

$$\langle \bar{\psi}\psi \rangle = \frac{1}{N_\tau N_\sigma^3} \frac{\partial \ln Z}{\partial m_q} \tag{5.15}$$

with $m_q = \frac{1}{2\kappa}$. As can be seen in fig. 5.15 the difference between our effective theory and full QCD grows with β. The reason for this is the neglect of higher order effects. The effective theory gives three leading contributions to the chiral condensate:

- The value at $\beta = 0$ is a trivial contribution due to the rescaling of the quark fields in the Wilson fermion action, cf. section 3.2.2.

- The decrease between $0 < \beta < \beta_c$ is caused by vacuum graphs of order $\kappa^4 u$ and $\kappa^6 u^2$ consisting of diagrams that are of similar type as the one in eq. 4.52, but without winding around the lattice. They are not included in the action because they cancel out when calculating thermodynamical expectation values.

- The decrease at β_c is caused by the κ dependent corrections to $\lambda_1 = \lambda_1(\beta, N_\tau, \kappa)$ which we discussed in section 4.4.3.

We see that the behaviour of the chiral condensate in the confined phase is well described. The partial restoration at the critical temperature is reproduced qualitatively. The disagreement in β_c is about 10% as in the pure gauge theory [89].

5.7.2 Roberge-Weiss Transition

As already discussed in section 2.3.3 the transition between different Z_3 sectors at imaginary chemical potential changes from first order to a crossover as temperature is lowered, with the nature of the endpoint depending on the quark masses. In [90] the location of the heavy tricritical Roberge-Weiss point was located at $\kappa_{\rm light}^{\rm tric} = 0.1048 \pm 0.0008$ for $N_\tau = 4$. This was done by using an effective theory with the static determinant eq. 4.19 together with the gauge corrections to h_1 shown in eq. 4.47 and the pure gauge contribution eq. 4.7. This has been confirmed by full LQCD calculations, which found

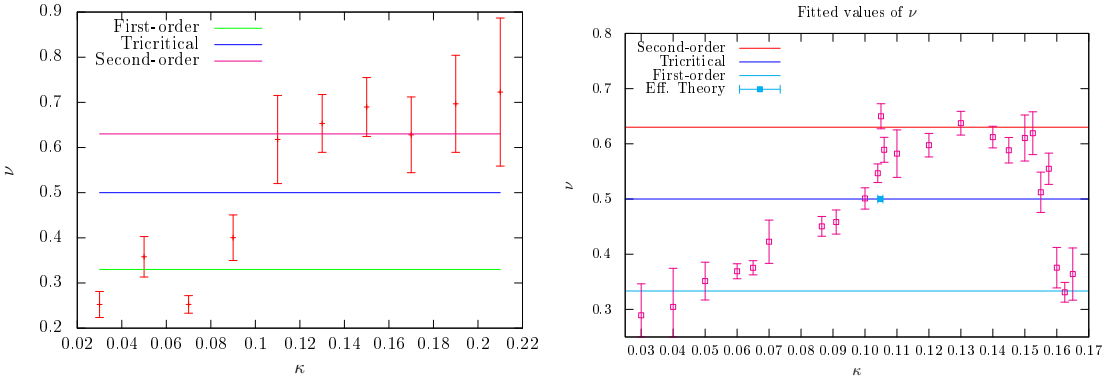

FIGURE 5.17: Comparison of critical exponents extracted from the effective theory (left) and full lattice QCD (right) for $N_\tau = 4$ and $N_f = 2$.

two tricritical points at $\kappa^{\text{tric}}_{\text{heavy}} = 0.1000 \pm 0.090$ and $\kappa^{\text{tric}}_{\text{light}} = 0.1550 \pm 0.050$ [19]. We try to locate the second tricritical point by using our $\mathcal{O}(\kappa^4)$ effective theory.

For this we perform simulations on lattice sizes $N_\sigma = 8, 10, 12$ with $N_\tau = 4$ and $N_f = 2$ degenerate flavors. The chemical potential is fixed to $\frac{\mu}{T} = i\frac{\pi}{3}$. As an order parameter we use the absolute value of the imaginary part of the Polyakov loop, $|\text{Im}(L)|$. The critical temperature β_c is extracted by using the Binder cumulant [107],

$$B_4(X) = \frac{\langle X - \langle X \rangle \rangle^4}{\langle X - \langle X \rangle \rangle^2}. \tag{5.16}$$

The Binder cumulant of the order parameter, calculated on lattice of different size, will intersect at β_c. Alternatively this can be done by locating the maximum of the susceptibility,

$$\chi(X) = V \langle X - \langle X \rangle \rangle^2, \tag{5.17}$$

in the infinite volume limit. The result for β_c is shown in fig. 5.16. As was already discussed in [89] the pure gauge transition temperature is reproduced with an accuracy of around 5%. Since the chemical potential does not enter in the pure gauge case this does not change at imaginary chemical potential. As finite quark masses are introduced, β_c decreases. Our effective theory describes this well for small κ, but the slope is significantly different as we move to larger values of κ.

To extract the critical exponent we apply the same method as in [19]. Around β_c the Binder cumulant is assumed to have finite size corrections going as

$$B_4(\beta, N_\sigma) = B_4(\beta, \infty) + a_1(\beta - \beta_c) N_\sigma^{\frac{1}{\nu}} + \mathcal{O}((\beta - \beta_c)^2). \tag{5.18}$$

If we are close to β_c higher orders can be neglected. Calculating the Binder cumulant on different lattice volumes then allows the extraction of the critical exponent ν.

Our results for ν are shown in fig. 5.17. As can be seen the effective theory reproduces the location of the first Roberge-Weiss tricritical point from [19]. However the second tricritical point is missing, even when looking at values of κ that are much larger than the ones investigated in [19].

We assume that this is not caused by the truncation of the pure hopping expansion. The use of small N_τ means our expansion parameter at the assumed location location of the second tricritical point is small, $\frac{(\kappa_{\text{light}}^{\text{tric}})^2 N_\tau}{N_c} \approx 0.032$. Furthermore, the couplings h_1 and $\bar{h}_1$ are small at imaginary chemical potential. Since powers of those couplings enter at all higher orders this should greatly improve the convergence. We therefore expect the convergence to be even better than in the cold dense limit shown in section 5.5. Gauge corrections discussed in section 4.4 to the fermionic couplings should also be well under control.

We therefore assume the problem to be caused by the neglect of gauge interactions between Polyakov loops in higher representations and at larger distances, which will receive κ dependent corrections due to mixing terms.

Chapter 6

Analytic Treatment of the Effective Theory

In chapter 5 we saw how the effective theory can be solved numerically. In addition to this, our effective theory can also be solved analytically by the use of perturbation theory. For this we use the fact that the static strong coupling limit, i.e. $\beta = \kappa = 0$, can be solved exactly. Corrections coming from the kinetic determinant are then expanded in the nearest neighbour coupling, h_2. This parameter has to be small since otherwise our effective theory would not converge to full lattice QCD.

Besides reproducing the results we already presented in the last chapter, this leads to additional insight into the structure of the theory. We already published the analytic results for the leading and next-to-leading order, i.e. for the static fermion determinant and $\mathcal{O}(\kappa^2)$ corrections, in [91, 92]. Here we will demonstrate how those results have been derived and expand them to the next order.

We will start with discussing the analytic solution of the quark determinant in the strong coupling limit in section 6.1. In section 6.2 we show how gauge corrections can be included. We then combine those results to repeat the continuum extrapolation from section 5.9 in section 6.3, using purely analytic expressions. Finally, in section 6.4, we provide a scheme for resumming the analytic solution, improving its region of convergence beyond that of the original effective theory.

6.1 Quarks in the strong coupling limit

In this section we derive an analytic solution for our effective theory in the strong coupling limit. Section 6.1.1 is concerned with the case of static quarks, which can be solved exactly. Here we demonstrate the basic recipe for deriving analytic expressions for different observables. The sections 6.1.2 and 6.1.3 expand this to the next orders.

6.1.1 Static Limit

In this section we solve the partition function for a system of static quarks in the strong coupling limit. For this we have to solve eq. 4.20,

$$Z = \int [dU_4] \prod_i ([1 + h_1 L_i^* + h_1^2 L_i + h_1^3][1 + \bar{h}_1 L_i^* + \bar{h}_1^2 L_i + \bar{h}_1^3])^{2N_f}. \tag{6.1}$$

Since there is no interaction between quarks at different lattice sites the gauge integral factorizes. If we denote the contributions of the spatial position x_i to the fermion determinant with Q_i^{stat}, we get

$$\int [dU_4] \prod_i Q_i^{\text{stat}} = \prod_i \int [dU_4] Q_i^{\text{stat}} = \prod_i z_0 = z_0^V. \tag{6.2}$$

In order to calculate z_0 we have to explicitly perform the gauge integration. We explain in appendix B how integrals of this type can be evaluated and list all integrals that are necessary for the following calculations. Since higher numbers of N_f lead to longer expressions we set $N_f = 1$ for now. After the integral is performed all dependence on link variables has vanished and we get

$$\begin{aligned} Z = z_0^V = &[(1 + 4h_1^3 + h_1^6) + (4h + 6h^4)\ \bar{h}_1 + (10h^2 + 6h^5)\ \bar{h}_1^2 \\ &+ (4 + 20h^3 + 4h^6)\ \bar{h}_1^3 + (6h + 10h^4)\ \bar{h}_1^4 \\ &+ (6h^2 + 4h^5)\ \bar{h}_1^5 + (1 + 4h^3 + h^6)\ \bar{h}_1^6]^V. \end{aligned} \tag{6.3}$$

We can already make several interesting observations from this result. Since h ($\bar{h}$) is the coupling constant for a single quark (anti-quark), a term $h^n \bar{h}^m$ corresponds to a state that is built from n quarks and m anti-quarks. All states have exponents that satisfy $m - n = \text{mod } N_c$, showing that after performing the gauge integration only color neutral states remain. Z therefore is the partition function of a non-interacting hadron gas consisting of baryonic and mesonic states. Furthermore, spin degeneracy factors can be read from the prefactors. For the first state, i.e. the first non constant term in eq. 6.3, the degeneracy is 4. We can interpret this as a spin $\frac{3}{2}$ quadruplet build from of 3 quarks. The second state is a spin 0 singlet consisting of 6 quarks. The next state is again a spin $\frac{3}{2}$ quadruplet, but build from a quark and an antiquark.

In order to map these states to physical particles we will have to go to $N_f = 2$. Doing so while keeping anti-quarks leads to very long formulas without introducing new conceptual difficulties. We therefore apply the limit discussed in section 4.7, where anti-quark contributions are exponentially suppressed and only baryonic states survive. We again have to solve eq. 6.1, this time setting $N_f = 2$ and $\bar{h}_1 = 0$. Using the integrals

given in appendix B we get

$$\begin{aligned} Z =&(1 + 4h_u^3 + h_u^6) + (6h_u^2 + 4h_u^5)h_d + (6h_u + 10h_u^4)h_d^2 + (4 + 20h_u^3 + 4h_u^6)h_d^3 \\ &+ (10h_u^2 + 6h_u^5)h_d^4 + (4h_u + 6h_u^4)h_d^5 + (1 + 4h_u^3 + h_u^6)h_d^6. \end{aligned} \tag{6.4}$$

Despite the fact that we already assumed all quarks to be degenerate in eq. 6.1 we introduce separate coupling constants h_u and h_d in order to distinguish the contributions from the different flavors. Eq. 6.4 describes all baryonic states that can be built out of up to 12 constituent quarks, while respecting the Fermi principle and color confinement. For example the state $h_u h_d^2$, i.e. *udd*, is sixfold degenerate. This can be divided into a spin 1/2 doublet, the proton and a spin 3/2 quadruplet, the Δ^+. The *udd* state correspondingly represents the neutron and the Δ^0. The Δ^{++} and Δ^- quadruplets correspond to *uuu* and *ddd*. Terms of higher order can be interpreted as combinations of those, forming di-baryon states.

Now that we calculated the partition function, deriving thermodynamical expectation values is straightforward. To demonstrate this we return to the full $N_f = 1$ partition function and perform the derivative with respect to the chemical potential μ. We get

$$\begin{aligned} a^3 n_B &= \frac{1}{3}\frac{1}{N_\tau N_\sigma^3}\frac{\partial \log Z}{\partial a\mu_q} \\ &= \Big[2(3h^4\bar{h} + 3h^5\bar{h}^2 - 3h\bar{h}^4 - 3h^2\bar{h}^5 - \bar{h}^3(2 + \bar{h}^3) + h^6(1 + 2\bar{h}^3) \\ &\quad - 2h^3(-1 + \bar{h}^6))\Big]\Big[1 + 4\bar{h}^3 + \bar{h}^6 + 2h^2\bar{h}^2(5 + 3\bar{h}^3) \\ &\quad + 2h^4\bar{h}(3 + 5\bar{h}^3) + h(4\bar{h} + 6\bar{h}^4) + h^5(6\bar{h}^2 + 4\bar{h}^5) \\ &\quad + h^6(1 + 4\bar{h}^3 + \bar{h}^6) + 4h^3(1 + 5\bar{h}^3 + \bar{h}^6)\Big]^{-1} \\ &\overset{h.d.}{=} \frac{4h_1^3 + 2h_1^6}{1 + 4h_1^3 + h_1^6}, \end{aligned} \tag{6.5}$$

with the last expression being valid in the heavy dense limit where anti-quarks can be neglected. This result demonstrates two features we already observed in the numerical simulations, the Silver Blaze property and Fermi saturation.

Fermi saturation, which we already saw in the results shown in fig. 5.3, can be seen from our analytic expression by taking the limit of high chemical potential, $\mu_B >> m_B$. In this limit we have $h_1 \to \infty$ and $\bar{h}_1 \to 0$. Expanding around both limits we get

$$\lim_{a\mu\to\infty} a^3 n_B = 2 + \mathcal{O}(\frac{1}{h^3}) + \mathcal{O}(\bar{h}^3). \tag{6.6}$$

This means we have a maximum of two baryons, or six quarks, per lattice site. In general the Fermi principle allows up to $2N_cN_f$ quark per site, with the factor of two accounting for spin. Note that saturation is a lattice effect that occurs due to the discretization,

there is no saturation in the continuum as one goes to asymptotically high chemical potential.

Silver Blaze behaviour denotes the independence of observables from the chemical potential below a critical value μ_c. In the zero temperature limit μ_c is $\mu_B - \epsilon m_B$, with ϵm_B being the nuclear binding energy. We saw this in the numerical results when we compared results at different temperatures, see fig 5.12. To extract this behavior from our analytic expression we take the limit $N_\tau \to \infty$, while staying in the region where $\mu_B < \mu_c \approx m_B$. In this limit both h and $\bar{h}$ go to zero exponentially, so we can expand to leading order in both couplings and get

$$\lim_{N_\tau \to \infty} a^3 n_B \overset{\mu < \mu_c}{=} \mathcal{O}(h^3) + \mathcal{O}(\bar{h}^3). \tag{6.7}$$

In the zero temperature limit the density therefore also gets suppressed exponentially as long as $\mu < \mu_c$. This confirms the behavior we saw in the numerical results.

Since we will later want to analytically calculate the binding energy we also calculate the energy density,

$$\begin{aligned} a^4 e &= \frac{a}{N_\tau N_s^3} \frac{\partial \ln Z}{\partial a} \\ &= \frac{a}{N_\tau N_s^3} \frac{\partial \kappa}{\partial a} \frac{\partial h_1}{\partial \kappa} \frac{\partial \ln Z}{\partial h_1} \\ &= \frac{a}{N_\tau N_s^3} \frac{N_\tau}{\kappa} \frac{\partial \kappa}{\partial a} \frac{\partial \ln Z}{\partial h_1} \\ &= a m_B a^3 n_B, \end{aligned} \tag{6.8}$$

where only the leading terms for $\frac{\partial \kappa}{\partial a} = -\kappa \frac{m_B}{3}$ and $a m_B = 3 \ln(2\kappa)$ were used. This is simply the energy of the rest mass contained in the system. The binding energy, as we defined it in eq. 5.6, is therefore zero in the static limit.

Knowing the analytic expression for the partition function, we can easily calculate all other thermodynamical observables by taking the respective derivatives. This is not the case for the Polyakov loop, so we will calculate $\langle L \rangle$ in order to demonstrate that we can also analytically derive expectation values. Using eq. 3.16 and the respective integrals

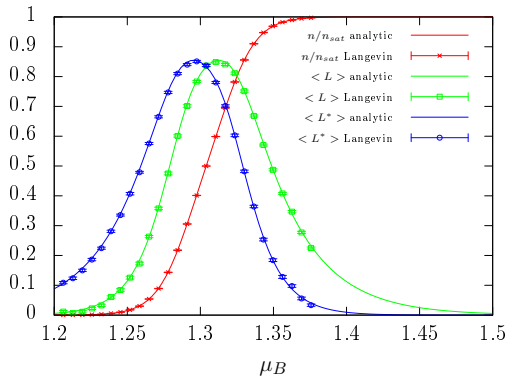

FIGURE 6.1: Comparison between simulation using stochastic quantization and analytic result for the static quark action, $N_\tau = 10$, $\kappa = 0.01$, $\beta = 0$.

from appendix B we get

$$\begin{aligned}
\langle L \rangle &= \frac{1}{Z} \int [dU_4] \prod_i (1 + hL_i + h^2 L_i^* + h^3)^2 (1 + \bar{h} L^* + \bar{h}^2 L + \bar{h}^3)^2 L \\
&= \frac{1}{Z} \Big[\int [dU_4] (1 + hL + h^2 L^* + h^3)^2 (1 + \bar{h} L^* + \bar{h}^2 L + \bar{h}^3)^2 \Big]^{V-1} \\
&\quad \Big[\int [dU_4] (1 + h_1 L + h_1^2 L^* + h_1^3)^2 (1 + \bar{h}_1 L^* + \bar{h}_1^2 L + \bar{h}_1^3)^2 L \Big] \\
&= \frac{1}{z_0} \Big[h^6 \bar{h} \left(3\bar{h}^3 + 2\right) + 2h^5 \left(\bar{h}^6 + 6\bar{h}^3 + 1\right) + h^4 \bar{h}^2 \left(8\bar{h}^3 + 15\right) \\
&\quad + 4h^3 \bar{h} \left(5\bar{h}^3 + 3\right) + h^2 \left(3\bar{h}^6 + 20\bar{h}^3 + 3\right) + 4h\bar{h}^2 \left(\bar{h}^3 + 2\right) + 3\bar{h}^4 + 2\bar{h} \Big]. \qquad (6.9)
\end{aligned}$$

We saw in fig. 5.3 that the Polyakov loop only takes a finite value around $\mu \approx m_B$. As we discussed in sections 2.3.1 and 5.3.1 this is due to the screening of color charges. We can easily see this behaviours from our analytic expression by taking the respective limits.

The complex conjugate of the Polyakov loop is calculated in an equivalent way, giving

$$\begin{aligned}
\langle L^* \rangle = \frac{1}{z_0} \Big[& h \left(3h^3 + 2\right) \mathrm{hb}^6 + 4h \left(5h^3 + 3\right) \bar{h}^3 + h \left(3h^3 + 2\right) + 2 \left(h^6 + 6h^3 + 1\right) \bar{h}^5 \\
& + \left(3h^6 + 20h^3 + 3\right) \bar{h}^2 + h^2 \left(8h^3 + 15\right) \bar{h}^4 + 4h^2 \left(h^3 + 2\right) \bar{h} \Big]. \qquad (6.10)
\end{aligned}$$

We end this section by comparing the analytic expressions for baryon number density, Polyakov loop and adjoint Polyakov loop with results obtained from simulations using stochastic quantization. As can be seen in fig. 6.1, the analytic solution for the static quark determinant agrees well with the numerical results. Indeed the solution we just derived is exact, since we did not have to rely on any approximations to perform the gauge integrals.

6.1.2 κ^2 corrections

The next step is to move away from the limit of static quarks. For this we will stay in the cold dense limit, i.e. use the approximate action discussed in section 4.7. The full action, i.e. the κ^2 contribution eq. 4.38 and the κ^4 contribution shown in appendix A, can be solved in an equivalent way, but leads to much longer formulas. For the same reason we keep $N_f = 1$. Introducing multiple degenerate flavors can, besides requiring the adjustments to the static determinant we already performed in the last section, can be achieved by modifying the respective prefactors in the hopping expansion as we explained in section 4.6.

The leading order contribution to the kinetic determinant was derived in section 4.3.2. The partition function we have to solve is

$$Z = \int [dU_4] \prod_i (1 + h_1 L_i^* + h_1^2 L_i + h_1^3)^2 \\ \times \exp[2h_2 \sum_{<i,j>} \mathrm{Tr} \frac{h_1 W_i}{\mathbb{1} + h_1 W_i} \mathrm{Tr} \frac{h_1 W_j}{\mathbb{1} + h_1 W_j}], \quad h_2 = \frac{\kappa^2 N_\tau}{N_c}, \tag{6.11}$$

with h_2 being the nearest neighbour coupling. In order to perform the gauge integral we have to rewrite the traces as Polyakov loops. We explain in appendix C how this can be done. Furthermore, the exponential has to be expanded, undoing the resummation we performed in section 4.5. After rewriting the traces and expanding the exponential up to leading order, the partition function reads

$$Z = \int [dU_4] \prod_i (1 + h_1 L_i^* + h_1^2 L_i + h_1^3)^2 \\ \times \Big[1 - 2h_2 \sum_{<i,j>} \frac{h_1 L_i + 2h_1^2 L_i^* + 3h_1^3}{1 + h_1 L_i + h_1^2 L_i^* + h_1^3} \frac{h_1 L_j + 2h_1^2 L_j^* + 3h_1^3}{1 + h_1 L_j + h_1^2 L_j^* + h_1^3}\Big] + \mathcal{O}(\kappa^4). \tag{6.12}$$

The fact that the Polyakov loops are contained in rational functions still prevents us from performing the gauge integral. This is resolved by noticing that they cancel with the respective contributions from the static determinant. This is hardly surprising, since the fractions originate from summing over all winding numbers in the temporal directions, which involved the use of the static quark propagator. Since higher orders in the hopping expansion introduce higher exponents in the denominators, relying on this cancellations is the limiting factor for the analytic solution as we proceed to solve higher orders in κ. At order κ^n, i.e. order $h_2^{n/2}$, the highest order that can appear in the denominator is $(\mathbb{1} + h_1 W)^{n/2}$. Since the exponent of the static quark determinant is $2N_f$, this gives us a limit for the order, κ^n we can solve analytically when working with N_f flavors. This

limit is

$$n \leq 4N_f. \tag{6.13}$$

That means that, staying at $N_f = 1$, we will not be able to go beyond analytically calculating the $\mathcal{O}(\kappa^4)$ corrections. At higher orders we still have the possibility to expand the fraction in eq. 6.12 in terms of h_1, but this relies on h_1 being small. Since h_1 grows exponentially with the chemical potential this is not feasible when working at high densities.

After we canceled the denominators in eq. 6.12 we can perform the gauge integration using the integrals given in the appendix B and get

$$Z = z_0^V - 6h_2 V z_0^{V-2} z_1^2, \tag{6.14}$$

where z_1 is

$$\begin{aligned} z_1 &= \int [dU_4](1 + h_1 L + h_1^2 L^* + h_1^3)^2 \ \frac{h_1 L_i + 2h_1^2 L_i^* + 3h_1^3}{1 + h_1 L_i + h_1^2 L_i^* + h_1^3} \\ &= 6h_1^3 + 3h_1^6. \end{aligned} \tag{6.15}$$

Factorizing out the static contribution we see that, to leading order, this can be written as an exponential,

$$Z = z_0^V [1 - 6h_2 V \frac{z_1^2}{z_0^2}] = z_0^V \ \exp[-6h_2 V \frac{z_1^2}{z_0^2}] + \mathcal{O}(\kappa^4). \tag{6.16}$$

The arguments for the necessity of resuming the result into an exponential are essentially the same as the ones given in section 4.5. After exponentiating, the logarithm of the partition function,

$$\frac{\ln Z}{V} = \ln z_0 - 6h_2 \frac{z_1^2}{z_0^2}, \tag{6.17}$$

has the correct volume dependence to ensure that intensive and extensive quantities scale correctly.

As an example we look at the baryon number density once more. The leading order correction to the static limit is

$$\langle a^3 n_B \rangle_{\kappa^2} = \langle a^3 n_B \rangle_0 - 216 h_2 \frac{2h_1^6 + 3h_1^9 + 3h_1^{12} + h_1^{15}}{z_0^3}, \tag{6.18}$$

with $\langle \mathcal{O} \rangle_{\kappa^0}$ $\langle \mathcal{O} \rangle_{\kappa^2}$ denoting expectation values calculated to the respective order in the hopping expansion. As can be seen the result is independent of the volume due to the

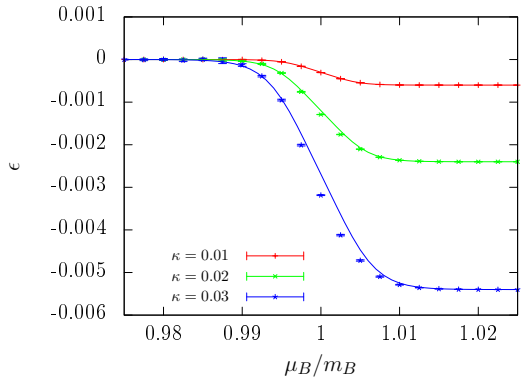

FIGURE 6.2: Binding energy for 3 different quarks masses vs chemical potential, $V = 6^3, N_\tau = 50, N_f = 1, V = 6$. Solid lines are analytical, points are numerical results.

resummation.

Fig. 6.2 shows the comparison between the analytic solution, eq. 6.18, and the numerical solution of the action, i.e. eq. 6.11, for different values of κ. As can be seen, both agree well for small κ, but start to diverge for larger values. The difference is of order κ^4. To see this we expand the nearest neighbour interaction in eq. 6.11 to the next order,

$$\begin{aligned}
&\int [dU_4] \exp(-2h_2 \sum_{<i,j>} \mathrm{Tr} \frac{h_1 W_i}{\mathbb{1} + h_1 W_i} \mathrm{Tr} \frac{h_1 W_j}{\mathbb{1} + h_1 W_j}) \\
&= 1 - 2h_2 \sum_{<i,j>} \mathrm{Tr} \frac{h_1 W_i}{\mathbb{1} + h_1 W_i} \mathrm{Tr} \frac{h_1 W_j}{\mathbb{1} + h_1 W_j} \\
&+ 2h_2^2 \sum_{<i,j>} \sum_{<k,l>} \mathrm{Tr} \frac{h_1 W_i}{\mathbb{1} + h_1 W_i} \mathrm{Tr} \frac{h_1 W_j}{\mathbb{1} + h_1 W_j} \mathrm{Tr} \frac{h_1 W_k}{\mathbb{1} + h_1 W_k} \mathrm{Tr} \frac{h_1 W_l}{\mathbb{1} + h_1 W_l} + O(\kappa^6). \qquad (6.19)
\end{aligned}$$

We solved the leading contribution in h_2 without needing any approximation. The next order contains two independent sums over nearest neighbours and is therefore quadratic in the volume. When we resummed our solution in eq. 6.16 we included all those graphs as if they were non-overlapping, i.e. proportional to z_1^2. This introduces an error that is proportional in the volume and of order κ^4, corresponding to the diagrams with overlapping sums.

Finding the exact analytic solution to the action eq. 6.11 therefore would require knowledge of an infinite number of gauge integrals. Since the effect is of order κ^4, the growing discrepancy between numerical and analytical data also signals the breakdown of the κ^2 approximation in the hopping expansion.

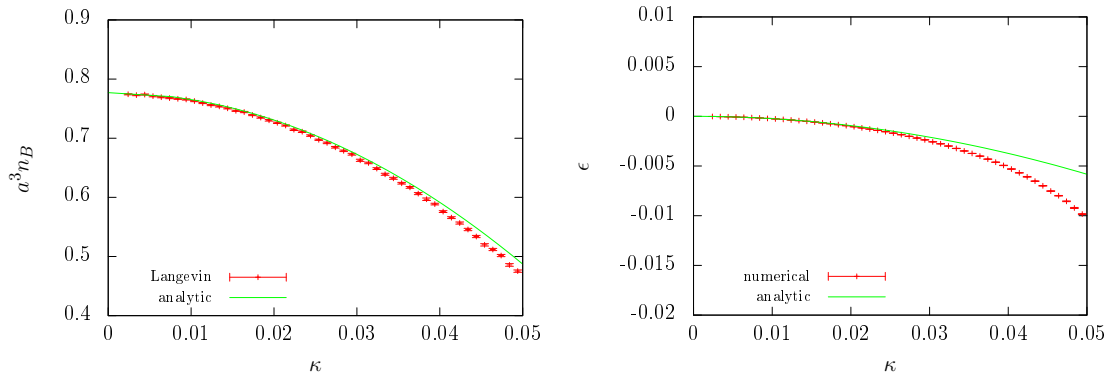

FIGURE 6.3: Left: Analytic vs numerical results for baryon number density with κ^2 action, $V = 6^3, N_\tau = 50$, $\beta = 0$, $N_f = 1$, $h_1 = 0.8$. Right: Same comparison for the nuclear binding energy.

Now we want to calculate the binding energy to leading order. For this we again need the energy density,

$$\begin{aligned} a^4 e &= -\frac{a}{N_\tau N_s^3}\frac{\partial \ln Z}{\partial a} \\ &= -\frac{a}{N_\tau N_s^3}\frac{\partial \kappa}{\partial a}\Big(\frac{\partial h_1}{\partial \kappa}\frac{\partial \ln Z}{\partial h_1} + \frac{\partial h_2}{\partial \kappa}\frac{\partial \ln Z}{\partial h_2}\Big) \\ &= \frac{a m_B}{N_\tau N_s^3}(\frac{\kappa}{3} - 2\kappa^4)\Big(\frac{N_\tau}{\kappa}N_s^3 a^3 n_q + \frac{2}{\kappa}h_2\frac{\partial \ln Z}{\partial h_2}\Big) \\ &= a m_B a^3 n_B(1 - 6k^3) - 4\frac{a m_B h_2}{N_\tau}(1 - 6\kappa^3)\frac{z_1^2}{z_0^2}. \end{aligned} \tag{6.20}$$

To get the binding energy we again subtract the rest mass contained in the system and normalize with respect to the density and the baryon mass. Keeping only leading orders in κ we get

$$\epsilon = \frac{a^4 e - n_b m_b}{n_b m_b} = -2\kappa^2\frac{z_1}{z_0} = -\frac{1}{2}\frac{z_1}{z_0}e^{-a m_\pi}. \tag{6.21}$$

In the last step we furthermore used eq. 5.10 to leading order. It shows that, to leading order, the binding energy is exponentially suppressed by the pion mass. This hints at a Yukawa type potential between the baryons, where an attractive interaction is mediated by pion exchange.

The comparison in fig. 6.3 shows that this solution reproduces the numerical results well. The increasing discrepancy between the numeric and analytic solution with larger κ is caused by the missing κ^4 contributions we already discussed.

6.1.3 κ^4 corrections

We will now proceed to present the analytic solution to the partition function including corrections up to order κ^4, i.e. the contributions shown in eq. 4.63. This is the last

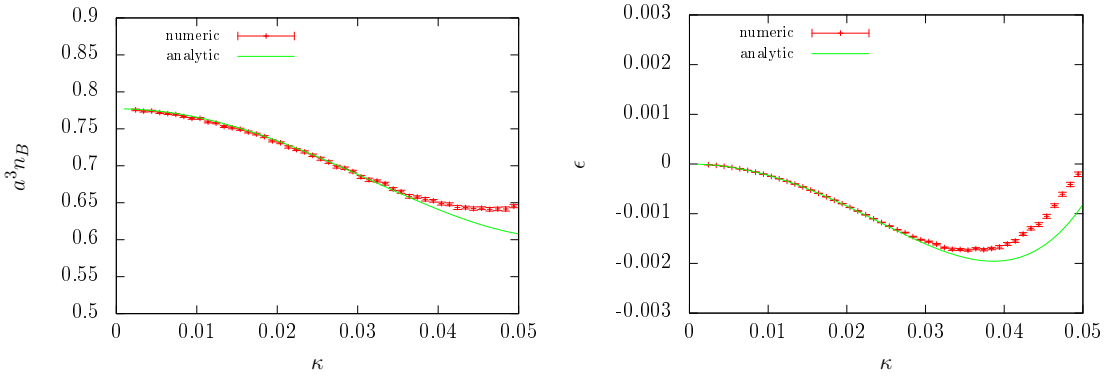

FIGURE 6.4: Left: Comparison between numeric and analytic data for baryon density vs chemical potential with the κ^4 action, $N_\tau = 50, N_f = 1, V = 6$. Solid lines show the analytic result of eq. 6.24. Right: Comparison between analytic and numerical results vs κ for the same action and $h_1 = 0.8$.

order that can be solved analytically for $N_f = 1$ because of the limit set by eq. 6.13. Repeating the steps of the previous section the partition function up to order κ^4 is

$$Z = z_0^V \exp\Big[-6Vh_2\frac{z_1^2}{z_0^2} + 30Vh_3\frac{z_1^2 z_2}{z_0^3} + 6Vh_3\frac{z_2 z_3}{z_0^2} + 6Vh_3\frac{z_2^2}{z_0^2} + 60Vh_3\frac{z_1^2 z_3}{z_0^3} + 6Vh_3\frac{z_3^2}{z_0^2} - 66Vh_3\frac{z_1^4}{z_0^4}\Big]. \tag{6.22}$$

where we again made use of the integrals in appendix B to compute

$$\begin{aligned} z_2 &= \int [dU_4](1 + h_1 L + h_1^2 L^* + h_1^3)^2 \ \frac{h_1(L + 4h_1^3 L + 4h_1 L^* + h_1^4 L^* + h_1^2(9 + LL^*))}{(1 + h_1 L + h_1^2 L^* + h_1^3)^2} \\ &= 10h_1^3, \\ z_3 &= \int [dU_4](1 + h_1 L + h_1^2 L^* + h_1^3)^2 \ \Big(\frac{h_1 L + 2h_1 L^* + 3h_1^3}{1 + h_1 L + h_1^2 L^* + h_1^3}\Big)^2 \\ &= 4h_1^3 + 9h_1^6. \end{aligned} \tag{6.23}$$

The last term of eq. 6.22 is a counterterm that corrects the order κ^4 error introduced when exponentiating the solution, see the discussion in section 6.1.2.

Calculating the baryon density we get

$$\langle a^3 n_B \rangle_{\kappa^4} = \langle a^3 n_B \rangle_{\kappa^2} + 36h_2^2\Big(52h_1^6 + 2117h_1^9 + 2990h_1^{12} + 4050h_1^{15} + 5110h_1^{18} + 3067h_1^{21} + 272h_1^{24} - 162h_1^{27}\Big)/z_0^5. \tag{6.24}$$

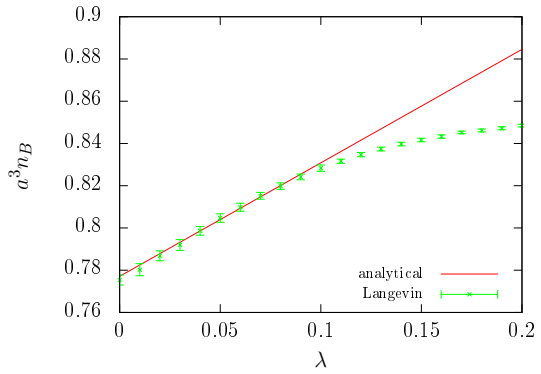

FIGURE 6.5: Comparison between simulation done with stochastic quantization and analytic result for the static quark determinant including leading λ corrections, $V = 6^3, N_\tau = 4$ $h_1 = 0.8$.

As in the κ^2 case these corrections vanish in the limits of low and high chemical potential. For the binding energy we get

$$< \epsilon >_{\kappa^4} = < \epsilon >_{\kappa^2} + h_2^2 \, \frac{12(52h_1^3 + 902h_1^6 + 1827h_1^9 + 1712h_1^{12} + 862h_1^{15} + 162h_1^{18})}{(6 + h_1^3)\, z_0^3} \tag{6.25}$$

In fig. 6.4 we show how those results compare to the numerical values. We have good agreement for small κ. The deviation for higher values of κ is again caused by the missing κ^6 contributions not included in the analytic result.

6.2 Gauge corrections

As already discussed in chapter 4, gauge corrections can be grouped into two categories. First there are contributions coming from the pure gauge action. Second we also have contributions coming from the possibilities to attach single plaquettes to fermionic graphs and vice versa, i.e. mixing terms between fermionic and gluonic contributions.

The latter are included by introducing gauge corrections to the fermionic coupling constants $h_1, h_2, ...$ and fermionic corrections to the gauge couplings $\lambda_1, \lambda_2, ...$. We already calculated those corrections in section 4.4. We can trivially incorporate them into the analytic solution by replacing the respective couplings.

What remains to be done is including the contributions from the pure gauge action. To derive those we have to include the leading contribution from section 4.2,

$$S_g = \sum_{<i,j>} \log[1 + 2\lambda_1(u(\beta), N_\tau) \mathrm{Re} L_i L_j^*]. \tag{6.26}$$

Taking $N_f = 1$ and again neglecting anti-quarks for brevity, we have

$$\begin{aligned} Z &= \int [dU_4] \prod_i (1 + h_1 L + h_1^2 L^* + h_1^3)^2 \prod_{<i,j>} (1 + 2\lambda_1 \mathrm{Re} L_i L_j^*) \\ &= z_0^V (1 + 6V\lambda_1 \frac{z_{\lambda,1} z_{\lambda,2}}{z_0^2}) \\ &= z_0^V \exp[6V\lambda_1 \frac{z_{\lambda,1} z_{\lambda,2}}{z_0^2})] + \mathcal{O}(\lambda^2), \end{aligned} \tag{6.27}$$

with the integrals

$$\begin{aligned} z_{\lambda,1} &= \int [dU_4](1 + h_1 L + h_1^2 L^* + h_1^3)^2 L = 3h_1^2 + 2h_1^5, \\ z_{\lambda,2} &= \int [dU_4](1 + h_1 L + h_1^2 L^* + h_1^3)^2 L^* = 2h_1 + 3h_1^4. \end{aligned} \tag{6.28}$$

The integrals necessary for this computation can again be found in appendix B. We exponentiated the result following the same arguments as in the case of eq. 6.16. Calculating the baryon number density for a system of static quarks, now including leading gauge corrections, gives us

$$\langle n_B \rangle_\lambda = \langle n_B \rangle_{\lambda=0} + 2\lambda_1 \frac{6h_1^3(3 + h_1^3 - h_1^9 - 3h_1^{12})}{z_0^3} + \mathcal{O}(\lambda^2). \tag{6.29}$$

As can be seen in fig. 6.5 this is a good approximation as long as $\lambda < 0.1$. This again confirms the validity of our approximation introduced in section 4.7, where we completely neglect the pure gauge contribution when $N_\tau \to \infty$. Note that the deconfinement transition already takes place at $\lambda_1 \approx 0.188$ [89], so the leading correction shown in fig. 6.5 already covers a large parameter region.

6.3 Analytic Continuum Extrapolation

Now that we have an analytic expression for the partition function up to order κ^4 including gauge corrections, it is possible to repeat the continuum extrapolation presented in the section 5.9 on a purely analytical basis. This allows us to test the validity of the analytic solution in a physically meaningful context. Using the parameters in table 5.1 we repeat the fitting procedure shown in fig. 5.9. The results in fig. 6.6 show that the results from the numerical approach and the ones derived analytically are in perfect agreement. Errors for the analytic result come from the difference between the $\mathcal{O}(\kappa^2)$ and the $\mathcal{O}(\kappa^4)$ expressions and the uncertainties due to the fitting procedure. The numerical data has an additional statistical error.

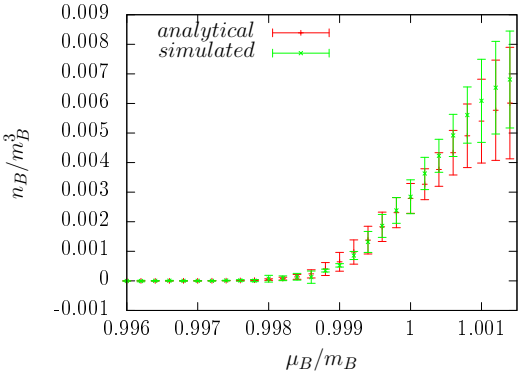

FIGURE 6.6: Comparison between the continuum extrapolated baryon density at $T = 10$MeV and a pion mass of $m_p = 20$GeV calculated using numerical simulations and analytical methods.

6.4 Resummation of higher order terms

So far we tried to reproduce the numerical results with analytic expressions. While this provides additional insight to the theory and serves as a check for the numerical results, its area of applicability is at best equal to the theory we started with. We conclude this chapter with presenting an approach to extent this by applying further resummations to the analytic results.

To demonstrate our approach we pick the following κ^2 and κ^4 contribution from the analytic κ^4 expression, see eq. 6.22,

$$Z_{\kappa^2} = z_0^V \exp\Big[-6Vh_2 \frac{z_1^2}{z_0^2} + 30Vh_3 \frac{z_1^2 z_2}{z_0^3} \Big]. \tag{6.30}$$

It will be recalled that these expressions come from the following two and three point interaction terms of the effective action, forming either a straight line or a wedge,

$$\begin{aligned} -S_{2p} &= -2N_f h_2 \sum_{\langle ij \rangle} \mathrm{Tr} \frac{h_1 W_i}{1 + h_1 W_i} \mathrm{Tr} \frac{h_1 W_k}{1 + h_1 W_k} \\ -S_{3p} &= 2N_f h_3 \sum_{\langle ijk \rangle} \mathrm{Tr} \frac{h_1 W_i}{1 + h_1 W_i} \mathrm{Tr} \frac{h_1 W_j}{(1 + h_1 W_j)^2} \mathrm{Tr} \frac{h_1 W_k}{1 + h_1 W_k}. \end{aligned} \tag{6.31}$$

Looking at higher orders one finds corresponding n-point interactions at higher orders. Those correspond to the contributions $P_i M_i$, $P_i P_j M_j M_i$, $P_i M_i P_j M_j$ and so on from eq. 4.22. If we restrict ourselves to cases where this n-point interactions form non-overlapping strings resummation is possible. This is because those diagrams do not introduce new types of gauge integrals, so each one can be recursively generated from

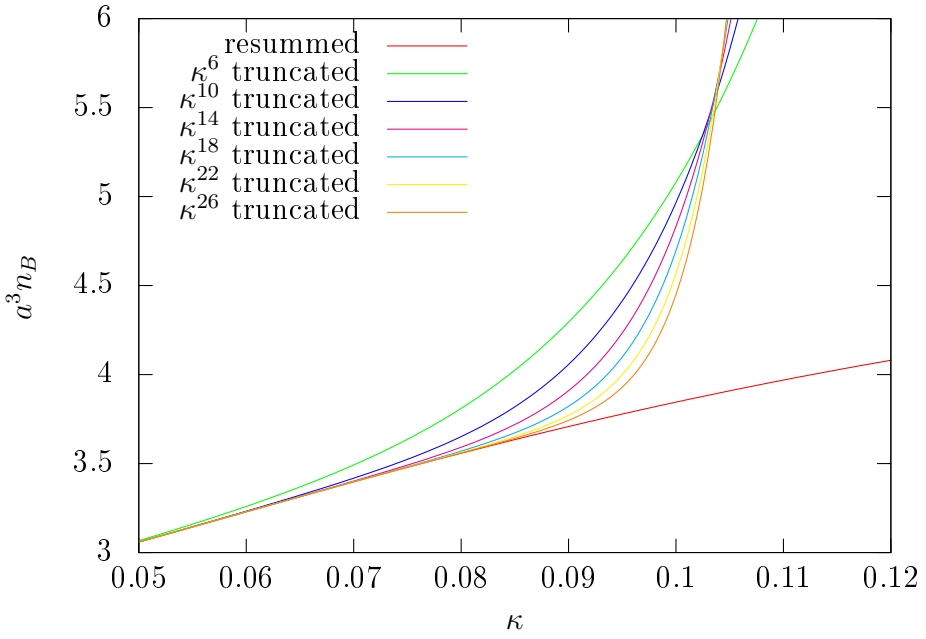

FIGURE 6.7: Comparison between the resummed κ^2 solution (red line) and its truncation at various orders. The point where the series expansion breaks down is $\kappa = 0.1095$, Parameters are $h_1 = 0.8, N_\tau = 50, N_f = 3$.

the previous term. The first terms of this subclass of diagrams gives the contribution

$$Z_{\kappa^2} = z_0^V \exp\Big[-6Vh_2\frac{z_1^2}{z_0^2} + 30Vh_2^2\frac{z_1^2 z_2}{z_0^3} - 150Vh_2^3\frac{z_1^2 z_2^2}{z_0^4} + 726Vh_2^4\frac{z_1^2 z_2^3}{z_0^5} - 3534Vh_2^5\frac{z_1^2 z_2^4}{z_0^6} + O(\kappa^{12})\Big]. \tag{6.32}$$

Here we used the fact that in the strong coupling limit $h_3 = h_2^2$, $h_4 = h_2^3$ and so on. The crucial observation is the fact that we can sum this up as a geometric series,

$$\begin{aligned} Z_{\kappa^2} &= z_0^V \exp\Big[6Vz_1^2\sum_{n=1}^{\infty}(-5)^{n-1}h_2^n\frac{z_2^{n-1}}{z_0^{n+2}}\Big] \\ &= \frac{6h_2 z_1^2}{z_0(z_0+5h_2 z_2)}. \end{aligned} \tag{6.33}$$

As can be seen from eq. 6.32 the factor of five is an approximation. For higher order graphs the number will be slightly lower since graphs that involve overlapping contributions have to be subtracted. This can be done order by order when resumming higher order graphs.

Note that this kind of resummation is not possible before the gauge integrals over the temporal links were performed. In our original effective action, eq. 6.31, every new order introduces a new sum over spatial positions that has to be performed explicitly.

In fig. 6.7 we truncated eq. 6.33 at different orders in κ and compared it to the

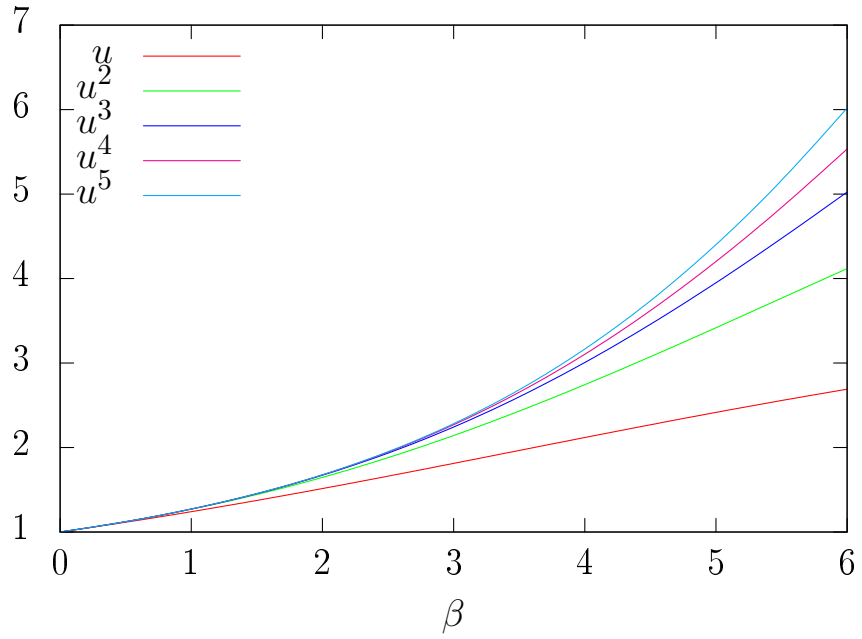

FIGURE 6.8: Coupling constant $h_3(\beta)/h_3(\beta = 0)$ truncated at different orders in u and plotted against the gauge coupling β.

untruncated expression. Note that the order in κ here refers to the diagram subclass we are looking at, not the full quark determinant. As can be seen the expansion breaks down at $\kappa \approx 0.1095$. The resummed expression in contrast seems to significantly extend the convergence region.

It is also possible to introduce gauge corrections for the higher order terms. Those are different for each order, so we denote h_n to be the coupling constant for order $\kappa^{2(n-1)}$, with $n \geq 2$. Leading orders from the possibilities to attach gauge plaquettes between nearest neighbour Polyakov loops. This happens in the same way as in the case of h_{3_1}, see fig. 4.3, but now with the possibility to attach the first plaquette at n different positions. At higher orders we again have the possibility to attach a cube build out of five gauge plaquettes. In general we have, at order κ^{2n}, the gauge corrections

$$h_{n+1}(u) = h_{n+1}(u=0)\left[\left(1+\frac{2u}{1-u}\right)^n + 8nu^5\right]. \tag{6.34}$$

These corrections can easily be introduced by replacing h_2^n by h_{n+1} in eq. 6.33. Fig. 6.8 shows h_3, i.e. the coupling for κ^8 terms, truncated at different values of u. While the convergence is good, it gets worse as we increase n. This gets mitigated by the fact that higher order terms have a smaller overall impact on the result. Note that, as long as we are in the heavy dense limit, the corrections given in eq. 6.34 apply for all types of diagrams, not only the subclass summed up in eq. 6.33.

Chapter 7

Conclusions and Outlook

In this thesis we presented the derivation as well as the numerical and analytical treatment of an effective theory for lattice Quantum Chromodynamics (LQCD). We derived the effective theory directly from LQCD, which allows us to systematically introduce further improvements. The derivation was performed by means of an expansion around the limit of infinite quark masses and infinite gauge coupling. Using this theory we were able to derive results in the region of large densities. This region is, due to the sign problem, inaccessible to standard LQCD approaches. Although LQCD simulations at large densities have been performed recently by applying stochastic quantization [61], those are still limited to lattice with low numbers of timeslices and therefor can not reach the low temperature region. Furthermore, they can not be crosschecked with Monte-Carlo simulations. Since the equivalence between stochastic quantization and Monte-Carlo is unproven for the case of finite density systems, new approaches to access the cold dense region of the QCD phase diagram are desirable. The effective theory presented in this thesis provides such an approach.

We introduced continuum QCD in chapter 2. In chapter 3 we presented how LQCD, i.e. QCD in a discretized space-time, can be formulated and used as a tool to explore the non-perturbative regions of the QCD phase diagram. Special emphasis was placed on simulations at finite baryon densities and the numerical problems that arise in this region. These problems are caused by the complexification of the action and are known as the sign problem.

We gave a detailed presentation of the derivation of our effective theory in chapter 4. For this we performed expansions around the limit of strong coupling and static quarks, $\kappa = \beta = 0$, introducing corrections order by order in the expansion parameters κ and β. Truncating the theory at different orders allowed us to determine the parameter region where the convergence to full LQCD is good. As we showed in section 4.4, the gauge corrections are sufficient to reach $\beta \approx 6$, which translates to lattice spacings down to $a \approx 0.1$fm. In section 5.6.1 we determined the convergence in κ by simulating the

action truncated at different orders. Due to the three dimensional nature of our theory the convergence depends on the temporal extent N_τ. We concluded that our theory converges well up to values of at least $\frac{N_\tau \kappa^2}{3} \approx 0.04$. Both results can be improved by deriving further corrections.

In chapter 5 we presented the numerical treatment of our theory. While the sign problem is still present, it is mild compared to the case of full LQCD. This allowed us to use both Monte-Carlo with reweighting and stochastic quantization in order to crosscheck results. This confirms the validity of stochastic quantization for our theory, which is our method of choice since, in contrast to reweighting, it is not limited to small lattice volumes. We presented results for two parameter regions, the region of large density and low temperatures, and the region of high temperature and low density.

For the cold dense region we calculated several thermodynamical quantities and performed continuum extrapolations. This allows us to make a connection to continuum QCD, although in a parameter region far away from the physical point. The results show the onset from the vacuum to the region of finite density, displaying Silver Blaze behavior. We furthermore demonstrated the existence of a finite binding energy between baryonic states, which in the continuum are responsible for the formation of nuclear matter. Although experiments show the transition from the vacuum to the region of finite density to be of first order for low enough temperatures, the convergence region of our theory is not large enough to reproduce this. Nevertheless, we where able to find signals for a change from a crossover to a true phase transition when we left this region. This demonstrates that our theory is in principle able to reproduce the qualitative features of cold and dense nuclear matter.

In the region of high temperatures and low densities, we investigated the chiral condensate and the nature of the critical endpoint of the Roberge-Weiss transition. In both cases LQCD calculations exist for comparison. While the behaviour of the chiral condensate can be modeled quantitatively, the second tricritical Roberge-Weiss endpoint located in [19] is absent in our theory. We discussed possible reasons for this, but can not offer a final conclusion so far.

Chapter 6 demonstrated how, in the cold dense region, our effective theory can be solved analytically. We used this to accurately reproduce the numerical results from chapter 5. We furthermore derived analytic expressions for different thermodynamical observables, demonstrating how to leading order the binding energy can be described by a Yukawa potential. We finally showed how the analytic results can be resummed, potentially extending their range of validity beyond the range of the original effective theory.

Future research perspectives lie in the possibility to systematically improve the theory. Using the methods described in chapter 4, higher orders can be derived in order to extend the convergence region. This is much simplified in the limit of low temperature and high

density presented in chapter 4, which simultaneously is the most interesting parameter region due to the lack of LQCD simulations. Together with the resummation scheme from chapter 6 it should be possible to extend the theory far beyond the parameter range presented here. This will allow for better continuum extrapolations and the use of lighter quarks. Simultaneously the use of lighter quarks will mean that it is no longer possible to use the pure gauge beta function in order to set the scale, so those will have to come from LQCD simulations including fermions.

Appendix A

Effective Action to Order κ^4

In this appendix we list the full action of our effective theory including corrections up to order κ^4. Parts of this action were already published in [92]. Here we additionally include the interactions from section 4.4.2, which were neglected in [92] since they are of higher order in β. We use this action, including the gauge action shown in section 4.2, for the simulations presented in section 5.7. For the simulations in the cold and dense region, section 5.6, we use the simplified version shown in section 4.7.

In order to implement the terms shown here one can either use the reformulation in terms of Polyakov Loops, cf. appendix C, or use the fact that all matrices are diagonalized, cf. eq. 5.3, which makes the matrix divisions contained in the action trivial.

In the derivation of eq. A.2 and eq. A.3 fourfold occupied spatial links are encountered, so besides the integration rules in eq. 4.36 we also need the integral over four gauge links [99],

$$\begin{aligned}\int dU U_{i_1 j_1} U_{i_2 j_2} U^\dagger_{k_1 l_1} U^\dagger_{k_2 l_2} =& \frac{1}{N_c^2-1}\Big[\delta_{i_1 l_1}\delta_{i_2 l_2}\delta_{j_1 k_1}\delta_{j_2 k_2} + \delta_{i_1 l_2}\delta_{i_2 l_1}\delta_{j_1 k_2}\delta_{j_2 k_1}\Big] \\ & - \frac{1}{N_c(N_c^2-1)}\Big[\delta_{i_1 l_2}\delta_{i_2 l_1}\delta_{j_1 k_1}\delta_{j_2 k_2} + \delta_{i_1 l_1}\delta_{i_2 l_2}\delta_{j_1 k_2}\delta_{j_2 k_1}\Big]. \quad \text{(A.1)}\end{aligned}$$

The full $\mathcal{O}(\kappa^4)$ contributions reads:

$$-\frac{1}{2}\int[dU_k]\sum_{\vec{x},i}\mathrm{Tr}P_{\vec{x},i}M_{\vec{x},i}P_{\vec{x},i}M_{\vec{x},i}= \tag{A.2}$$

$$\begin{aligned}
&\frac{\kappa^4 N_\tau(N_\tau-1)}{N_c^2}\sum_{\vec{x},i}\Big\{\mathrm{Tr}\Big(\frac{h_1W_{\vec{x}}}{(\mathbb{1}+h_1W_{\vec{x}})^2}+\frac{\bar{h}_1W^\dagger_{\vec{x}}}{(\mathbb{1}+\bar{h}_1W^\dagger_{\vec{x}})^2}+2\frac{\frac{\mathbb{1}}{N_\tau-1}\sum_{t=1}^{N_\tau-1}(2\kappa)^{2t}}{(\mathbb{1}+h_1W_{\vec{x}})(\mathbb{1}+\bar{h}_1W^\dagger_{\vec{x}})}\Big)\\
&\qquad\Big(\mathrm{Tr}\frac{h_1W_{\vec{x}+i}}{\mathbb{1}+h_1W_{\vec{x}+i}}-\mathrm{Tr}\frac{\bar{h}_1W^\dagger_{\vec{x}+i}}{\mathbb{1}+\bar{h}_1W^\dagger_{\vec{x}+i}}\Big)^2+\Big(\mathrm{Tr}\frac{h_1W_{\vec{x}}}{\mathbb{1}+h_1W_{\vec{x}}}-\mathrm{Tr}\frac{\bar{h}_1W^\dagger_{\vec{x}}}{\mathbb{1}+\bar{h}_1W^\dagger_{\vec{x}}}\Big)^2\\
&\qquad\mathrm{Tr}\Big(\frac{h_1W_{\vec{x}+i}}{(\mathbb{1}+h_1W_{\vec{x}+i})^2}+\frac{\bar{h}_1W^\dagger_{\vec{x}+i}}{(\mathbb{1}+\bar{h}_1W^\dagger_{\vec{x}+i})^2}+2\frac{\frac{\mathbb{1}}{N_\tau-1}\sum_{t=1}^{N_\tau-1}(2\kappa)^{2t}}{(\mathbb{1}+h_1W_{\vec{x}+i})(\mathbb{1}+\bar{h}_1W^\dagger_{\vec{x}+i})}\Big)\Big\}\\
&-\frac{\kappa^4 N_\tau}{N_c^2-1}\sum_{\vec{x},i}\Big\{\mathrm{Tr}\Big(\frac{h_1W_{\vec{x}}}{\mathbb{1}+h_1W_{\vec{x}}}-\frac{\bar{h}_1W^\dagger_{\vec{x}}}{\mathbb{1}+\bar{h}_1W^\dagger_{\vec{x}}}\Big)^2\Big(\mathrm{Tr}\frac{h_1W_{\vec{x}+i}}{\mathbb{1}+h_1W_{\vec{x}+i}}-\mathrm{Tr}\frac{\bar{h}_1W^\dagger_{\vec{x}+i}}{\mathbb{1}+\bar{h}_1W^\dagger_{\vec{x}+i}}\Big)^2\\
&\qquad+\Big(\mathrm{Tr}\frac{h_1W_{\vec{x}}}{\mathbb{1}+h_1W_{\vec{x}}}-\mathrm{Tr}\frac{\bar{h}_1W^\dagger_{\vec{x}}}{\mathbb{1}+\bar{h}_1W^\dagger_{\vec{x}}}\Big)^2\mathrm{Tr}\Big(\frac{h_1W_{\vec{x}+i}}{\mathbb{1}+h_1W_{\vec{x}+i}}-\frac{\bar{h}_1W^\dagger_{\vec{x}+i}}{\mathbb{1}+\bar{h}_1W^\dagger_{\vec{x}+i}}\Big)^2\Big\}\\
&+\frac{\kappa^4 N_\tau}{N_c^3-N_c}\sum_{\vec{x},i}\Big\{\mathrm{Tr}\Big(\frac{h_1W_{\vec{x}}}{\mathbb{1}+h_1W_{\vec{x}}}-\frac{\bar{h}_1W^\dagger_{\vec{x}}}{\mathbb{1}+\bar{h}_1W^\dagger_{\vec{x}}}\Big)^2\mathrm{Tr}\Big(\frac{h_1W_{\vec{x}+i}}{\mathbb{1}+h_1W_{\vec{x}+i}}-\frac{\bar{h}_1W^\dagger_{\vec{x}+i}}{\mathbb{1}+\bar{h}_1W^\dagger_{\vec{x}+i}}\Big)^2\\
&\qquad+\Big(\mathrm{Tr}\frac{h_1W_{\vec{x}}}{\mathbb{1}+h_1W_{\vec{x}}}-\mathrm{Tr}\frac{\bar{h}_1W^\dagger_{\vec{x}}}{\mathbb{1}+\bar{h}_1W^\dagger_{\vec{x}}}\Big)^2\Big(\mathrm{Tr}\frac{h_1W_{\vec{x}+i}}{\mathbb{1}+h_1W_{\vec{x}+i}}-\mathrm{Tr}\frac{\bar{h}_1W^\dagger_{\vec{x}+i}}{\mathbb{1}+\bar{h}_1W^\dagger_{\vec{x}+i}}\Big)^2\Big\}
\end{aligned}$$

$$\frac{1}{2}\int [dU_k]\sum_{\vec{x},i}\mathrm{Tr}P_{\vec{x},i}M_{\vec{x},i}\mathrm{Tr}P_{\vec{x},i}M_{\vec{x},i} = \tag{A.3}$$

$$2\frac{\kappa^4 N_\tau(N_\tau-1)}{N_c^2}\sum_{\vec{x},i}\Big\{\Big(\mathrm{Tr}\frac{h_1W_{\vec{x}}}{\mathbb{1}+h_1W_{\vec{x}}}-\mathrm{Tr}\frac{\bar{h}_1W^\dagger_{\vec{x}}}{\mathbb{1}+\bar{h}_1W^\dagger_{\vec{x}}}\Big)^2\Big(\mathrm{Tr}\frac{h_1W_{\vec{x}+i}}{\mathbb{1}+h_1W_{\vec{x}+i}}-\mathrm{Tr}\frac{\bar{h}_1W^\dagger_{\vec{x}+i}}{\mathbb{1}+\bar{h}_1W^\dagger_{\vec{x}+i}}\Big)^2$$
$$+\mathrm{Tr}\Big(\frac{h_1W_{\vec{x}}}{(\mathbb{1}+h_1W_{\vec{x}})^2}+\frac{\bar{h}_1W^\dagger_{\vec{x}}}{(\mathbb{1}+\bar{h}_1W^\dagger_{\vec{x}})^2}\Big)\mathrm{Tr}\Big(\frac{h_1W_{\vec{x}+i}}{(\mathbb{1}+h_1W_{\vec{x}+i})^2}+\frac{\bar{h}_1W^\dagger_{\vec{x}+i}}{(\mathbb{1}+\bar{h}_1W^\dagger_{\vec{x}+i})^2}\Big)$$
$$+4\mathrm{Tr}\Big(\frac{h_1W_{\vec{x}}}{(\mathbb{1}+h_1W_{\vec{x}})^2}+\frac{\bar{h}_1W^\dagger_{\vec{x}}}{(\mathbb{1}+\bar{h}_1W^\dagger_{\vec{x}})^2}\Big)\mathrm{Tr}\frac{\frac{1}{N_\tau-1}\sum_{t=1}^{N_\tau-1}(2\mathbb{1}\kappa)^{2t}}{(\mathbb{1}+h_1W_{\vec{x}+i})(\mathbb{1}+\bar{h}_1W^\dagger_{\vec{x}+i})}$$
$$+4\mathrm{Tr}\frac{\frac{1}{N_\tau-1}\sum_{t=1}^{N_\tau-1}(2\kappa)^{2t}}{(\mathbb{1}+h_1W_{\vec{x}})(\mathbb{1}+\bar{h}_1W^\dagger_{\vec{x}})}\mathrm{Tr}\Big(\frac{h_1W_{\vec{x}+i}}{(\mathbb{1}+h_1W_{\vec{x}+i})^2}+\frac{\bar{h}_1W^\dagger_{\vec{x}+i}}{(\mathbb{1}+\bar{h}_1W^\dagger_{\vec{x}+i})^2}\Big)$$
$$+4\frac{1}{N_\tau-1}\sum_{t=1}^{N_\tau-1}(2\kappa)^{4t}\mathrm{Tr}\frac{\mathbb{1}}{(\mathbb{1}+h_1W_{\vec{x}})(\mathbb{1}+\bar{h}_1W^\dagger_{\vec{x}})}\mathrm{Tr}\frac{\mathbb{1}}{(\mathbb{1}+h_1W_{\vec{x}+i})(\mathbb{1}+\bar{h}_1W^\dagger_{\vec{x}+i})}$$
$$+4(2\kappa)^{2N_\tau}\mathrm{Tr}\frac{\mathbb{1}}{(\mathbb{1}+h_1W_{\vec{x}})(\mathbb{1}+\bar{h}_1W^\dagger_{\vec{x}})}\mathrm{Tr}\frac{\mathbb{1}}{(\mathbb{1}+h_1W_{\vec{x}+i})(\mathbb{1}+\bar{h}_1W^\dagger_{\vec{x}+i})}\Big\}$$
$$+2\frac{\kappa^4 N_\tau}{N_c^2-1}\sum_{\vec{x},i}\Big\{\Big(\mathrm{Tr}\frac{h_1W_{\vec{x}}}{\mathbb{1}+h_1W_{\vec{x}}}-\mathrm{Tr}\frac{\bar{h}_1W^\dagger_{\vec{x}}}{\mathbb{1}+\bar{h}_1W^\dagger_{\vec{x}}}\Big)^2\Big(\mathrm{Tr}\frac{h_1W_{\vec{x}+i}}{\mathbb{1}+h_1W_{\vec{x}+i}}-\mathrm{Tr}\frac{\bar{h}_1W^\dagger_{\vec{x}+i}}{\mathbb{1}+\bar{h}_1W^\dagger_{\vec{x}+i}}\Big)^2$$
$$+\mathrm{Tr}\Big(\frac{h_1W_{\vec{x}}}{\mathbb{1}+h_1W_{\vec{x}}}-\frac{\bar{h}_1W^\dagger_{\vec{x}}}{\mathbb{1}+\bar{h}_1W^\dagger_{\vec{x}}}\Big)^2\mathrm{Tr}\Big(\frac{h_1W_{\vec{x}+i}}{\mathbb{1}+h_1W_{\vec{x}+i}}-\frac{\bar{h}_1W^\dagger_{\vec{x}+i}}{\mathbb{1}+\bar{h}_1W^\dagger_{\vec{x}+i}}\Big)^2\Big\}$$
$$-2\frac{\kappa^4 N_\tau}{N_c^3-N_c}\sum_{\vec{x},i}\Big\{\mathrm{Tr}\Big(\frac{h_1W_{\vec{x}}}{\mathbb{1}+h_1W_{\vec{x}}}-\frac{\bar{h}_1W^\dagger_{\vec{x}}}{\mathbb{1}+\bar{h}_1W^\dagger_{\vec{x}}}\Big)^2\Big(\mathrm{Tr}\frac{h_1W_{\vec{x}+i}}{\mathbb{1}+h_1W_{\vec{x}+i}}-\mathrm{Tr}\frac{\bar{h}_1W^\dagger_{\vec{x}+i}}{\mathbb{1}+\bar{h}_1W^\dagger_{\vec{x}+i}}\Big)^2$$
$$+\Big(\mathrm{Tr}\frac{h_1W_{\vec{x}}}{\mathbb{1}+h_1W_{\vec{x}}}-\mathrm{Tr}\frac{\bar{h}_1W^\dagger_{\vec{x}}}{\mathbb{1}+\bar{h}_1W^\dagger_{\vec{x}}}\Big)^2\mathrm{Tr}\Big(\frac{h_1W_{\vec{x}+i}}{\mathbb{1}+h_1W_{\vec{x}+i}}-\frac{\bar{h}_1W^\dagger_{\vec{x}+i}}{\mathbb{1}+\bar{h}_1W^\dagger_{\vec{x}+i}}\Big)^2\Big\}$$

$$-\int [dU_k] \sum_{\vec{x},i} \mathrm{Tr} P_{\vec{x},i} P_{\vec{x},i} M_{\vec{x},i} M_{\vec{x},i} = \tag{A.4}$$

$$2\frac{\kappa^4 N_\tau (N_\tau - 1)}{N_c^2} \sum_{\vec{x},i} \mathrm{Tr}\Big(\frac{h_1 W_{\vec{x}-i}}{\mathbb{1} + h_1 W_{\vec{x}-i}} - \frac{\bar{h}_1 W^\dagger_{\vec{x}-i}}{\mathbb{1} + \bar{h}_1 W^\dagger_{\vec{x}-i}}\Big)$$
$$\mathrm{Tr}\Big(\frac{h_1 W_{\vec{x}}}{(\mathbb{1} + h_1 W_{\vec{x}})^2} + \frac{\bar{h}_1 W^\dagger_{\vec{x}}}{(\mathbb{1} + \bar{h}_1 W^\dagger_{\vec{x}})^2} - 2\frac{\frac{1}{N_\tau - 1}\sum_{t=1}^{N_\tau - 1}(2\kappa)^{2t}}{(\mathbb{1} + h_1 W_{\vec{x}})(\mathbb{1} + \bar{h}_1 W^\dagger_{\vec{x}})}\Big)$$
$$\mathrm{Tr}\Big(\frac{h_1 W_{\vec{x}+i}}{\mathbb{1} + h_1 W_{\vec{x}+i}} - \frac{\bar{h}_1 W^\dagger_{\vec{x}+i}}{\mathbb{1} + \bar{h}_1 W^\dagger_{\vec{x}+i}}\Big)$$
$$-2\frac{\kappa^4 N_\tau}{N_c^2} \sum_{\vec{x},i} \Big\{ \mathrm{Tr}\Big(\frac{h_1 W_{\vec{x}-i}}{\mathbb{1} + h_1 W_{\vec{x}-i}} - \frac{\bar{h}_1 W^\dagger_{\vec{x}-i}}{\mathbb{1} + \bar{h}_1 W^\dagger_{\vec{x}-i}}\Big) \mathrm{Tr}\Big(1 - \frac{h_1 W_{\vec{x}}}{\mathbb{1} + h_1 W_{\vec{x}}} + 1 - \frac{\bar{h}_1 W^\dagger_{\vec{x}}}{\mathbb{1} + \bar{h}_1 W^\dagger_{\vec{x}}}\Big)^2$$
$$\mathrm{Tr}\Big(\frac{h_1 W_{\vec{x}+i}}{\mathbb{1} + h_1 W_{\vec{x}+i}} - \frac{\bar{h}_1 W^\dagger_{\vec{x}+i}}{\mathbb{1} + \bar{h}_1 W^\dagger_{\vec{x}+i}}\Big)\Big\}$$

$$-\int [dU_k] \sum_{\vec{x},i\neq j} \mathrm{Tr} P_{\vec{x},i} M_{\vec{x},j} P_{\vec{x},j} M_{\vec{x},i} = \tag{A.5}$$
$$2\frac{\kappa^4 N_\tau (N_\tau - 1)}{N_c^2} \sum_{\vec{x},i\neq j} \mathrm{Tr}\Big(\frac{h_1 W_{\vec{x}-i}}{\mathbb{1} + h_1 W_{\vec{x}-i}} - \frac{\bar{h}_1 W^\dagger_{\vec{x}-i}}{\mathbb{1} + \bar{h}_1 W^\dagger_{\vec{x}-i}}\Big)$$
$$\mathrm{Tr}\Big(\frac{h_1 W_{\vec{x}}}{(\mathbb{1} + h_1 W_{\vec{x}})^2} + \frac{\bar{h}_1 W^\dagger_{\vec{x}}}{(\mathbb{1} + \bar{h}_1 W^\dagger_{\vec{x}})^2}\Big) \mathrm{Tr}\Big(\frac{h_1 W_{\vec{x}+j}}{\mathbb{1} + h_1 W_{\vec{x}+j}} - \frac{\bar{h}_1 W^\dagger_{\vec{x}+j}}{\mathbb{1} + \bar{h}_1 W^\dagger_{\vec{x}+j}}\Big)$$
$$-\frac{\kappa^4 N_\tau}{N_c^2} \sum_{\vec{x},i\neq j} \Big\{ \mathrm{Tr}\Big(\frac{h_1 W_{\vec{x}-i}}{\mathbb{1} + h_1 W_{\vec{x}-i}} - \frac{\bar{h}_1 W^\dagger_{\vec{x}-i}}{\mathbb{1} + \bar{h}_1 W^\dagger_{\vec{x}-i}}\Big)$$
$$\mathrm{Tr}\Big[\Big(1 - \frac{h_1 W_{\vec{x}}}{\mathbb{1} + h_1 W_{\vec{x}}} + 1 - \frac{\bar{h}_1 W^\dagger_{\vec{x}}}{\mathbb{1} + \bar{h}_1 W^\dagger_{\vec{x}}}\Big)^2 + \Big(\frac{h_1 W_{\vec{x}}}{\mathbb{1} + h_1 W_{\vec{x}}} - \frac{\bar{h}_1 W^\dagger_{\vec{x}}}{\mathbb{1} + \bar{h}_1 W^\dagger_{\vec{x}}}\Big)^2\Big]$$
$$\mathrm{Tr}\Big(\frac{h_1 W_{\vec{x}+j}}{\mathbb{1} + h_1 W_{\vec{x}+j}} - \frac{\bar{h}_1 W^\dagger_{\vec{x}+j}}{\mathbb{1} + \bar{h}_1 W^\dagger_{\vec{x}+j}}\Big)\Big\}$$

The $\mathrm{Tr}P_i M_i P_j M_j$ and $\mathrm{Tr}P_i M_j P_j M_i$ contributions are the same, just with different directions and a factor of $\frac{1}{2}$ in front. We therefore do not show them.

$$\frac{1}{2}\int [dU_k] \sum_{\vec{x},i,j} \mathrm{Tr} P_{\vec{x},i} M_{\vec{x},i} \mathrm{Tr} P_{\vec{y},j} M_{\vec{y},j} = \tag{A.6}$$
$$2\frac{\kappa^4 N_\tau^2}{N_c^2} \sum_{\vec{x},i,j} \Big(\mathrm{Tr}\frac{h_1 W_{\vec{x}}}{\mathbb{1} + h_1 W_{\vec{x}}} - \mathrm{Tr}\frac{\bar{h}_1 W^\dagger_{\vec{x}}}{\mathbb{1} + \bar{h}_1 W^\dagger_{\vec{x}}}\Big)^2$$
$$\mathrm{Tr}\Big(\frac{h_1 W_{\vec{x}+i}}{\mathbb{1} + h_1 W_{\vec{x}+i}} - \frac{\bar{h}_1 W^\dagger_{\vec{x}+i}}{\mathbb{1} + \bar{h}_1 W^\dagger_{\vec{x}+i}}\Big) \mathrm{Tr}\Big(\frac{h_1 W_{\vec{x}+j}}{\mathbb{1} + h_1 W_{\vec{x}+j}} - \frac{\bar{h}_1 W^\dagger_{\vec{x}+j}}{\mathbb{1} + \bar{h}_1 W^\dagger_{\vec{x}+j}}\Big)$$

$$
\begin{aligned}
-\int [dU_k] \sum_{i\neq j} \mathrm{Tr} P_i P_j M_i M_j = \frac{1}{2}\frac{\kappa^4 u N_\tau}{N_c^3} \sum_{\vec{x},i\neq j} \Big[\qquad (A.7)\\
\mathrm{Tr}\Big(\mathbb{1} - \frac{h_1 W_{\vec{x}}}{\mathbb{1}+h_1 W_{\vec{x}}} + \mathbb{1} - \frac{h_1 W^\dagger_{\vec{x}}}{\mathbb{1}+h_1 W^\dagger_{\vec{x}}}\Big)\mathrm{Tr}\Big(\mathbb{1} - \frac{h_1 W_{\vec{x}+i}}{\mathbb{1}+h_1 W_{\vec{x}+i}} + \mathbb{1} - \frac{h_1 W^\dagger_{\vec{x}+i}}{\mathbb{1}+h_1 W^\dagger_{\vec{x}+i}}\Big)\\
\mathrm{Tr}\Big(\mathbb{1} - \frac{h_1 W_{\vec{x}+i+j}}{\mathbb{1}+h_1 W_{\vec{x}+i+j}} + \mathbb{1} - \frac{h_1 W^\dagger_{\vec{x}+i+j}}{\mathbb{1}+h_1 W^\dagger_{\vec{x}+i+j}}\Big)\mathrm{Tr}\Big(\mathbb{1} - \frac{h_1 W_{\vec{x}+j}}{\mathbb{1}+h_1 W_{\vec{x}+j}} + \mathbb{1} - \frac{h_1 W^\dagger_{\vec{x}+j}}{\mathbb{1}+h_1 W^\dagger_{\vec{x}+j}}\Big)\\
\mathrm{Tr}\Big(\frac{h_1 W_{\vec{x}}}{\mathbb{1}+h_1 W_{\vec{x}}} + \frac{h_1 W^\dagger_{\vec{x}}}{\mathbb{1}+h_1 W^\dagger_{\vec{x}}}\Big)\mathrm{Tr}\Big(\frac{h_1 W_{\vec{x}+i}}{\mathbb{1}+h_1 W_{\vec{x}+i}} + \frac{h_1 W^\dagger_{\vec{x}+i}}{\mathbb{1}+h_1 W^\dagger_{\vec{x}+i}}\Big)\\
\mathrm{Tr}\Big(\mathbb{1} - \frac{h_1 W_{\vec{x}+i+j}}{\mathbb{1}+h_1 W_{\vec{x}+i+j}} + \mathbb{1} - \frac{h_1 W^\dagger_{\vec{x}+i+j}}{\mathbb{1}+h_1 W^\dagger_{\vec{x}+i+j}}\Big)\mathrm{Tr}\Big(\mathbb{1} - \frac{h_1 W_{\vec{x}+j}}{\mathbb{1}+h_1 W_{\vec{x}+j}} + \mathbb{1} - \frac{h_1 W^\dagger_{\vec{x}+j}}{\mathbb{1}+h_1 W^\dagger_{\vec{x}+j}}\Big)\\
\mathrm{Tr}\Big(\frac{h_1 W_{\vec{x}}}{\mathbb{1}+h_1 W_{\vec{x}}} + \frac{h_1 W^\dagger_{\vec{x}}}{\mathbb{1}+h_1 W^\dagger_{\vec{x}}}\Big)\mathrm{Tr}\Big(\mathbb{1} - \frac{h_1 W_{\vec{x}+i}}{\mathbb{1}+h_1 W_{\vec{x}+i}} + \mathbb{1} - \frac{h_1 W^\dagger_{\vec{x}+i}}{\mathbb{1}+h_1 W^\dagger_{\vec{x}+i}}\Big)\\
\mathrm{Tr}\Big(\frac{h_1 W_{\vec{x}+i+j}}{\mathbb{1}+h_1 W_{\vec{x}+i+j}} + \frac{h_1 W^\dagger_{\vec{x}+i+j}}{\mathbb{1}+h_1 W^\dagger_{\vec{x}+i+j}}\Big)\mathrm{Tr}\Big(\mathbb{1} - \frac{h_1 W_{\vec{x}+j}}{\mathbb{1}+h_1 W_{\vec{x}+j}} + \mathbb{1} - \frac{h_1 W^\dagger_{\vec{x}+j}}{\mathbb{1}+h_1 W^\dagger_{\vec{x}+j}}\Big)\\
\mathrm{Tr}\Big(\mathbb{1} - \frac{h_1 W_{\vec{x}}}{\mathbb{1}+h_1 W_{\vec{x}}} + \mathbb{1} - \frac{h_1 W^\dagger_{\vec{x}}}{\mathbb{1}+h_1 W^\dagger_{\vec{x}}}\Big)\mathrm{Tr}\Big(\frac{h_1 W_{\vec{x}+i}}{\mathbb{1}+h_1 W_{\vec{x}+i}} + \frac{h_1 W^\dagger_{\vec{x}+i}}{\mathbb{1}+h_1 W^\dagger_{\vec{x}+i}}\Big)\\
\mathrm{Tr}\Big(\frac{h_1 W_{\vec{x}+i+j}}{\mathbb{1}+h_1 W_{\vec{x}+i+j}} + \frac{h_1 W^\dagger_{\vec{x}+i+j}}{\mathbb{1}+h_1 W^\dagger_{\vec{x}+i+j}}\Big)\mathrm{Tr}\Big(\mathbb{1} - \frac{h_1 W_{\vec{x}+j}}{\mathbb{1}+h_1 W_{\vec{x}+j}} + \mathbb{1} - \frac{h_1 W^\dagger_{\vec{x}+j}}{\mathbb{1}+h_1 W^\dagger_{\vec{x}+j}}\Big)\\
\mathrm{Tr}\Big(\mathbb{1} - \frac{h_1 W_{\vec{x}}}{\mathbb{1}+h_1 W_{\vec{x}}} + \mathbb{1} - \frac{h_1 W^\dagger_{\vec{x}}}{\mathbb{1}+h_1 W^\dagger_{\vec{x}}}\Big)\mathrm{Tr}\Big(\mathbb{1} - \frac{h_1 W_{\vec{x}+i}}{\mathbb{1}+h_1 W_{\vec{x}+i}} + \mathbb{1} - \frac{h_1 W^\dagger_{\vec{x}+i}}{\mathbb{1}+h_1 W^\dagger_{\vec{x}+i}}\Big)\\
\mathrm{Tr}\Big(\frac{h_1 W_{\vec{x}+i+j}}{\mathbb{1}+h_1 W_{\vec{x}+i+j}} + \frac{h_1 W^\dagger_{\vec{x}+i+j}}{\mathbb{1}+h_1 W^\dagger_{\vec{x}+i+j}}\Big)\mathrm{Tr}\Big(\frac{h_1 W_{\vec{x}+j}}{\mathbb{1}+h_1 W_{\vec{x}+j}} + \frac{h_1 W^\dagger_{\vec{x}+j}}{\mathbb{1}+h_1 W^\dagger_{\vec{x}+j}}\Big)\\
\mathrm{Tr}\Big(\frac{h_1 W_{\vec{x}}}{\mathbb{1}+h_1 W_{\vec{x}}} + \frac{h_1 W^\dagger_{\vec{x}}}{\mathbb{1}+h_1 W^\dagger_{\vec{x}}}\Big)\mathrm{Tr}\Big(\frac{h_1 W_{\vec{x}+i}}{\mathbb{1}+h_1 W_{\vec{x}+i}} + \frac{h_1 W^\dagger_{\vec{x}+i}}{\mathbb{1}+h_1 W^\dagger_{\vec{x}+i}}\Big)\\
\mathrm{Tr}\Big(\frac{h_1 W_{\vec{x}+i+j}}{\mathbb{1}+h_1 W_{\vec{x}+i+j}} + \frac{h_1 W^\dagger_{\vec{x}+i+j}}{\mathbb{1}+h_1 W^\dagger_{\vec{x}+i+j}}\Big)\mathrm{Tr}\Big(\frac{h_1 W_{\vec{x}+j}}{\mathbb{1}+h_1 W_{\vec{x}+j}} + \frac{h_1 W^\dagger_{\vec{x}+j}}{\mathbb{1}+h_1 W^\dagger_{\vec{x}+j}}\Big)
\end{aligned}
$$

Appendix B

SU(3) Integration

Treating the effective theory analytically requires knowledge of integrals of the type

$$\int dU L^m (L^*)^n, \tag{B.1}$$

with m, n being positive integers and L and L^* Polyakov loops. This can be done either numerically by parameterize the traces in terms of eq. 5.3 and introducing the Haar-Measure eq. 5.2 or by using the technique given in [99].

Using the second approach we start with the simplest non vanishing integral,

$$\int dU LL^* = \int dU \ \mathrm{Tr}U \ \mathrm{Tr}U^\dagger = \int dU U_{ii} U^\dagger_{jj} \tag{B.2}$$

Knowing from [99] that

$$\int dU U_{ij} U^\dagger_{kl} = \frac{1}{N_c} \delta_{il} \delta jk \tag{B.3}$$

we get

$$\int dU LL^* = \frac{1}{N_c} \delta_{ij} \delta_{ij} = 1. \tag{B.4}$$

In general integrals of this kind will only give a nonzero contribution if $(n-m)\%3 = 0$. For the analytic calculations in chapter 6 integrals up to order $m+n = 10$ where used,

the nonvanishing contributions are

$$\begin{aligned}
\int dUL^3 &= 1, \\
\int dUL^6 &= 5, \\
\int dUL^9 &= 42, \\
\int dU(L^*)^3 &= 1, \\
\int dU(L^*)^6 &= 5, \\
\int dU(L^*)^9 &= 42, \\
\int dUL^4(L^*) &= 3, \\
\int dUL^7(L^*) &= 21, \\
\int dUL^2(L^*)^2 &= 2, \\
\int dUL^5(L^*)^2 &= 11, \\
\int dUL^8(L^*)^2 &= 98, \\
\int dUL^3(L^*)^3 &= 6, \\
\int dUL^6(L^*)^3 &= 47, \\
\int dUL(L^*)^4 &= 3, \\
\int dUL^4(L^*)^4 &= 23, \\
\int dUL^2(L^*)^5 &= 11, \\
\int dUL^5(L^*)^5 &= 103, \\
\int dUL^3(L^*)^6 &= 47, \\
\int dUL(L^*)^7 &= 21, \\
\int dUL^2(L^*)^8 &= 98.
\end{aligned} \tag{B.5}$$

Appendix C

Transformation of the propagator traces into Polyakov Loops

The effective action derived in this thesis is formulated in traces over rational functions containing temporal Wilson lines, i.e.

$$\mathrm{Tr}\frac{h_1 W}{\mathbb{1}+h_1 W}. \tag{C.1}$$

When solving the theory analytically it is necessary to reformulate this in terms of Polyakov loops. This may also be convinient for numerical implementations. For this we use the generating function [1]

$$G[\alpha,\beta]=\ln\det[\alpha+\beta h_1 W]=\ln[\alpha^3+\alpha^2\beta h_1 L+\alpha\beta^2 h_1^2 L^\dagger+\beta^3 h_1^3]. \tag{C.2}$$

Expressions can then be derived by taking derivatives with respect to α and β at $\alpha=\beta=0$,

$$\mathrm{Tr}\frac{(h_1 W)^n}{(1+h_1 W)^{n+m}}=\frac{(-1)^{m+n-1}}{(m+n-1)!}\Big(\frac{\partial}{\partial\alpha}\Big)^m\Big(\frac{\partial}{\partial\beta}\Big)^n G[\alpha,\beta]\Big|_{\alpha=\beta=0}. \tag{C.3}$$

For example for $m=0,n=1$ we get

$$\mathrm{Tr}\frac{h_1 W}{\mathbb{1}+h_1 W}=\frac{h_1 L+2h_1^2 L^*+3h_1^3}{1+h_1 L+h_1^2 L^*+h_1^3}, \tag{C.4}$$

while $m=1,n=1$ gives

$$\mathrm{Tr}\frac{h_1 W}{(\mathbb{1}+h_1 W)^2}=\frac{h_1(L+4h_1^3 L+4h_1 L^*+h_1^4 L^*+h_1^2(9+LL^*))}{(1+h_1 L+h_1^2 L^*+h_1^3)^2}. \tag{C.5}$$

[1] Georg Bergner, private communication, 2014.

Bibliography

[1] ATLAS and CMS Collaborations. Experimental Tests of QCD. *CERN-CMS-CR-2013-435, arXiv:1312.5694 [hep-ex].*

[2] M. Gell-Mann. Symmetries of Baryons and Mesons. *Phys.Rev. 125 (1962) 1067-1084*, .

[3] Y. Ne'eman. Derivation of strong interactions from a gauge invariance. *Nucl.Phys. 26 (1961) 222-229.*

[4] M. Gell-Mann. A Schematic Model of Baryons and Mesons. *Phys.Lett. 8 (1964) 214-215*, .

[5] G. Zweig. An SU(3) model for strong interaction symmetry and its breaking. *CERN-TH-412, NP-14146, PRINT-64-170*, 1964.

[6] Particle Data Group Collaboration. Review of Particle Physics. *Chin.Phys. C38 (2014) 090001.*

[7] O.W. Greenberg. Spin and Unitary Spin Independence in a Paraquark Model of Baryons and Meson. *Phys.Rev.Lett. 13 (1964) 598-602.*

[8] LENA Collaboration. Measurement of R in e^+e^- annihilation for $\sqrt{s}$ between 7.4 and 9.4 GeV. *Z.Phys. C15 (1982) 299.*

[9] R. Faccini, L. Maiani, F. Piccinini, A. Pilloni, A.D. Polosa, and V. Riquer. A $J^{PG} = 1^{++}$ Charged Resonance in the Y(4260) to $\pi^+\pi^- J/\psi$ Decay? *Phys. Rev. D 87, 111102(R) (2013), arXiv:1303.6857 [hep-ph].*

[10] C. N. Yang and R. L. Mills. Conservation of Isotopic Spin and Isotopic Gauge Invariance. *Phys.Rev. 96 (1954) 191-195.*

[11] D. J. Gross and F. Wilczek. Ultraviolet Behavior of Non-Abelian Gauge Theories. *Phys. Rev. Lett. 30 (1973) 1343.*

[12] H. D. Politzer. Reliable Perturbative Results for Strong Interactions? *Phys.Rev.Lett. 30 (1973) 1346-1349.*

[13] G. t'Hooft. Renormalization of Massless Yang-Mills Fields. *Nucl.Phys. B33 (1971) 173-199.*

[14] S.Durr, Z. Fodor, J. Frison, C. Hoelbling, R. Hoffmann, S.D. Katz, S. Krieg, T. Kurth, L. Lellouch, T. Lippert, K.K. Szabo, and G. Vulvert. Ab-Initio Determination of Light Hadron Masses. *Science 322 (2008) 1224-1227, arXiv:0906.3599 [hep-lat].*

[15] S. Borsanyi, Z. Fodor, C. Hoelbling, S. D Katz, S. Krieg, C. Ratti, and K. K. Szabo. Is there still any T_c mystery in lattice QCD? Results with physical masses in the continuum limit III. *JHEP 1009:073,2010, arXiv:1005.3508.*

[16] J. I. Kapusta and C. Gale. *Finite-Temperature Field Theory Principles and Applications.* Cambridge Monographs on Mathematical Physics, 2006.

[17] M. E. Peskin and D. V. Schroeder. *An Introduction to Quantum Field Theory.* Westview Press, 1995.

[18] G. 't Hooft. Symmetry Breaking through Bell-Jackiw Anomalies. *Phys.Rev.Lett. 37 (1976) 8-11.*

[19] O. Philipsen and C. Pinke. The nature of the Roberge-Weiss transition in $N_f = 2$ QCD with Wilson fermions. *Phys. Rev. D 89, 094504 (2014), arXiv:1402.0838 [hep-lat].*

[20] A. Roberge and N. Weiss. Gauge theories with imaginary chemical potential and the phases of QCD. *Nucl.Phys. B275 (1986) 734.*

[21] T. Boeckel and J. Schaffner-Bielich. A little inflation at the cosmological QCD phase transition. *Phys.Rev. D85 (2012) 103506, arXiv:1105.0832 [astro-ph.CO].*

[22] O. Philipsen. The QCD phase diagram at zero and small baryon density. *PoS LAT2005 (2005) 016, arXiv:hep-lat/0510077.*

[23] N. Cabibbo and G. Parisi. Exponential hadronic spectrum and quark liberation. *Phys.Lett. B59 (1975) 67-69.*

[24] M. Gyulassy. The QGP discovered at RHIC. *arXiv:nucl-th/0403032*, 2004.

[25] U. W. Heinz and M. Jacob. Evidence for a New State of Matter: An Assessment of the Results from the CERN Lead Beam Programme. *arXiv:nucl-th/0002042*, 2000.

[26] Y. Aoki, Z. Fodor, S.D. Katz, and K.K. Szabo. The QCD transition temperature: results with physical masses in the continuum limit. *Phys.Lett. B643 (2006) 46-54, arXiv:hep-lat/0609068.*

[27] R. V. Gavai and S. Gupta. On the critical end point of QCD. *Phys. Rev. D 71 (2005) 114014.*

[28] Z. Fodor and S.D. Katz. Lattice determination of the critical point of QCD at finite T and mu. *JHEP 0203 (2002) 014, arXiv:hep-lat/0106002.*

[29] P. de Forcrand and O. Philipsen. The QCD phase diagram for small densities from imaginary chemical potential. *Nucl.Phys. B642 (2002) 290-306, arXiv:hep-lat/0205016*, .

[30] R. A. Lacey, N.N. Ajitanand, J.M. Alexander, P. Chung, J. Jia, A. Taranenko, and P. Danielewicz. An Estimate for the location of QCD critical end point . *arXiv:0708.3512 [nucl-ex]*, 2007.

[31] STAR Collaboration. An Experimental Exploration of the QCD Phase Diagram: The Search for the Critical Point and the Onset of De-confinement. *arXiv:1007.2613 [nucl-ex]*, 2010.

[32] A. Delfino and J.B. Silva. Approximate analytical solution for nuclear matter in a mean-field Walecka model and Coester line behavior. *Phys.Rev. C73 (2006) 037311.*

[33] K. Fukushima and C. Sasaki. The phase diagram of nuclear and quark matter at high baryon density. *Prog.Part.Nucl.Phys. 72 (2013) 99-154, arXiv:1301.6377 [hep-ph].*

[34] V.A. Karnaukhov, H. Oeschler, S.P. Avdeyev, E.V. Duginova, V.K. Rodionov, A. Budzanowski, W. Karcz, O.V. Bochkarev, E.A. Kuzmin, L.V. Chulkov, E. Norbeck, and A.S. Botvina. Critical Temperature for the Nuclear Liquid-Gas Phase Transition. *Phys.Rev. C67 (2003) 011601, arXiv:nucl-ex/0302006.*

[35] T Tatsumi, N Yasutake, and T Maruyama. Mixed phases during the phase transitions. *arXiv:1107.0804 [nucl-th]*, 2011.

[36] K. Fukushima. Generic features of the phase transition in cold and dense quark matter. *Phys.Rev. D86 (2012) 054002, arXiv:1204.0594 [hep-ph].*

[37] M. G. Alford, K. Rajagopal, T. Schaefer, and A. Schmitt. Color superconductivity in dense quark matter. *Rev.Mod.Phys. 80 (2008) 1455-1515, arXiv:0709.4635 [hep-ph].*

[38] K. G. Wilson. Confinement of quarks. *Phys. Rev. D 10 (1974) 2445*, .

[39] M. Creutz. Lattice gauge theory: A retrospective. *Nucl.Phys.Proc.Suppl. 94 (2001) 219-226, arXiv:hep-lat/0010047*, .

[40] K. G. Wilson. The Origins of Lattice Gauge Theory. *Nucl.Phys.Proc.Suppl.140:3-19,2005, arXiv:hep-lat/0412043*, .

[41] C. Gattringer and C. B. Lang. *Quantum Chromodynamics on the Lattice*. Springer, 2010.

[42] I. Montvay and G. Münster. *Quantum Fields on a Lattice*. Cambridge University Press, 1994.

[43] T. DeGrand and C. DeTar. *Lattice Methods for Quantum Chromodynamics*. World Scientific Publishing, 2006.

[44] M. Lüscher and P. Weisz. On-shell improved lattice gauge theories. *Commun.Math.Phys. 97 (1985) 59*.

[45] H.B. Nielsen and M. Ninomiya. A no-go theorem for regularizing chiral fermions. *Phys.Lett. B105 (1981) 219*.

[46] K. G. Wilson. Quarks and string on a lattice. *The Subnuclear Series Volume 13, 1977, pp 69-142*, .

[47] P.T. Matthews and A. Salam. The Green's functions of quantized fields. *Nuovo Cim. 12 (1954) 563-565*, .

[48] P.T. Matthews and A. Salam. Propagators of quantized field. *Nuovo Cim. 2 (1955) 120-134*, .

[49] CP-PACS and JLQCD Collaborations. Computational cost of full QCD simulations experienced by CP-PACS and JLQCD Collaborations. *Nucl.Phys.Proc.Suppl. 106 (2002) 195-196*.

[50] N. Metropolis. The Beginning of the Monte Carlo Method. *Los Alamos Science Special Issue (1987)*.

[51] N. Metropolis, A.W. Rosenbluth, M.N. Rosenbluth, A.H. Teller, and E. Teller. Equation of State Calculations by Fast Computing Machines. *J.Chem.Phys. 21 (1953) 1087-1092*.

[52] A. Gelman, W. R. Gilks, and G. O. Roberts. Weak convergence and optimal scaling of random walk Metropolis algorithms. *Ann. Appl. Probab. Volume 7, Number 1 (1997), 110-120*.

[53] Y. S. Wu G. Parisi. Perturbation theory without gauge fixing. *Sci.Sin. 24 (1981) 483*.

[54] P. Damgaard and H. Hüffel. Stochastic Quantization. *PHYSICS REPORTS 152, Nos. 5 & 6 (1987) 227-398.*

[55] P. Langevin. On the Theory of Brownian Motion. *C. R. Acad. Sci. (Paris) 146,. 530–533 (1908).*

[56] F. Karsch and H.W.Wyld. Complex Langevin Simulation of the SU(3) Spin Model With Nonzero Chemical Potential. *Phys.Rev.Lett. 55 (1985) 2242,*, 1985.

[57] N. Bilic, H. Gausterer, and S. Sanielevici. Complex Langevin Solution to an Effective Theory of Lattice QCD. *Phys.Rev. D37 (1988) 3684*, 1987.

[58] G. Aarts. Can stochastic quantization evade the sign problem? – the relativistic Bose gas at finite chemical potential. *Phys.Rev.Lett. 102 (2009) 131601, arXiv:0810.2089 [hep-lat].*

[59] I. O. Stamatescu G. Aarts. Stochastic quantization at finite chemical potential. *JHEP 0809 (2008) 018, arXiv:0807.1597 [hep-lat]*, .

[60] F. A. James G. Aarts. Complex Langevin dynamics in the SU(3) spin model at nonzero chemical potential revisited. *JHEP 1201 (2012) 118, arXiv:1112.4655 [hep-lat]*, .

[61] D. Sexty. Simulating full QCD at nonzero density using the complex Langevin equation. *Phys.Lett. B729 (2014) 108-111, arXiv:1307.7748 [hep-lat].*

[62] H. Hueffel and G. Kelnhofer. QED Revisited: Proving Equivalence Between Path Integral and Stochastic Quantization. *Phys.Lett. B588 (2004) 145-150.*

[63] W. Grimus and H. Hueffel. Pertubation Theory from Stochastic Quantization of Scalar Fields. *Z.Phys. C18 (1983) 129.*

[64] H. Huffel and H. Rumpf. Stochastic Quantization in Minkowski Space. *Phys.Lett. B148 (1984) 104-110.*

[65] G. Aarts, F.A. James, E. Seiler, and I.O. Stamatescu. Adaptive stepsize and instabilities in complex Langevin dynamics. *Phys.Lett. B687 (2010) 154-159, arXiv:0912.0617 [hep-lat]*, .

[66] P. de Forcrand. Simulating QCD at finite density. *PoS LAT2009 (2009) 010, arXiv:1005.0539 [hep-lat].*

[67] T. Cohen. Functional integrals for QCD at nonzero chemical potential and zero density. *Phys.Rev.Lett. 91 (2003) 222001, arXiv:hep-ph/0307089.*

[68] J. R. Ipsen and K. Splittorff. Baryon Number Dirac Spectrum in QCD. *Phys.Rev. D86 (2012) 014508, arXiv:1205.3093 [hep-lat].*

[69] I. M. Barbour, S. E. Morrison, E. G. Klepfish, J. B. Kogut, and M. P. Lombardo. Results on Finite Density QCD. *Nucl.Phys.Proc.Suppl. 60A (1998) 220-234, arXiv:hep-lat/9705042.*

[70] S. Gottlieb, D. Toussaint W. Liu, R. L. Renken, and R. L. Sugar. Quark-number susceptibility of high-temperature QCD. *Phys. Rev. Lett. 59 (1987) 2247.*

[71] J. B. Kogut and D. K. Sinclair. The finite temperature transition for 2-flavour lattice QCD at finite isospin density. *Phys.Rev. D70 (2004) 094501, arXiv:hep-lat/0407027.*

[72] S.K. Yang J. Ambjorn. Numerical Problems in applying the Langevin Equation to complex effective actions. *Phys.Lett. B165 (1985) 140.*

[73] H.Q. Lin and J.E. Hirsch. Monte Carlo versus Langevin methods for nonpositive definite weights. *Phys. Rev. B 34, 1964.*

[74] J. Berges, Sz. Borsanyi, D. Sexty, and I. O. Stamatescu. Lattice simulations of real-time quantum fields. *Phys.Rev. D75 (2007) 045007, arXiv:hep-lat/0609058.*

[75] G. Aarts and F. A. James. On the convergence of complex Langevin dynamics: the three-dimensional XY model at finite chemical potential. *JHEP 1008 (2010) 020, arXiv:1005.3468 [hep-lat].*

[76] H. Hamber and G. Parisi. Numerical Estimates of Hadronic Masses in a Pure SU(3) Gauge Theory. *Phys.Rev.Lett. 47 (1981) 1792.*

[77] D.T. Son and M.A. Stephanov. QCD at finite isospin density. *Phys.Rev.Lett. 86 (2001) 592-595, arXiv:hep-ph/0005225.*

[78] I. M. Barbour and Susan E. Morrison. The Critical Points of Strongly Coupled Lattice QCD at Nonzero Chemical Potential. *Phys.Rev. D56 (1997) 7063-7072, hep-lat/9705038.*

[79] A. Ferrenberg and R. Swendsen. New Monte Carlo technique for studying phase transitions. *Phys.Rev.Lett. 61 (1988) 2635-2638.*

[80] P. de Forcrand, S. Kim, and T. Takaishi. QCD simulations at small chemical potential. *Nucl.Phys.Proc.Suppl. 119 (2003) 541-543, arXiv:hep-lat/0209126.*

[81] C. Bonati, P. de Forcrand, M. D'Elia, O.Philipsen, and F. Sanfilippo. Constraints on the two-flavor QCD phase diagram from imaginary chemical potential. *PoS LATTICE2011 (2011) 189, arXiv:1201.2769 [hep-lat],* .

[82] P. de Forcrand and O. Philipsen. Constraining the QCD phase diagram by tricritical lines at imaginary chemical potential. *Phys.Rev.Lett. 105 (2010) 152001, arXiv:1004.3144 [hep-lat]*, .

[83] C. Bonati, P. de Forcrand, M. D'Elia, O. Philipsen, and F. Sanfilippo. The chiral phase transition in two-flavor QCD from imaginary chemical potential. *Phys.Rev. D90 (2014) 074030, arXiv:1408.5086 [hep-lat]*, .

[84] P. de Forcrand and O. Philipsen. The chiral critical point of Nf=3 QCD at finite density to the order $(\mu/T)^4$. *JHEP0811:012 (2008), arXiv:0808.1096*, .

[85] G. Aarts, F. A. James, E. Seiler, and I. O. Stamatescu. Complex Langevin: Etiology and Diagnostics of its Main Problem. *Eur.Phys.J. C71 (2011) 1756, arXiv:1101.3270 [hep-lat]*, .

[86] G. Aarts, P. Giudice, and E. Seiler. Localised distributions and criteria for correctness in complex Langevin dynamics. *Annals Phys. 337 (2013) 238-260, arXiv:1306.3075*, .

[87] Erhard Seiler, Dénes Sexty, and Ion-Olimpiu Stamatescu. Gauge cooling in complex Langevin for QCD with heavy quarks. *Phys.Lett. B723 (2013) 213-216, arXiv:1211.3709 [hep-lat].*

[88] J. Langelage and O. Philipsen. The pressure of strong coupling lattice QCD with heavy quarks, the hadron resonance gas model and the large N limit. *JHEP 1004 (2010) 055 arXiv:1002.1507 [hep-lat].*

[89] J. Langelage, S. Lottini, and O. Philipsen. Centre symmetric 3d effective actions for thermal SU(N) Yang-Mills from strong coupling series. *JHEP 1102 (2011) 057 Erratum-ibid. 1107 (2011) 014, arXiv:1010.0951 [hep-lat].*

[90] S. Lottini M. Fromm, J. Langelage. The QCD deconfinement transition for heavy quarks and all baryon chemical potentials. *JHEP 1201 (2012) 042 arXiv:1111.4953 [hep-lat].*

[91] M. Fromm, J. Langelage, S. Lottini, M. Neuman, and O. Philipsen. Phase transitions in heavy-quark QCD from an effective theory. *J.Phys.Conf.Ser. 432 (2013) 012033 arXiv:1210.7994 [hep-lat]*, .

[92] M. Fromm, J. Langelage, M. Neuman, and O. Philipsen. The onset transition to cold nuclear matter from lattice QCD with heavy quarks. *Phys.Rev.Lett. 110 (2013) 122001, arXiv:1207.3005 [hep-lat]*, .

[93] G. Münster. High Temperature Expansions for the Free Energy of Vortices, Respectively the String Tension in Lattice Gauge Theories. *Nucl.Phys. B180 (1981) 23.*

[94] G. S. Bali. Casimir scaling of SU(3) static potentials. *Phys.Rev. D62 (2000) 114503, arXiv:hep-lat/0006022.*

[95] C. Wozar, T. Kaestner, A. Wipf, and T. Heinzl. Inverse Monte-Carlo determination of effective lattice models for SU(3) Yang-Mills theory at finite temperature. *Phys.Rev. D76 (2007) 085004, arXiv:0704.2570.*

[96] O. Philipsen G.Bergner, J. Langelage. Effective lattice Polyakov loop theory vs. full SU(3) Yang-Mills at finite temperature. *JHEP 1403 (2014) 039, arXiv:1312.7823 [hep-lat].*

[97] J. Kogut and M. Stephanov. *The Phases of Quantum Chromodynamics.* Cambridge Monographs on Particle Physics, Nuclear Physics and Cosmology, 2004.

[98] C. Gattringer. Flux representation of an effective Polyakov loop model for QCD thermodynamics. *Nucl.Phys. B850 (2011) 242-252, arXiv:1104.2503 [hep-lat].*

[99] M. Creutz. On invariant integration over SU(N). *J.Math.Phys. 19 (1978) 2043*, .

[100] P. D. Pedersen A. S. Christensen, J. C. Myers. Large N lattice QCD and its extended strong-weak connection to the hypersphere. *JHEP 1402 (2014) 028, arXiv:1312.3519 [hep-lat].*

[101] M. Gross, J. Bartholomew, and D. Hochberg. Su(n) Deconfinement Transition And The N State Clock Model. *EFI-83-35-CHICAGO (1983).*

[102] A. Mollgaard and K. Splittdorff. Complex Langevin Dynamics for chiral Random Matrix Theory. *Phys.Rev. D88 (2013) 116007, arXiv:1309.4335 [hep-lat].*

[103] S. Necco and R. Sommer. The $N_f = 0$ heavy quark potential from short to intermediate distances. *Nucl.Phys.B622:328-346 (2002), [arXiv:hep-lat/0108008].*

[104] Jan Smit. *Introduction to Quantum Fields on a Lattice.* Cambridge University Press, 2002.

[105] J. Hoek and J. Smit. On the $1/g^2$ Corrections to Hadron Masses. *Nucl.Phys. B263 (1986) 129.*

[106] C. Pinke. *Lattice QCD at Finite Temperature with Wilson Fermions.* PhD thesis, Goethe Universität Frankfurt, 2014.

[107] K. Binder. Finite size scaling analysis of Ising model block distribution functions. *Z.Phys. B43 (1981) 119-140.*